

Gold Distribution and the Relationship to
Pyrite Trace Element Geochemistry at the
Ernest Henry Deposit, Queensland

Thesis submitted in accordance with the requirements of the University of Adelaide for
an Honours Degree in Geology

James Bentley Hewett
October 2017



GOLD DISTRIBUTION AND THE RELATIONSHIP TO PYRITE TRACE ELEMENT GEOCHEMISTRY AT
THE ERNEST HENRY DEPOSIT, QUEENSLAND

RUNNING TITLE: ERNEST HENRY GOLD AND PYRITE

ABSTRACT

The Ernest Henry deposit is situated within the Eastern Fold Belt of the Mount Isa Inlier, NW Queensland, and is the largest iron oxide copper-gold (IOCG) deposit in the Proterozoic Cloncurry district. The hydrothermal deposit is hosted in brecciated intermediate meta-volcanic and metasedimentary rocks with a biotite-calcite-chalcopyrite-gold-magnetite-pyrite-quartz mineral assemblage.

This study investigates the mineralogical, textural and geochemical association between gold and pyrite with samples collected from three drill holes (EH768, EH859 and EH864) at ~700 m vertical depth within the ore body.

Majority of the gold (~98%) at Ernest Henry is in the form of free gold, which is commonly observed in pyrite microfractures, associated with chalcopyrite infill. Free gold has been interpreted to have entered the system with the main economic Cu-Au mineralisation stage. We propose that the semi-conducting potential of pre-existing pyrite surfaces have acted as a catalyst for the precipitation of free gold.

Implications from this study may assist in the improvement of gold recovery at Ernest Henry, and provide a better understanding of the timing of the 'C' and 'G' in 'IOCG' deposits in the local Cloncurry District.

KEYWORDS

Arsenian pyrite, chalcopyrite, electrochemical reduction, gold distribution, free gold, geochemistry, iron oxide copper-gold, pyrite, trace elements

TABLE OF CONTENTS

Abstract.....	i
Keywords.....	i
Table of Contents.....	ii
Table of Figures.....	iv
Table of Tables.....	iv
Introduction.....	1
Geological Setting.....	5
Methods.....	11
Sample Collection & Preparation.....	11
SEM – Mineral Liberation Analysis.....	12
LA-ICP-MS.....	14
Observations & Results.....	18
Petrology.....	18
SEM Observations of Free Gold.....	21
LA-ICP-MS.....	28
Pyrite Trace Elements.....	28
Pyrite Zonation.....	31
Arsenian Pyrite and Free Gold.....	34
Other Forms of Gold.....	36
Summary of Results.....	38
Discussion.....	39
Pyrite Textures.....	39
Gold Chemistry.....	40
As-Co-Ni Pyrite Chemistry.....	42
Electrochemical Reduction of Gold.....	43
Fluid Chemistry.....	46
Regional Deposits: A Result of Fluid Mixing.....	47
Mining Challenges.....	49
Conclusions.....	51
Further Research.....	51
Acknowledgements.....	52
References.....	53
Appendix 1.a: Lithology Descriptions.....	56

Appendix 1.b: Sample Summary	57
Appendix 2.a: Extended Mineralogical and Textural Setting of Free Gold	60
Appendix 2.b: Extended Images of Free Gold.....	64
Appendix 3.a: Extended Geochemical Pyrite Maps	92
Appendix 3.b: Pyrite Geochemical Spot Locations.....	98
Appendix 4: Gold Mass Balance	99

TABLE OF FIGURES

Figure 1: Regional geology and study location.	2
Figure 2: The different elements that correlate with Au at the assay scale.	4
Figure 3: Geological cross-section of the Ernest Henry ore body.	7
Figure 4: The succession of the three major mineralisation and alteration stages of the Ernest Henry.	10
Figure 5: Half-core images of the targeted pyrite textures.	12
Figure 6: Example of a high quality BSE map, EDS spectrum, and MLA map.	13
Figure 7: Distribution of spot locations for a) pyrite, b) chalcopyrite, and c) magnetite.	17
Figure 8: Three rock types sampled from the 1475 Level of the ore body.	18
Figure 9: Pyrite textures of the half-core samples.	19
Figure 10: Reflected light optical images representing the three identified pyrite textures at the micro-scale. ...	21
Figure 11: Average gold grain size.	22
Figure 12: SEM images of free gold textures.	23
Figure 13: SEM images of the common locations of free gold associated to pyrite.	26
Figure 14: SEM images representing the unique mineralogical settings of free gold.	27
Figure 15: Example of all the elements mapped with ICP-MS.	29
Figure 16: As-Co-Ni laser maps of the three pyrite textures.	32
Figure 17: As-Co-Ni zonation of Vein-infill Pyrite.	33
Figure 18: Pyrite ICP-MS spot data displaying no correlation between As and Au.	34
Figure 19: Spatial association of free gold and As concentration gradient.	35
Figure 20: ICP-MS spot data representing invisible gold in pyrite as solid solution and nano-inclusions.	36
Figure 21: Ternary diagram of the Au-Ag-Cu system.	40
Figure 22: Electrochemical precipitation of free gold onto pre-existing pyrite surfaces.	45
Figure 23: 3D illustration of how the crystal defects that free S ⁻ attract Au ⁺ or Au ³⁺	45
Figure 24: Scatter plot representing the Co to Ni ratios for pyrite of different origins.	49

TABLE OF TABLES

Table 1: Overview of the parameters applied to the NewWave LA-ICP-MS.	16
Table 2: The dominant pyrite texture and lithology recorded for each sample.	19
Table 3: Mineralogical, textural, and lithological associations of free gold grains.	24
Table 4: Pyrite chemistry classified into the different pyrite textures.	30
Table 5: Pyrite chemistry classified into the different lithology.	30
Table 6: The mean and standard deviations of As-Co-Ni for the different pyrite textures.	31
Table 7: The economic resource at Ernest Henry, including the gold compositions of chalcopyrite and pyrite. .	37

INTRODUCTION

Gold is a significant by-product of many base metal mines. The textural and mineralogical setting, and mechanisms of free gold precipitation are important considerations for metallogenesis and ore processing, and even small percentage improvements in gold recovery can affect mine economics. In hydrothermal deposits, including iron oxide copper-gold (IOCG), gold commonly occurs as free gold grains (95 to 65 wt.% Au), or as invisible gold in the form of nano-inclusions or solid solution hosted in minerals such as chalcopyrite, pyrite, and magnetite (Ciobanu et al., 2012; Cook & Chryssoulis, 1990; A. Foster, Williams, & Ryan, 2007; Rusk et al., 2010; Schwartz, 1944).

The Ernest Henry (EH) IOCG deposit is located within the Eastern Succession of the Proterozoic Mount Isa Inlier, ~35 km northeast of the Cloncurry Township in northern Australia (Figure 1). Discovered in 1991, EH was evaluated with a pre-mining resource of 166 million tonnes (Mt) at 1.1% Cu and 0.54 g/t Au (Ryan, 1998). EH Mining operated as an open pit from 1996 to 2013, and has subsequently transitioned into an underground sub-level cave operation with a December 2015 underground resource estimate of 87.1 Mt at 1.18% Cu and 0.60 g/t Au. Ore is processed through a mill with a capacity of ~10 Mt/year with the recovery from primary ore averaging ~65% gold and 90% for copper (EH Mining 2000).

Elemental associations between Au and other elements (As, Co, Cu, Fe, Ni, and S) were established early in the mine life (Figure 2), with the copper to gold ratio and high arsenic content being two of the key discriminants between EH and different IOCG deposits in the Eastern Succession. Previous research of gold distribution at EH by A. Foster et al. (2007) investigated the uppermost levels (~300 m vertical depth) of the ore system (Figure 3) and concluded that majority of the gold exists as free gold associated with chalcopyrite and pyrite.

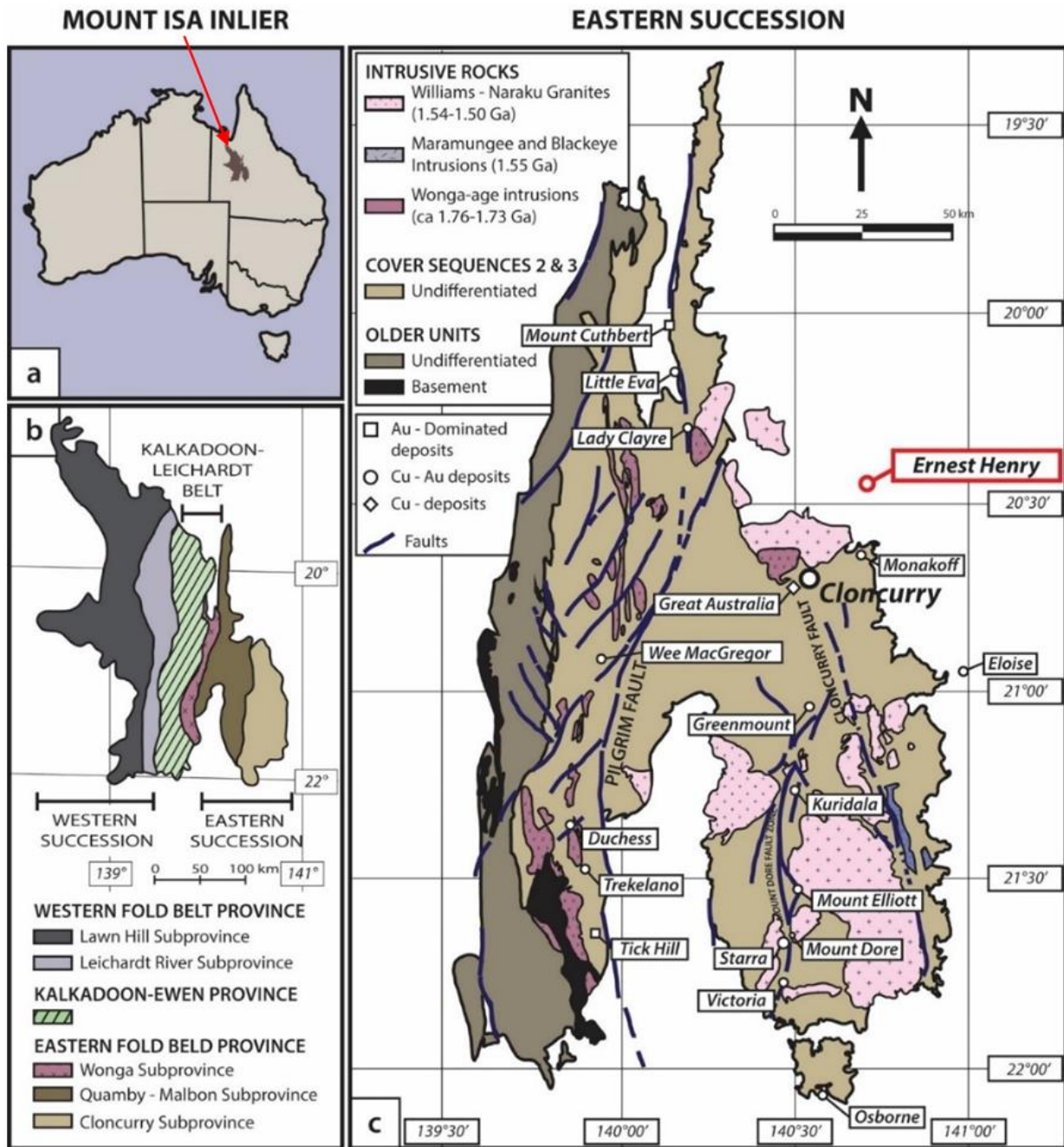


Figure 1: Regional geology and study location: a) location of Mount Isa Inlier, b) sub provinces of the Mount Isa Inlier adapted from Denaro, Ramsden, and Brown (2007), c) simplified geology and mineral deposits of the Eastern Succession including EH (circled), various deposits, and major faults adapted from Mark, Oliver, and Williams (2006). Note the white background where EH is located represents sedimentary cover.

The ore body encompasses three main lithologies (Figure 3a, f, g); intermediate volcanics (*iv*); clast-supported felsic volcanics (*fv1*); and the sulphide-rich matrix-supported felsic volcanics (*fv2*). Splitting the ore body at depth is an uneconomic zone hosted by *iv* lithology termed the ‘Interlens’ (Figure 3h). Pyrite textures originally defined by A. Foster et al. (2007) are consistent with the paragenesis of Mark et al. (2006). *Disseminated*, *Porphyroblastic*, and *Vein-infill Pyrite* have been defined to differentiate pyrite generations and the associated free gold.

This study utilises petrographic observations, Scanning Electron Microscopy Energy-Dispersive X-Ray Spectrometry (SEM-EDS), and Mineral Liberation Analysis (MLA) to document the mineralogical and textural variations of gold in the current production levels (Figure 3). Furthermore, Laser Ablation Inductively Coupled Plasma Mass Spectrometer (LA-ICP-MS) has been used to explore the variations of trace elements in gold-bearing minerals such as pyrite.

Five key questions have been addressed to better understand the related free gold associated to pyrite:

- What is the mineralogical and textural association of free gold and pyrite?
- Is there an association between pyrite chemistry, pyrite texture, and lithology?
- Is As-Co-Ni zonation present in pyrite, and is it consistent between the different pyrite textures?
- Is there an association between As concentration in pyrite and free gold?
- Are there other forms of gold that should be further investigated?

This study assists recent trends which have investigated mineral trace element compositions to better constrain the origin and variation of hydrothermal fluids. However, the primary purpose of this study is to better understand the distribution of gold, and to determine possible methods of improving gold recovery.

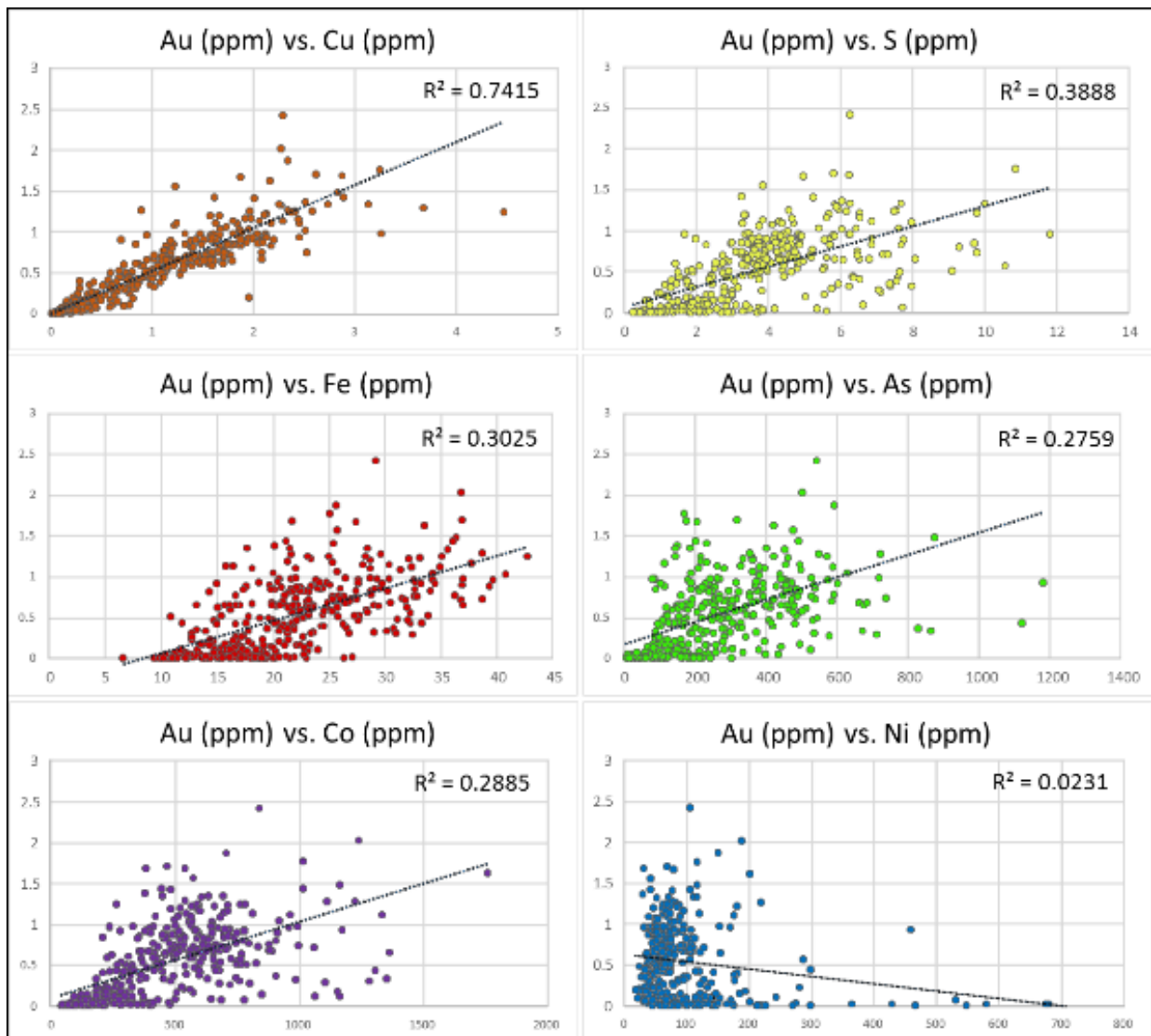


Figure 2: Bivariate scatter plots representing different elemental relationships with Au. The elements of chalcopyrite (CuFeS) and pyrite (FeS) are closely related to Au. Pyrite is commonly associated with As, Co, and Ni. Drill assay data from EH Mining (2000) and A. Foster et al. (2007).

GEOLOGICAL SETTING

The Proterozoic Mount Isa Inlier is composed of three provinces; the Western Fold Belt, (central) Kalkadoon-Leichhardt Belt, and the Eastern Fold Belt (Figure 1). Each province formed by tectonic extension during three periods of protracted intracontinental rifting and are defined by N-S trending major faults or fault zones (Blake, 1987; Blake & Stewart, 1992). The Eastern Succession rifting events have resulted in three distinct cover sequences deposited between 1890 and 1610 Ma (Etheridge, Rutland, & Wyborn, 1987). Remnants of the first cycle formed the basement (Cover Sequence 1), which was overprinted during metamorphism (amphibolite facie) of the Barramundi Orogeny from 1890 to 1850 Ma (Blake, 1987). This basement package was overlain by a sequence of sediments and bimodal volcanics from the second cycle; Cover Sequence 2 (1800 to 1750 Ma), which was unconformably overlain by Cover Sequence 3 from 1710 to 1610 Ma (Blake, 1987) and it is during this period that the majority of IOCG deposits are believed to have formed (D. Foster & Austin, 2008). Both sequences were later deformed and metamorphosed during the 1600 to 1500 Ma Isan Orogeny (Blake & Stewart, 1992; D. Foster, 2003; D. Foster & Rubenach, 2006; Page & Sun, 1998), and it is during this time that EH formed (Mark et al., 2006).

The largest of these deposits is the polymetallic (Cu, Au, Ag, Fe, Ba, Bi, Co, Mo, W, As, U, Ni and REE) EH deposit. The orebody is hosted by strongly metasomatised intermediate metavolcanic rocks that are geochemically, geochronologically, and stratigraphically comparable to the neighbouring 1740 Ma Mount Fort Constantine volcanics (P. Williams et al., 2005). Chalcopyrite is the main economic sulphide mineral and is hosted in a magnetite and K-feldspar bearing, pipe-like breccia that is structurally constrained by two magnetite-biotite altered sub-parallel shear zones (Figure 3b, c). The ore body dips $\sim 45^\circ$ to the SSE and is split by the Interlens; a sulphide-poor pre-mineralisation shear zone (Figure 3h). The weakly brecciated and mineralised Interlens is likely to represent intercalated metasedimentary and metamafic volcanic rocks within the main intermediate volcanic package (Cave, 2017; Lilly, Case, & Miller, 2017; O'Brien, 2016).

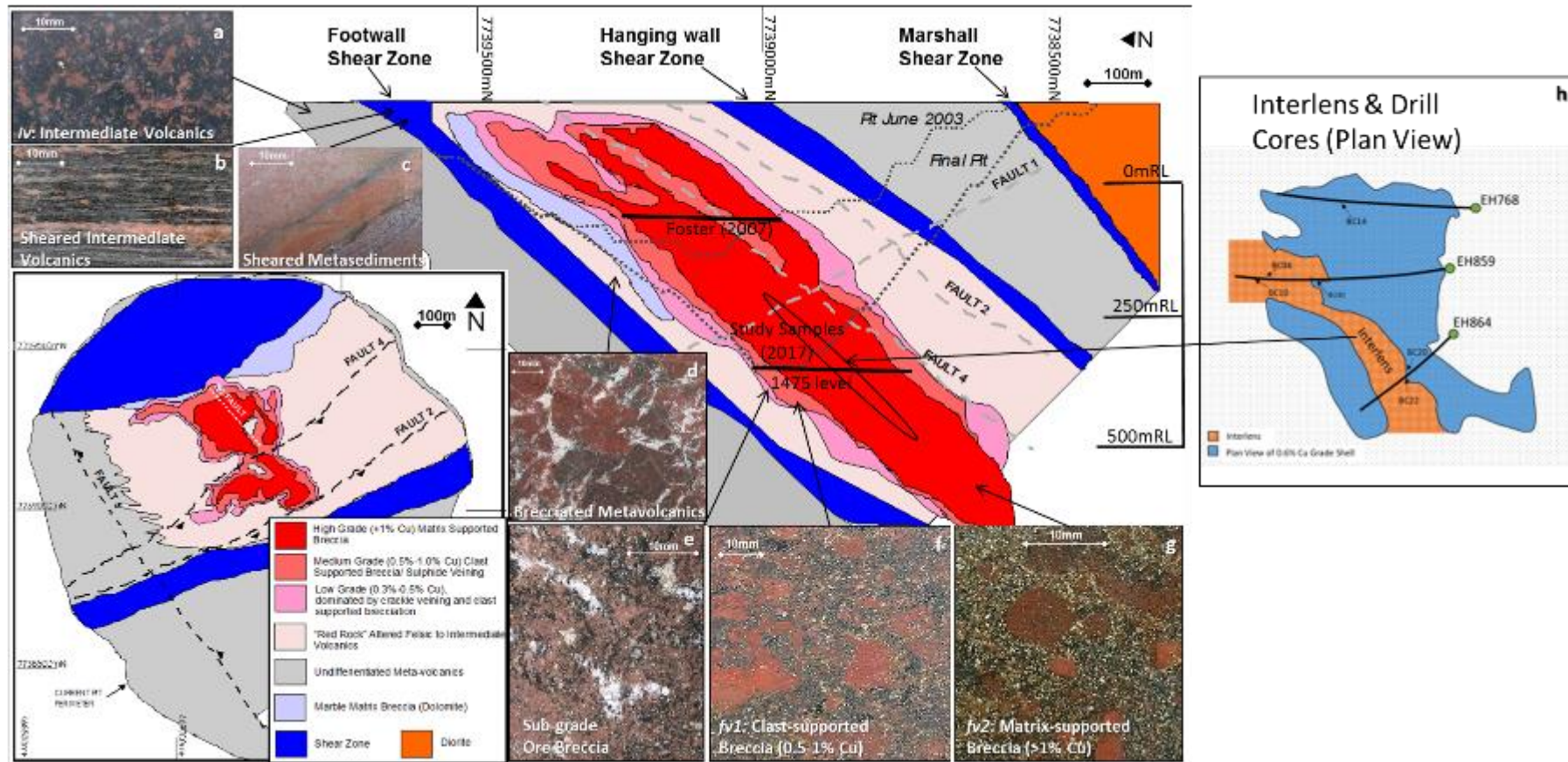


Figure 3: Geological cross-section (looking east) of the host, altered, and mineralised rock distributed through the ore body. The structurally constrained pipe-like orebody is bounded by zones of extensive shearing (blue). The orebody is hosted in strongly altered and variable; a) brecciated; sheared b) metovolcanics and c) metasedimentary rocks, d) metovolcanic rocks closer to the orebody display strong K-feldspar alteration (red) and crackle veining with carbonate and quartz infill (white). Alteration and infill increase towards the orebody as the host metovolcanics diminish, resulting in rounded clasts (black magnetite, and speckle-gold chalcopryrite and pyrite); e, f, g) represents a progressive increase in copper-gold grade. h) Plan view of the 1475 level sample locations and the Interlens. Note location of samples from A. Foster et al. (2007) and this study (black lines on cross section). Adapted from Cave (2017) and Lilly et al. (2017).

The metasomatic evolution of the EH mineral system has been well established (Mark et al., 2006). Fluid inclusion and isotope studies indicate that at least two fluids have been involved in the ore generation process: a high-temperature (>450°C) granite-derived oxidised fluid and a lower-temperature reduced fluid, possibly sourced from basinal brines (Fuss, 2014; Kendrick, Mark, & Phillips, 2007; Oliver et al., 2008; M. Williams, Holwell, Lilly, Case, & McDonald, 2015). The currently accepted model is a hypothesis that supports repeated brecciation that facilitates chemical milling by interaction between hydrothermal fluids, and assimilation of wall-rock and clast boundaries along structurally controlled pathways (Austin & Blenkinsop, 2009; Baker et al., 2008; Kendrick et al., 2007; Pollard, 2006). Contending this model is the hypothesis that ore formation involves the release of CO₂ from fluids sourced directly from enriched mantle or indirectly through mafic magmas (Oliver et al., 2006). The CO₂ release facilitates brecciation and mineralisation, sharing similar characteristics to that of kimberlite dykes (Oliver et al., 2006).

Four main stages of hydrothermal alteration and mineralisation are recognised (Mark et al., 2006) (Figure 4):

- 1) Regional sodic-calcic alteration displays a metasomatic event characterized by fine grained albite and scapolite-altered rocks found throughout the Eastern Fold Belt (Mark et al., 2006). This alteration formed as the result of 350 to 450°C fluids that migrated along fractures, faults, and lithological boundaries (Mark et al., 2006).
- 2) Pre-mineralisation and alteration displays similar chemical and mineralogical characteristics of the ore assemblage (Mark et al., 2001). This alteration is divided into two groups; the first group is a dark rock alteration and consists of fine grained biotite and magnetite rich alteration which overprints regionally altered rocks (Mark et al., 2006). The second group is commonly termed 'red rock' alteration, and consists

of K-feldspar-biotite-garnet-pyrite bearing veins and alteration (Mark, Oliver, Williams, Valenta, & Crookes, 1999).

- 3) Mineralisation of the ore assemblage took place because of magmatic and basinal fluid mixing (Kendrick et al., 2007). Additionally, wall rock assimilation and changing pressure and temperature conditions may have influenced precipitation (Baker et al., 2008). The ore grade assemblage consists of magnetite-calcite-pyrite-chalcopyrite-quartz with minor barite-biotite-hematite-K-feldspar. Copper mineralisation occurs as chalcopyrite infilling between breccia clasts, and gold as native gold or electrum grains associated with chalcopyrite (A. Foster et al., 2007; Mark et al., 2006). Titanite (Mark et al., 2006) and apatite (Cave, 2017) have been dated with the conventional U-Pb method, dating the EH mineral assemblage to 1529 ± 24 Ma and 1529 ± 39 Ma.
- 4) Post-mineralisation events are represented by carbonate-rich veins and minor breccia hosting calcite-dolomite-quartz overprinting all previous stages (Mark et al., 2001; Rusk et al., 2010).

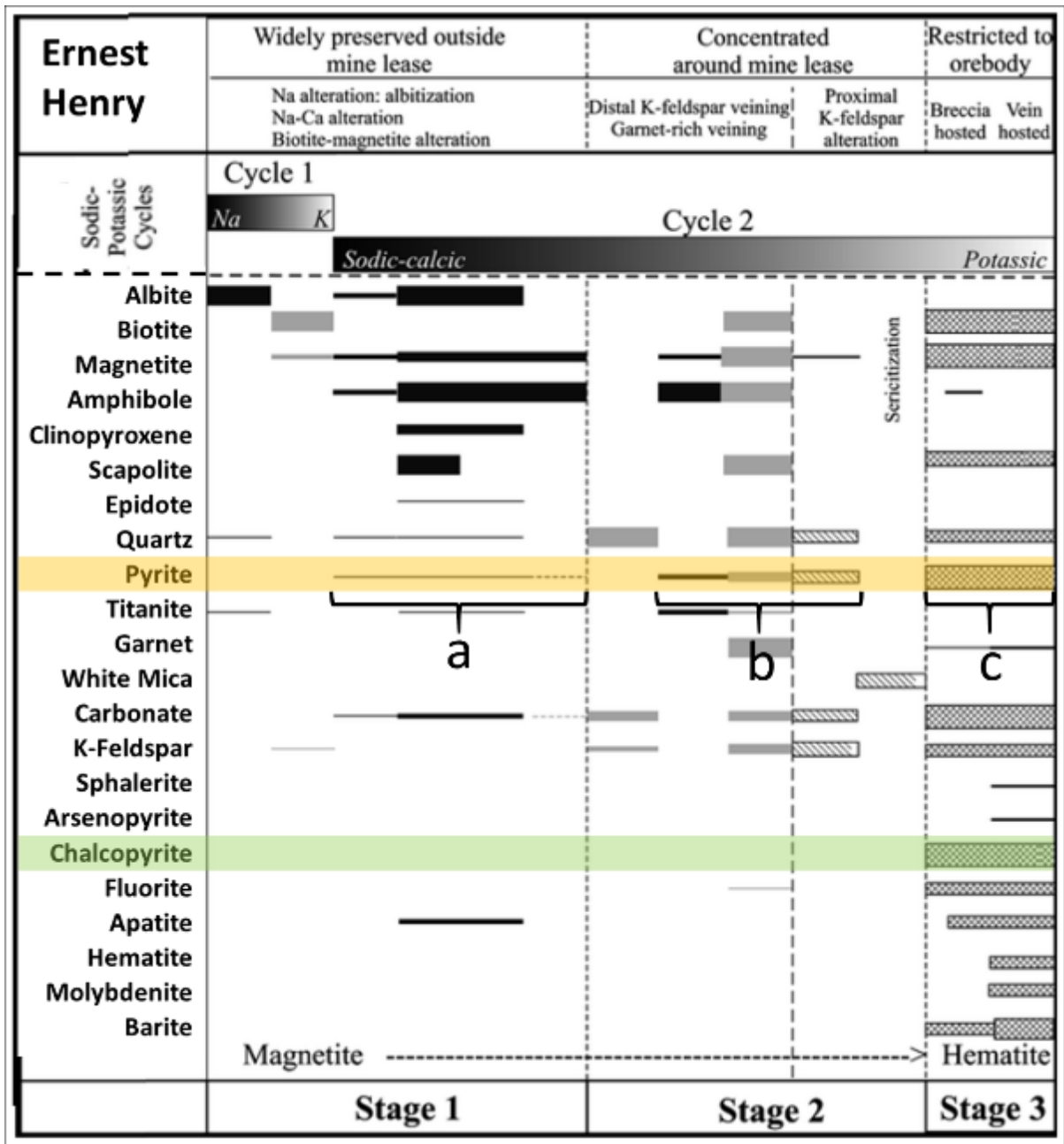


Figure 4: The succession of the three major mineralisation and alteration stages of the EH ore body adapted from Mark et al. (2006). Note the pyrite phases (a and b) that pre-date stage 3 mineralisation, and pyrite phase c that is coexistent with main (chalcopyrite) mineralisation stage 3.

METHODS

Free gold is the key subject of this study, so the parameters and methods in acquiring free gold data is important. The classic ‘nugget effect’ of gold should be noted as it was evident at the micro-scale (e.g. Figure 12a). Each gold grain was defined on the merit that it was completely separated to any neighbouring gold grains.

Sample Collection & Preparation

Field work was completed at EH Mining during March 2017. Twenty two samples were selected from three near-horizontal drill cores (EH768, EH859, and EH864) from the 1475 Level (Figure 3). Assay data was used to target zones of different ore grade and host lithology. Textural descriptions of pyrite used by A. Foster et al. (2007) were used in this study including, a) Disseminated Pyrite, b) Porphyroblastic Pyrite, and c) Vein-infill Pyrite (Figure 5). Birds-wing Pyrite is another observed texture located in the periphery of the ore body (Figure 5d). However, assay data indicated that these zones are depleted in Au and Cu, and therefore the Birds-wing Pyrite has not been considered.

Samples were sent to Ingham Petrographics to be made into polished thin sections. Petrography of the samples were examined under the Olympus BX51 optical microscope, followed by further analysis with the FEI Quanta 600 and a Philips XL30 FEG Scanning Electron Microscope (SEM) supported with Energy-Dispersive X-ray Spectroscopy (EDS).

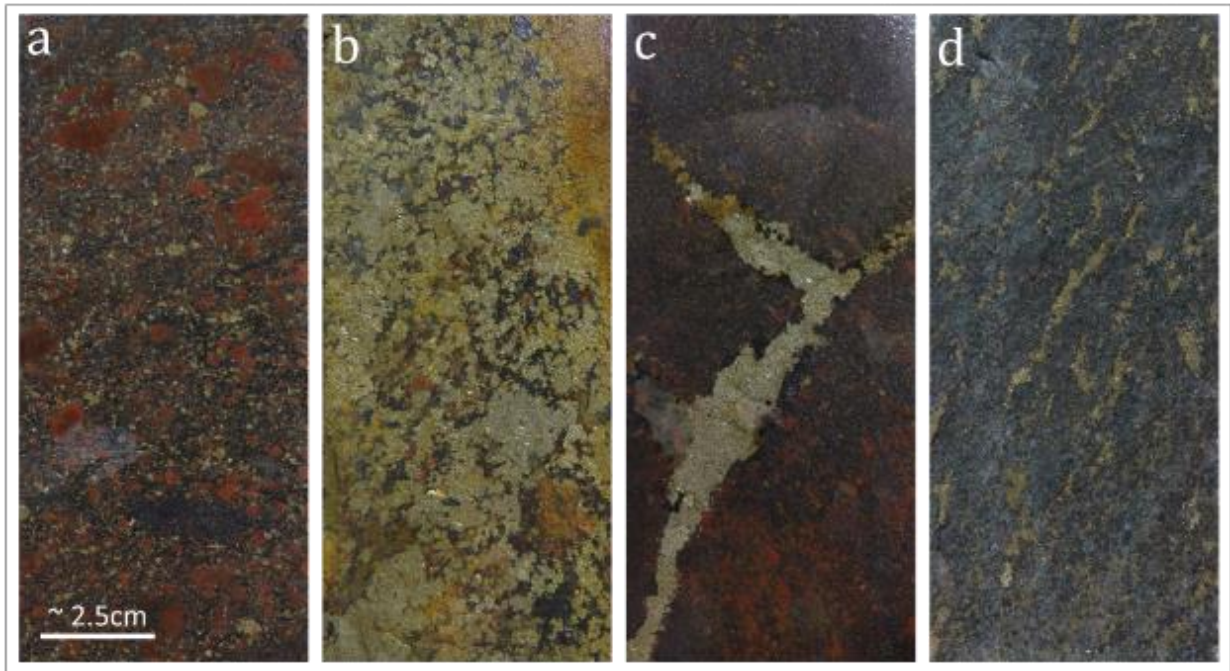


Figure 5: Half-core images of targeted pyrite textures: a) Disseminated Pyrite, the most common ore texture throughout the drill core. b) Porphyroblastic pyrite, which produces distinct aggregated textural zones in the orebody independent of the deposit-scale pyrite-chalcopyrite zonation. c) Vein-infill Pyrite. d) Dilatational ‘Birds-wing’ Pyrite, infill from trans-tensional shearing at the periphery of the orebody.

SEM – Mineral Liberation Analysis

The FEI Quanta 600 equipped with a tungsten filament and supported with an EDS system was used to detect free gold and the associated minerals. The SEM was used in back-scattered electron (BSE) mode to generate high quality grey-scale images of gold grains and the associated minerals (Figure 6a), the EDS validated the gold and minerals by their elemental composition (Figure 6b), and the MLA software generated colour-coded mineral maps (Figure 6c). Adjustments to the MLA software were made in attempt to increase the detection of the finer gold grains; the spot scan interval was changed from 5 μm to 2 μm to optimise detection of small gold particles.

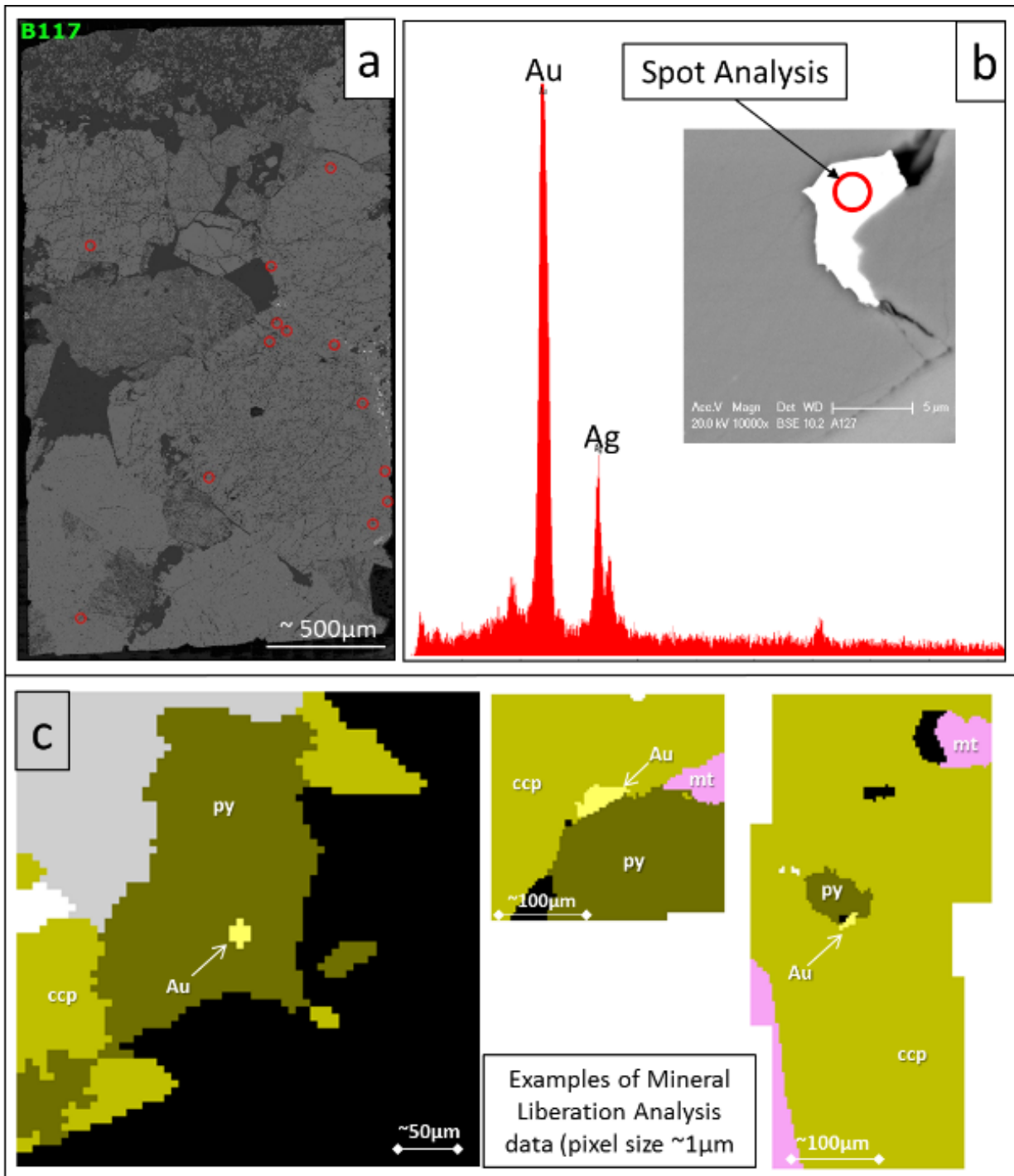


Figure 6: a) Example of a high quality BSE map taken from Sample B117. The red circles are locations of identified free gold. b) Example of a spectrum count taken by the EDS to validate a gold grain. Note the presence of accessory Ag in the non-quantitative EDS analysis (see discussion). c) Example of an MLA image taken from one of the common gold locations adapted from Lilly et al. (2017).

Each gold grain identified by the MLA was cross-checked by visual observations with the FEI Quanta 600 SEM and the EDS to ensure the MLA had accurately classified the grain. This was important in particular for sylvanite (Ag, Au) Te₂, as only 2 out of 20 sylvanite grains were correctly classified by the MLA.

The XL30 SEM was used to capture high-resolution images of each identified gold grain and the surrounding minerals in BSE mode with an acceleration voltage of 20.0 kV. As with the FEI Quanta 600, EDS was used to validate all minerals associated to the gold grains. The enhanced magnification of the XL30 comparable to the FEI Quanta 600, provided a more detailed resolution of the grain size and textural setting of the associated minerals, as well as detecting sub-microscopic (<1 µm) grains.

LA-ICP-MS

ICP-MS analysis was used to collect both quantitative geochemical data for chalcopyrite, magnetite and pyrite, and semi-quantitative geochemical maps of pyrite to investigate if the chemistry of chalcopyrite, pyrite, and magnetite is associated with gold. Twenty-five elements were analysed for their common association with hydrothermal systems (Table 1). Priority elements (Ag, As, Au, Co, Ni) were set with longer acquisition time to ensure sufficient data was collected. Spot size (30 to 80 µm diameter) was maximised and restricted depending on the size of the mineral grain, and to avoid inclusions or neighbouring minerals that would contaminate the data (Figure 7d).

Approximately 500 quantitative spot analyses were taken from thirty seven mineral grains including, pyrite (23), chalcopyrite (7), and magnetite (7); the spot locations for the pyrite samples can be found in Appendix 3.b. Spot analysis on the pyrite samples were distributed across two linear paths perpendicular to each other to investigate any changes in trace element concentrations (Figure 7a). Chalcopyrite and magnetite were examined with 4 or 5 random spots on gold-hosted and gold-absent grains (Figure 7b, c).

Three standards were used with the ICP-MS including, NIST610 (Na-Ca-Al-Si rich glass), GSD-1G (Fe-Al-Si basaltic-like glass), and MASS-1 (Fe-Cu rich press powdered sulphide precipitate). The holistic approach in combining the different chemical compositions of GSD-1G and NIST610, and the different texture of MASS-1 (pressed powder) improved the consistency and reliability of the data when correcting for instrumental drift in the Iolite software.

The Trace Element_IS data reduction scheme (DRS), a function in Iolite, was used to calculate the trace element compositions of chalcopyrite, pyrite, and magnetite with the MASS-1 standard. Additionally, the lower detection limits of the Mass Spectrometer were processed in Excel to discredit any values that returned lower than this limit. Trace element maps of pyrite (6) were generated in Iolite using the Trace Element DRS function. The semi-quantitative scan method created a visual representation of the trace element distribution (e.g. Figure 15).

Table 1: Overview of the parameters applied to the NewWave LA-ICP-MS system for pyrite and chalcopyrite (left column) and magnetite (right column).

<i>LA-ICP-MS Parameters</i>		
	<i>Sulphides</i>	<i>Fe-Oxides</i>
<i>Brand and Model</i>	<i>NWR 213-7900 ICP-MS</i>	<i>NWR 213-7900 ICP-MS</i>
	<u>Laser</u>	
<i>Spot Size</i>	<i>30 – 80 μm</i>	<i>40 μm</i>
<i>Laser Fluence</i>	<i>~4.5 J/cm-2</i>	<i>~7.5 J/cm-2</i>
<i>Laser Warm Up</i> <i>(background collection)</i>	<i>30 s</i>	<i>30 s</i>
	<u>Data Acquisition Parameters</u>	
<i>Data Acquisition Protocol</i>	<i>Time-resolved analysis</i>	<i>Time-resolved analysis</i>
<i>Cleaning Method</i>	<i>Firing 5 pulses followed by washout</i>	<i>Firing 5 pulses followed by washout</i>
<i>Scanned Masses</i>	<i>²⁹Si, ³⁴Si, ⁴³Ca, ⁵¹V, ⁵⁵Mn, ⁵⁷Fe, ⁵⁹Co, ⁶⁰Ni, ⁶³Cu, ⁶⁶Zn, ⁷⁵As, ⁷⁷Se, ⁹⁵Mo, ¹⁰⁷Ag, ¹¹Cd, ¹¹⁸Sn, ¹²¹Sb, ¹²⁵Te, ¹⁸²W, ¹⁹⁷Au, ²⁰⁵Ti, ²⁰⁸Pb, ²⁰⁹Bi, ²³²Th, ²³⁸U</i>	<i>²⁹Si, ³⁴Si, ⁴³Ca, ⁵¹V, ⁵⁵Mn, ⁵⁷Fe, ⁵⁹Co, ⁶⁰Ni, ⁶³Cu, ⁶⁶Zn, ⁷⁵As, ⁷⁷Se, ⁹⁵Mo, ¹⁰⁷Ag, ¹¹Cd, ¹¹⁸Sn, ¹²¹Sb, ¹²⁵Te, ¹⁸²W, ¹⁹⁷Au, ²⁰⁵Ti, ²⁰⁸Pb, ²⁰⁹Bi, ²³²Th, ²³⁸U</i>
<i>Background Collection</i>	<i>30 s</i>	<i>30 s</i>
<i>Ablation Time</i>	<i>30 s</i>	<i>30 s</i>
<i>Acquisition Time</i>	<i>69.601s (spot duration)</i>	<i>69.601 s (spot duration)</i>
	<i>79.927s (scan duration)</i>	<i>79.927 s (scan duration)</i>
<i>Washout</i>	<i>20 s</i>	<i>20 s</i>
	<u>Standardisation and Data Reduction</u>	
<i>Primary Standard</i>	<i>NIST610</i>	<i>NIST610</i>
<i>Secondary Standard</i>	<i>MASS_1</i>	<i>MASS_1</i>
<i>Tertiary Standard</i>	<i>GSD-1G</i>	<i>GSD-1G</i>
<i>Data reduction Software</i>	<i>Iolite</i>	<i>Iolite</i>

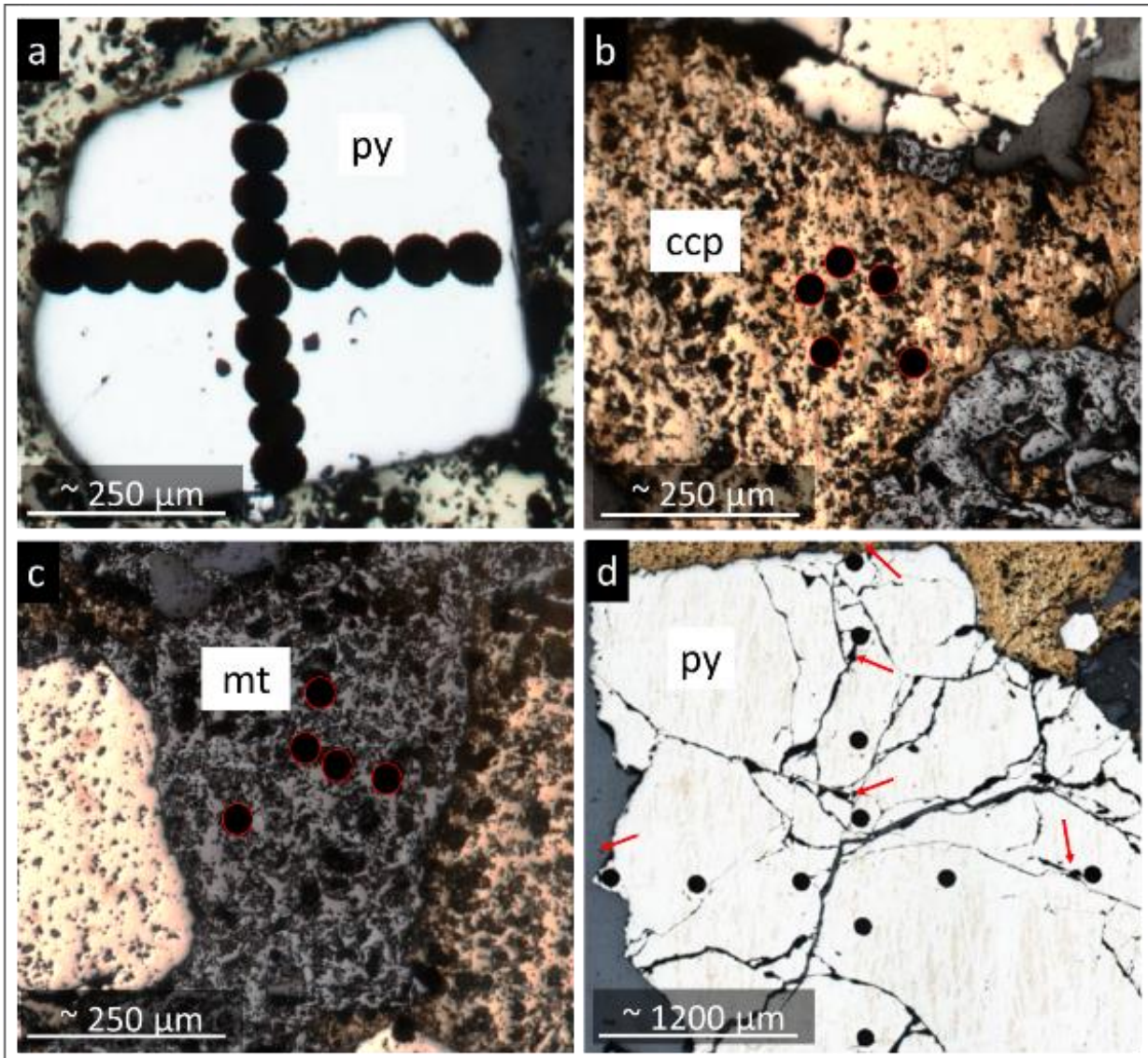


Figure 7: Distribution of spot locations for a) pyrite, b) chalcopyrite, and c) magnetite. Note the two linear and perpendicular spot lines for pyrite used to detect change in the relative elemental composition. d) Red arrows represent locations that were avoided because of inclusions, microfractures, or other minerals in contact with the target mineral (pyrite).

OBSERVATIONS & RESULTS

Petrology

The suite of 22 samples varied from *iv* lithology located at the edge of the ore body (Figure 8a), to *fv1* and *fv2* lithology in the ore zone (Figure 8b, c); each samples can be found in Appendix 1.b, and a full description of the main lithologies can be found in Appendix 1.a. The samples are considered representative of the ore from the 1475 Level, all consisting of strongly K-feldspar altered Mount Fort Constantine Volcanics with varying proportions of magnetite, chalcopyrite, pyrite, calcite, quartz, and biotite (Figure 8). No free gold was observed by reflected light optical microscopy. Petrographic observations did not identify any unusual paragenetic timing between the major constituent minerals, and it is considered that the samples have the same ore paragenesis as described by Mark et al. (2006) in Figure 4.

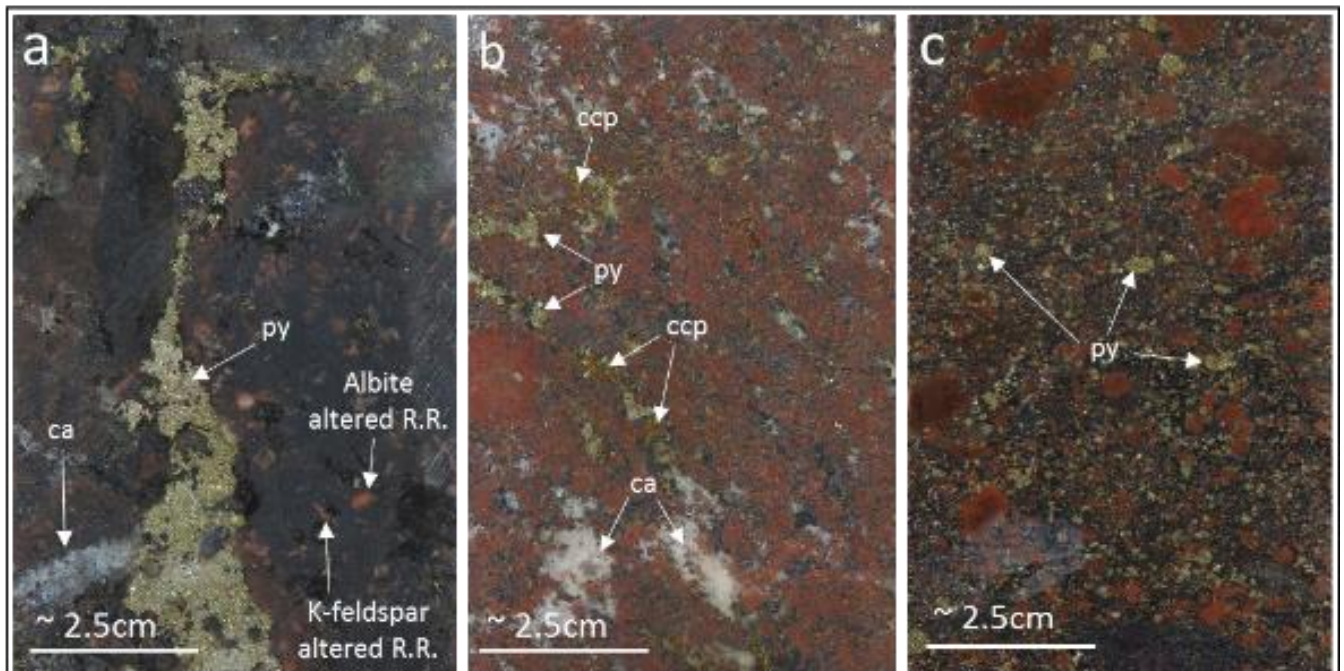


Figure 8: Three rock types sampled from the 1475 Level: a) *iv*, b) *fv1*, and c) *fv2*. Black mineral = magnetite ± biotite, red mineral = red rock (R.R.) alteration of albite and K-feldspar. Note the association between clast/matrix ratio and the progressive increase in sulphide content from *fv1* to *fv2*.

Disseminated, Porphyroblastic, and Vein-infill Pyrite textures can be present together in a single 1 m core interval (Figure 9), so only the dominant pyrite texture and lithology are listed in Table 2. There is no evidence that pyrite textures are associated with host lithology.

Table 2: The dominant pyrite texture and lithology recorded for each sample. Note the potential bias when classifying the dominant pyrite texture; Porphyroblastic and Vein-infill Pyrite are generally larger grains that overshadow Disseminate Pyrite.

A Samples (EH768)	Texture	Lithology	B Samples (EH859)	Texture	Lithology	C Samples (EH864)	Texture	Lithology
A034	<i>di</i>	<i>fv2</i>	B080	<i>po</i>	<i>fv2</i>	C002	<i>vi</i>	<i>fv1</i>
A036	<i>vi</i>	<i>fv2</i>	B117	<i>vi</i>	<i>fv2</i>	C045	<i>po</i>	<i>fv1</i>
A121a	<i>vi</i>	<i>fv2</i>	B194	<i>vi</i>	<i>fv1</i>	C071	<i>po</i>	<i>fv1</i>
A121b	<i>vi</i>	<i>fv2</i>	B204	<i>vi</i>	<i>fv2</i>	C077	<i>vi</i>	<i>iv</i>
A127	<i>vi</i>	<i>fv2</i>	B207	<i>di</i>	<i>fv2</i>	C125	<i>vi</i>	<i>fv2</i>
A155	<i>po</i>	<i>fv1</i>	B222	<i>di</i>	<i>fv2</i>	C144	<i>po</i>	<i>fv2</i>
A157	<i>vi</i>	<i>fv1</i>	B247	<i>po</i>	<i>iv</i>			
A168	<i>vi</i>	<i>fv2</i>						
A177	<i>po</i>	<i>fv2</i>						

Texture code: *di* = Disseminated Pyrite, *po* = Porphyroblastic Pyrite, *vi* = Vein-infill Pyrite.

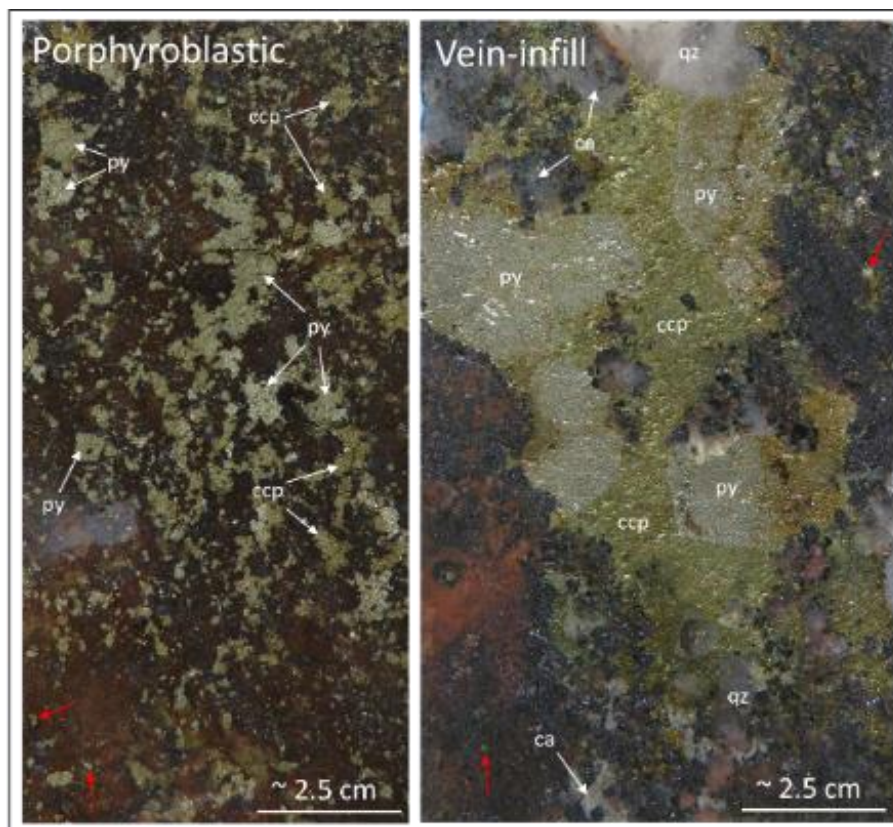


Figure 9: Pyrite textures in half-core samples A036 (left) and C071 (right) displaying the textural difference between Porphyroblastic and Vein-infill pyrite. Disseminated pyrite (red arrows) are recorded in Porphyroblastic and Vein-infill zones and are most evident in and around the larger red rock altered clasts.

Micro-scale features of the pyrite textures can be used to distinguish the different pyrite textures observed in the core samples (Figure 5). Disseminated Pyrite is characterised by a solid internal structure and relative small (50 to 500 μm) sub-euhedral to rounded grains (Figure 10a), and is often concealed by overprinting of Porphyroblastic and Vein-infill Pyrite (Figure 9; Figure 10b). Porphyroblastic Pyrite is characterised by grains that are 300 to 3000 μm with typically rounded edges, and contain some internal fractures (Figure 10b, e). Vein-infill Pyrite are relatively large (2000 μm to cm scale) angular grains, and have a pervasive fracture network (Figure 10c, d). Chalcopyrite infill is identified in Vein-infill Pyrite, supporting the paragenesis of Mark et al. (2006) who interpreted that the main stage economic mineralisation post-dates most pyrite. The irregular grain boundaries and fractures observed in Porphyroblastic and Vein-infill Pyrite support both hypotheses of brecciation events that facilitated economic mineralisation.

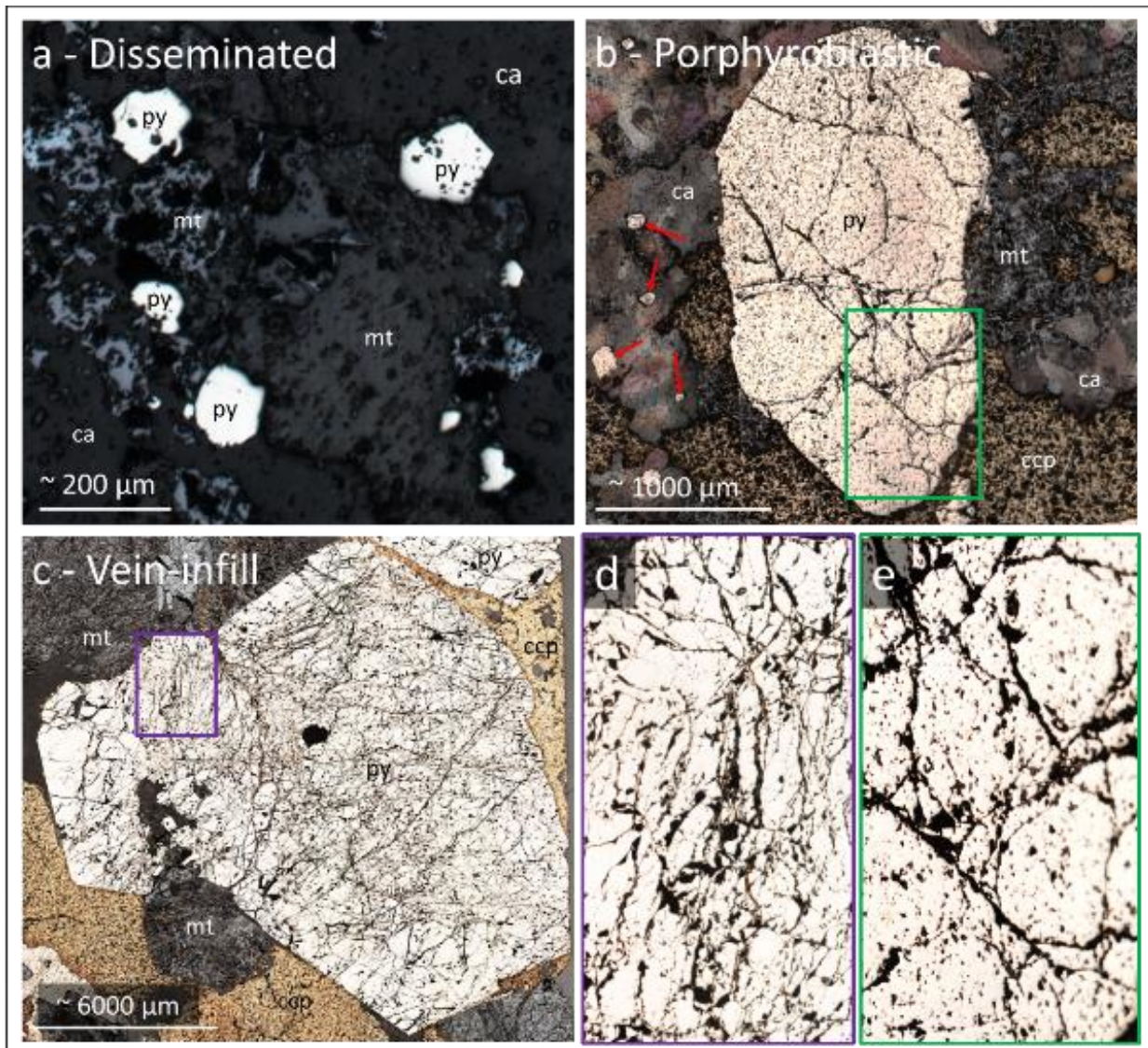


Figure 10: Reflected light optical images representing the three identified pyrite textures at the micro-scale. a) Disseminated pyrite, b) Porphyroblastic Pyrite and Disseminated Pyrite (red arrows), and c) Vein-infill Pyrite; d and e) inflated boxes of the Porphyroblastic and Vein-infill Pyrite representing the difference in fracture density. Note the difference between the rounded edges of Porphyroblastic Pyrite and the angular edges and more pervasive fracture network of Vein-infill Pyrite.

SEM Observations of Free Gold

Free gold grains ($n = 155$) were observed in 20 of the 22 polished thin sections (Table 3); for information and images of individual grains see Appendix 2.a and 2.b. Pyrite was the most common mineral of the 11 minerals in contact with free gold (Figure 11b). A strong association was also observed with free gold and chalcopyrite, illustrating a relationship between chalcopyrite, pyrite and free gold. Pyrite associated with free gold was observed in

Vein-infill Pyrite (72%), Disseminated Pyrite (16%), and Porphyroblastic Pyrite (12%).

Sylvanite (2 grains) was the only gold-bearing mineral identified (sample A121b), and concurs with the observations of A. Foster et al. (2007), who concluded that ~95% of the gold is in the form of native free gold, and the remaining 5% as other gold-bearing minerals such as sylvanite or as invisible gold.

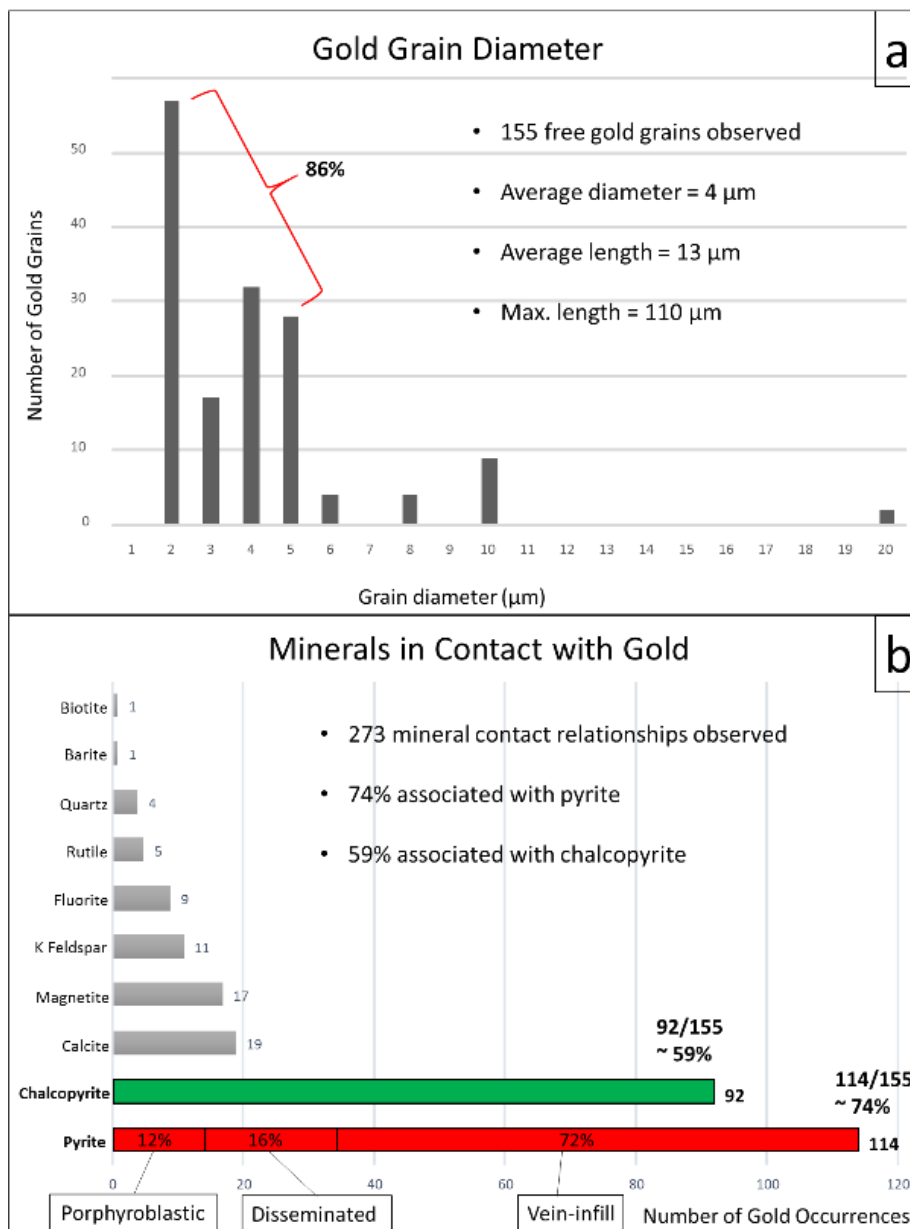


Figure 11: a) Average gold grain diameters (µm), n = 155. b) Observed frequency of mineral contacts with free gold grains. Note the observed gold grains could have more than one mineral contact. Additionally, minerals in contact were observed in two dimensions and associations in the third dimension may also exist.

The average diameter and length of free gold ($n = 155$) was $4 \mu\text{m}$ and $12 \mu\text{m}$ (Table 3). The maximum measured length of a gold grain was $110 \mu\text{m}$ (Table 3), and observations of gold grain textures (Figure 12; Figure 13; Figure 14) indicate that the variable grain sizes are influenced by these textures, i.e. “hairline fractures” in pyrite host elongated gold grains that are in microfractures typically $<2 \mu\text{m}$ in diameter (Figure 12c, d). It is unknown if any other minerals are hosted in these hairline fractures as the SEM MLA was unable to detect minerals $<2 \mu\text{m}$ in diameter, thus limiting investigation into the observed sub-microscopic invisible gold (Figure 12b).

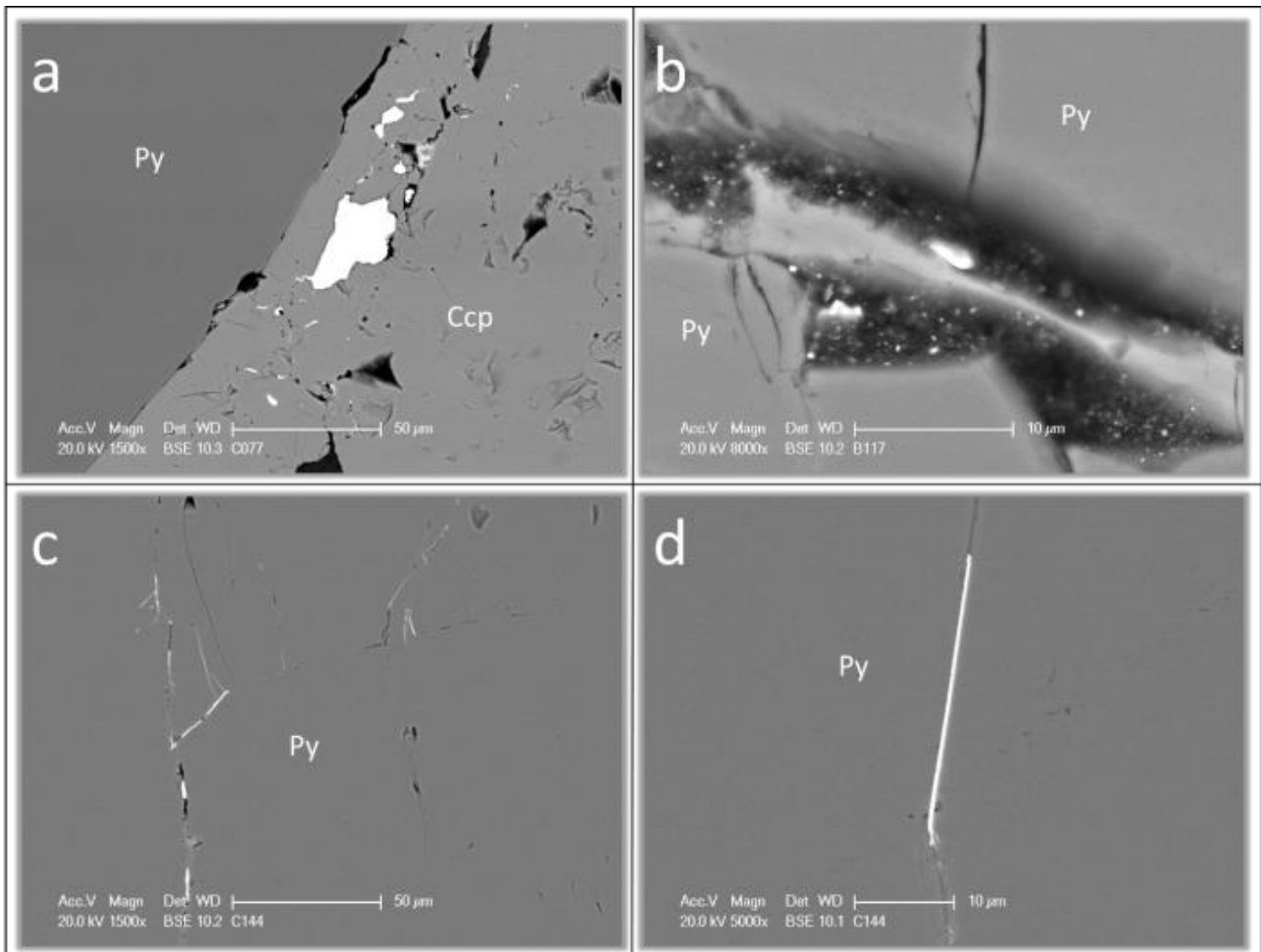


Figure 12: SEM images taken in BSE mode representing the range of observed gold textures and precipitation styles. Gold appears white in the images. a) Gold micro-cluster within chalcopyrite. b) Sub-microscopic gold nano-cluster in pyrite grain within a recessive area of the polished thin section. c) Gold hosted in pyrite hairline fractures. d) Close up of a gold-bearing hairline fracture

Table 3: Mineralogical, textural, and lithological associations of free gold grains from drill core EH768 (A samples), EH859 (B samples), and EH864 (C samples). See Appendix A for more details on individual gold grains.

<i>Sample</i>	<i>Number of Gold Grains</i>	<i>Mean Length (µm)</i>	<i>Mean Diameter (µm)</i>	<i>Mineralogical Association</i>	<i>Textural Site</i>	<i>py Texture</i>
A034	2	7	2	ca/ccp/py/qz	mf	di (1)
A036	10	11	4	ba/ca/ccp/fl/mt/py	cm (1), mf (9)	di (1) vi (9)
A121a	0	-	-	-	-	-
A121b	10	16	4	ca/ccp/py/qz	dp (1), mf (10)	vi (11)
A127	15	13	4	ca/ccp/fl/py	dp (1), cm (4), mf (10)	vi (15)
A155	1	5	4	ccp/py	cm (1), mf (9)	di (1)
A157	0	-	-	-	-	-
A168	17	13	4	ccp/kf/mt/py/ru	cm (1), dp (2), mf (14)	vi (13)
A177	2	9	4	ccp/py	mf	po (2)
B080	8	13	7	ccp/mt/py	cm (2), dp (6)	di (2)
B117	24	11	4	ccp/py	mf	vi (24)
B194	7	26	3	ccp/py	cm (1) mf (6)	di (1) vi (5)
B204	5	16	4	py	mf (1) dp (4)	vi (5)
B207	9	10	4	ca/ccp/mt/py/qz	cm (2), mf (7)	di (7)
B222	1	10	5	ccp/kf/py	cm	di (1)
B247	1	5	2	ccp/py	mf	po (1)
C002	1	5	3	ca/py	cm	di (1)
C045	3	10	4	ccp/py	mf	po (3)
C071	8	16	7	ca/ccp/py/qz	cm (1), dp (3), mf (4)	po (8)
C077	6	11	4	ccp	dp	-
C125	8	4	3	bi/ccp/kf/py	dp (3), mf (5)	vi (8)
C144	17	10	3	bi/ca/ccp/kf/py	dp (1), cm (2), mf (14)	di (3) po (14)
22 samples	155	12	4		cm (13) dp (27) mf (115)	di (18) po (14) vi (82)

Mineral codes: ba = barite, bi = biotite, ca = calcite, ccp = chalcopyrite, fl = fluorite, kf = K-feldspar, mt = magnetite, py = pyrite, q = quartz, ru = rutile.

Textural codes: cm = contact margin, dp = dissolution pit, mf = micro fracture

The host mineralogy and textural setting of free gold was observed in six different settings which are listed below and displayed in Figure 13 and Figure 14:

- 1) **Pyrite (microfractures):** Pyrite microfractures (Figure 13a) with chalcopyrite infill represented 65% of observed gold. Microfractures are pervasive in Vein-infill Pyrite, moderate in Porphyroblastic Pyrite, and almost absent in Disseminated Pyrite.
- 2) **Pyrite (dissolution pits):** Hosted within pyrite grains with no association to any other minerals represented 16% of observed gold (Figure 13b). Note that this does not account for other minerals in the third dimension.
- 3) **Pyrite (contact margins):** Located at boundaries between pyrite and chalcopyrite represented 7% (Figure 13c). This style is most commonly associated with Disseminated Pyrite.
- 4) **Chalcopyrite:** Hosted within chalcopyrite represented 7% of observed gold (Figure 14a). All observed gold was hosted in chalcopyrite in sample C077.
- 5) **Magnetite:** Hosted within magnetite represented 5% of observed gold (Figure 14b).
- 6) **Calcite:** A single gold grain was observed in calcite (sample A034; Figure 14c).

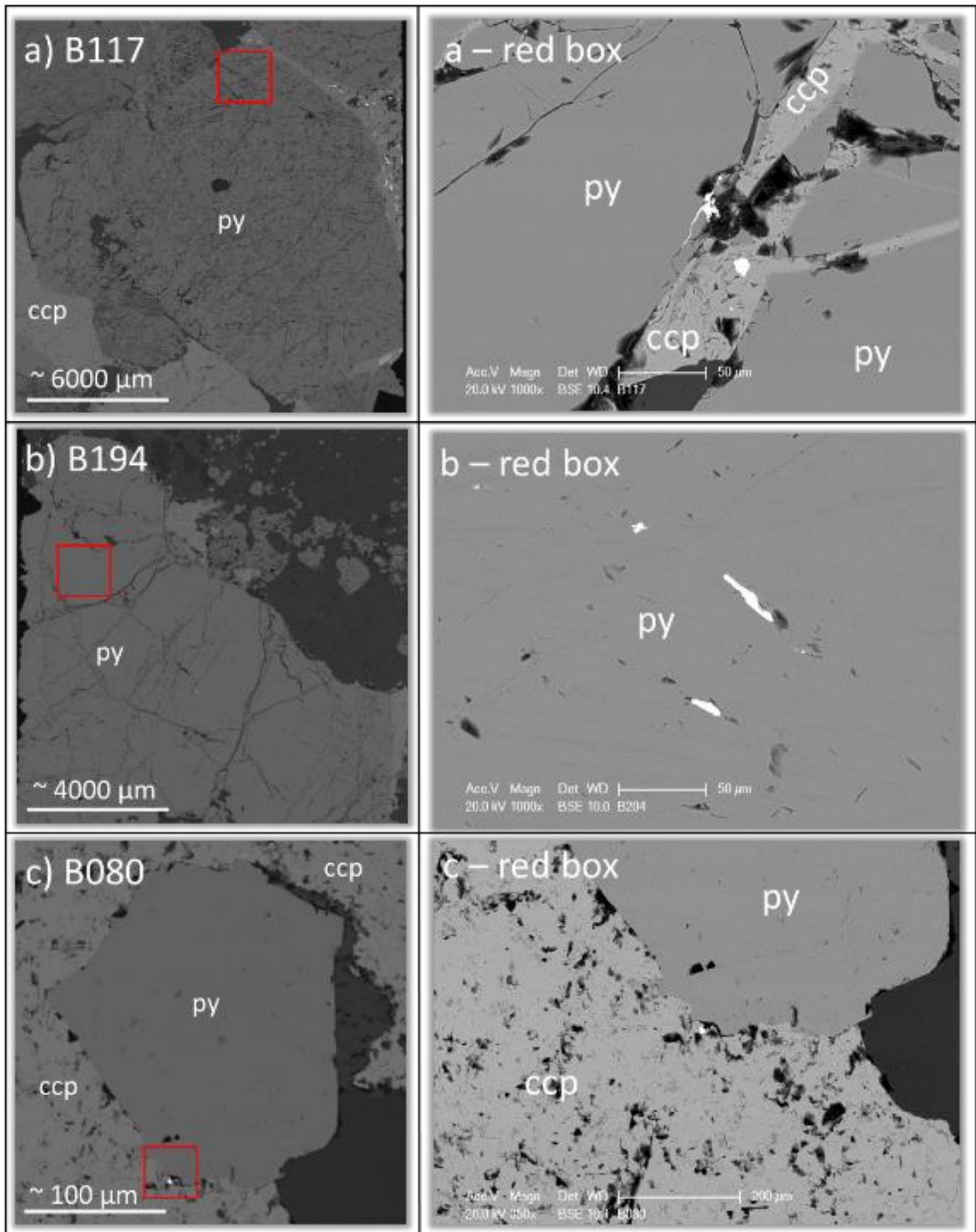


Figure 13: SEM images taken in BSE mode representing the textural settings of free gold associated with pyrite. Gold appears white in the images. a) Hosted in chalcopyrite veins in pyrite microfractures. b) Hosted in dissolution pits within the pyrite crystal lattice. c) Hosted at pyrite-chalcopyrite contact margins.

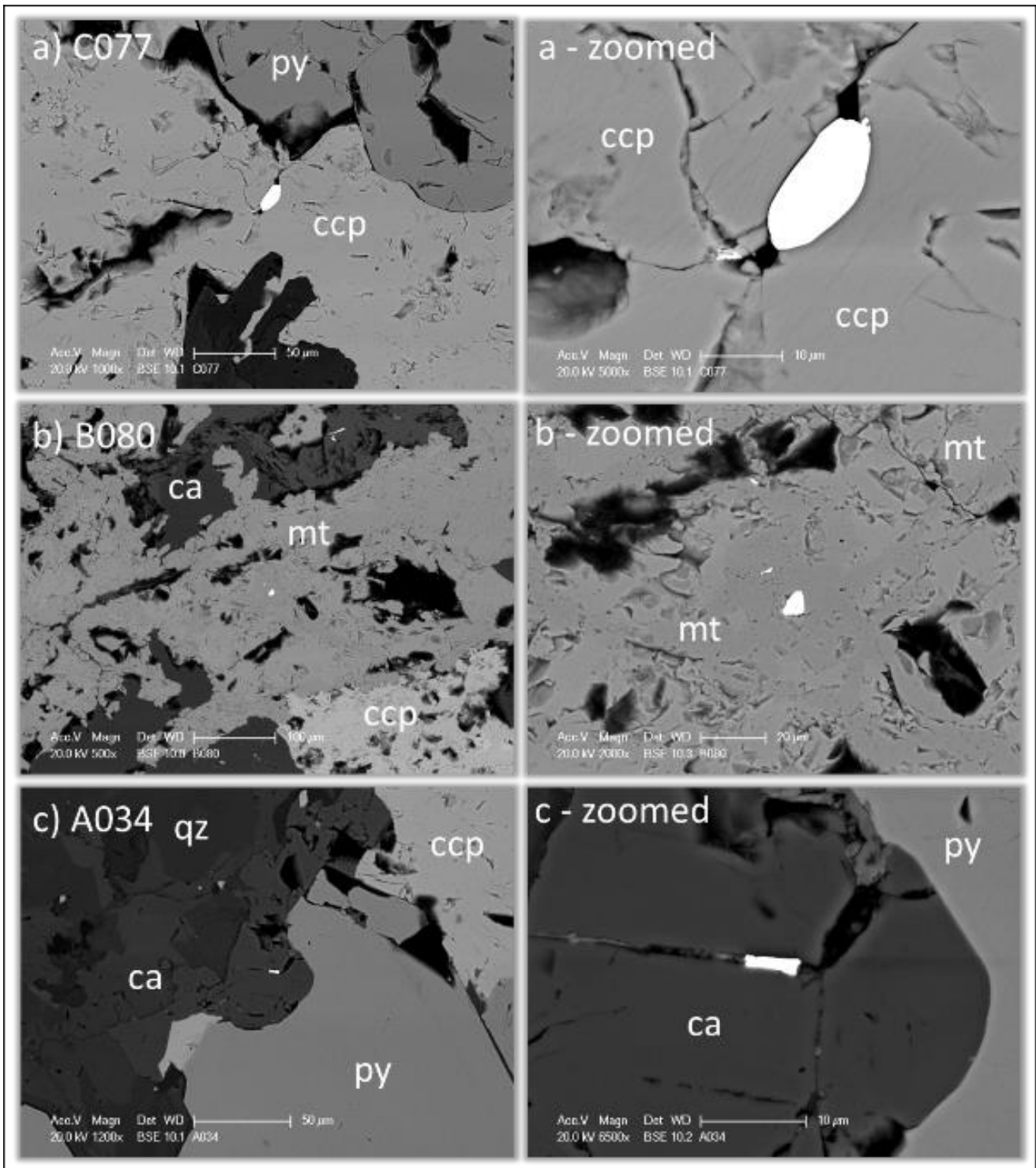


Figure 14: SEM images taken in BSE mode representing unique mineralogical settings of free gold. Gold appears white in the images. a) Hosted in chalcopyrite. b) Hosted in magnetite. c) Hosted in calcite.

LA-ICP-MS

PYRITE TRACE ELEMENTS

Six elemental maps of pyrite from gold-hosted and gold-absent grains were generated with ICP-MS line scan (Figure 15); Appendix 3.a. Only portions of Porphyroblastic and Vein-infill Pyrite grains were mapped. The maps were of suitable resolution to observe trace element variation in pyrite, and facilitated a focussed investigation using quantitative spot analysis. The average composition of pyrite has been investigated to identify whether pyrite texture (Table 4) or lithology (Table 5) affects the concentration and distribution of trace elements in pyrite. The data displays that Disseminated Pyrite is relatively enriched in As, Co, and Ni (Table 4). Data related to lithology displayed that the iv lithology has significantly higher Ni and lower As concentrations compared to pyrite samples from fv1 and fv2 lithology (Table 5), indicating spatial constraints of the distribution of Ni. Each pyrite texture displayed zonation of As-Co-Ni (Figure 15; Figure 16a; Figure 17).

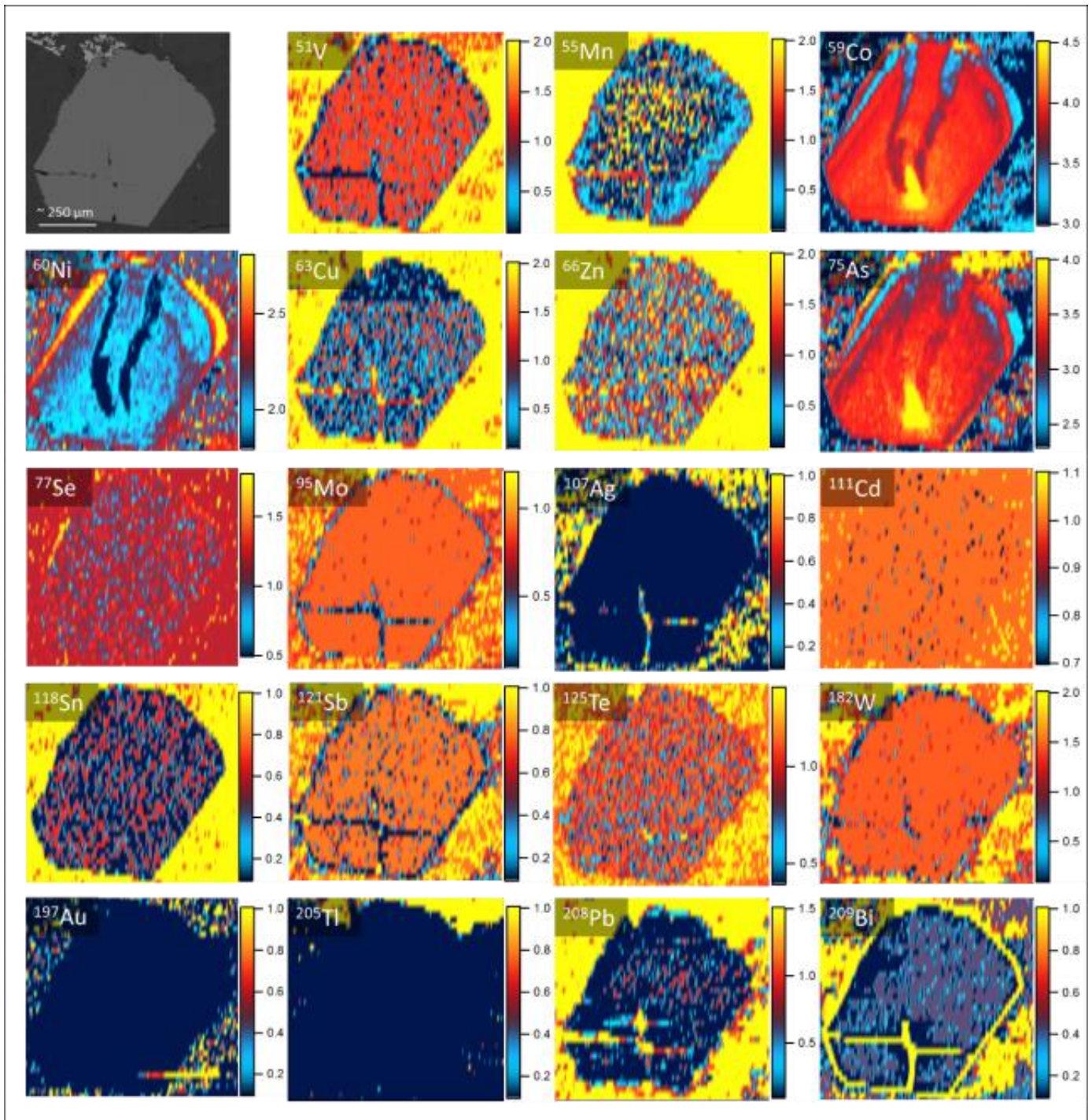


Figure 15: Example of all the elements mapped with ICP-MS for a Disseminated Pyrite grain (sample B117). Red indicates higher relative concentration (log scale ppm). Note the distinctive zonation of As, Co, and Ni.

Table 4: Pyrite chemistry (ppm) classified into the different pyrite textures. The colour represents the major (yellow), concentrated trace elements (pink), and other trace elements (green).

		Fe	S	S/Fe	Co	Ni	Co/Ni	As	Cu	Ag	Au
Disseminated n = 142	mean	3.13E+07	3.62E+06	0.12	14652.76	720.90	20.33	7572.22	251.09	5.79	0.16
	std	2.12E+07	2.42E+06	0.11	18953.27	2534.19	7.48	20963.47	1352.87	13.35	0.38
Porphyroblastic n = 105	mean	2.80E+07	3.27E+06	0.12	9834.75	87.33	112.62	485.20	277.90	4.45	0.53
	std	5.98E+06	9.57E+05	0.16	4770.49	123.34	38.68	1186.45	1338.23	15.23	1.29
Vein-infill n = 181	mean	9.92E+07	1.10E+07	0.11	8386.85	88.06	95.24	1527.60	239.92	37.84	3.02
	std	8.09E+06	1.20E+06	0.15	2165.29	53.86	40.20	1208.18	906.13	333.78	20.69

Table 5: Pyrite chemistry (ppm) classified into the different lithology. Note the As-poor and Ni-rich Porphyroblastic Pyrite hosted in *iv* lithology.

		Fe	S	S/Fe	Co	Ni	Co/Ni	As	Cu	Ag	Au
<i>iv</i> (po) n = 78	mean	2.51E+07	2.88E+06	0.12	8058.05	929.11	8.67	32.65	321.09	10.10	0.31
	std	5.03E+06	5.71E+05	0.11	5169.65	3085.07	1.68	29.10	1161.19	21.57	0.42
<i>fv1</i> (vi) n = 123	mean	8.19E+07	9.03E+06	0.11	11711.38	36.19	323.57	2355.02	206.62	71.04	3.80
	std	3.13E+07	3.36E+06	0.11	5701.18	11.81	482.85	3058.16	1289.85	471.58	24.51
<i>fv2</i> (po) n = 76	mean	2.63E+07	3.07E+06	0.12	8155.20	232.60	35.06	683.40	229.03	3.12	0.96
	std	9.86E+06	1.37E+06	0.14	5229.38	599.06	8.73	1358.27	1223.50	3.84	1.82
<i>fv2</i> (vi) n = 130	mean	8.20E+07	9.19E+06	0.11	12575.62	136.45	92.16	6803.44	273.46	3.85	1.50
	std	3.07E+07	3.45E+06	0.11	17510.79	67.51	259.38	19991.02	997.73	14.98	13.26

Table 6: The mean and standard deviations of As-Co-Ni for the different pyrite textures. Note the positive As and Co and the negative Ni core to rim ratio.

<i>Pyrite Texture</i>	<i>As (ppm)</i>			<i>Co (ppm)</i>			<i>Ni (ppm)</i>		
	Core	Rim	Core/Rim	Core	Rim	Core/Rim	Core	Rim	Core/Rim
<i>Disseminated (n = 142)</i>									
<i>Mean</i>	10226	4484	2.28	18431	10267	1.80	570	897	0.64
<i>std</i>	26381	11102		22561	12230		2236	2832	
<i>Porphyroblastic (n = 105)</i>									
<i>mean</i>	540	406	1.33	12693	5714	2.22	69	113	0.61
<i>std</i>	1394	791		3293	3343		53	179	
<i>Vein-infill (n = 181)</i>									
<i>mean</i>	1687	1317	1.28	9300	7181	1.30	75	106	0.71
<i>std</i>	1328	989		1804	2006		46	58	

PYRITE ZONATION

Zonation is the relative change in the distribution of elements, and in this study it refers to the change in As-Co-Ni that exists in the core, near-rim and rim. Disseminated Pyrite grains clearly exhibit Co enrichment in the core, As enrichment in the core or rim, and Ni enrichment in the rim (Figure 15; Figure 16a). Elemental maps for Porphyroblastic and Vein-infill Pyrite are not as clearly zoned (Figure 16b, c), however, element profiles constructed from quantitative spot data of Porphyroblastic and Vein-infill Pyrite are consistent with the As-Co-Ni zonation profiles in Disseminated Pyrite (Figure 17). A comprehensive table of the spot data can be viewed in Appendix B.

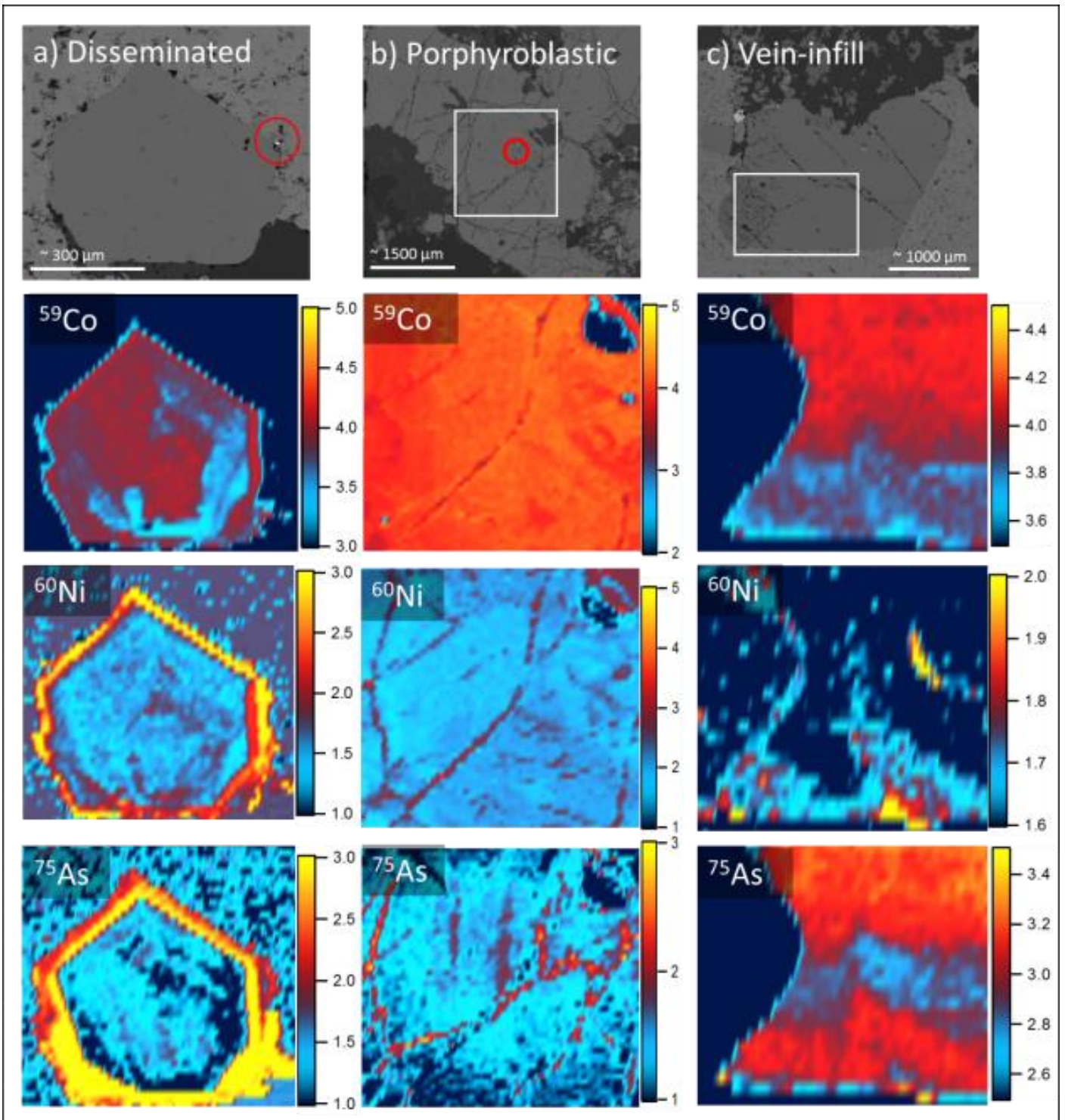


Figure 16: As-Co-Ni laser maps (log scale ppm) of the three pyrite textures (a) Disseminated, (b) Porphyroblastic, and (c) Vein-infill Pyrite. The white rectangles on the BSE images for (b) and (c) indicate the area of the grain where the elemental laser maps were generated. Red circles highlight the location of free gold grains.

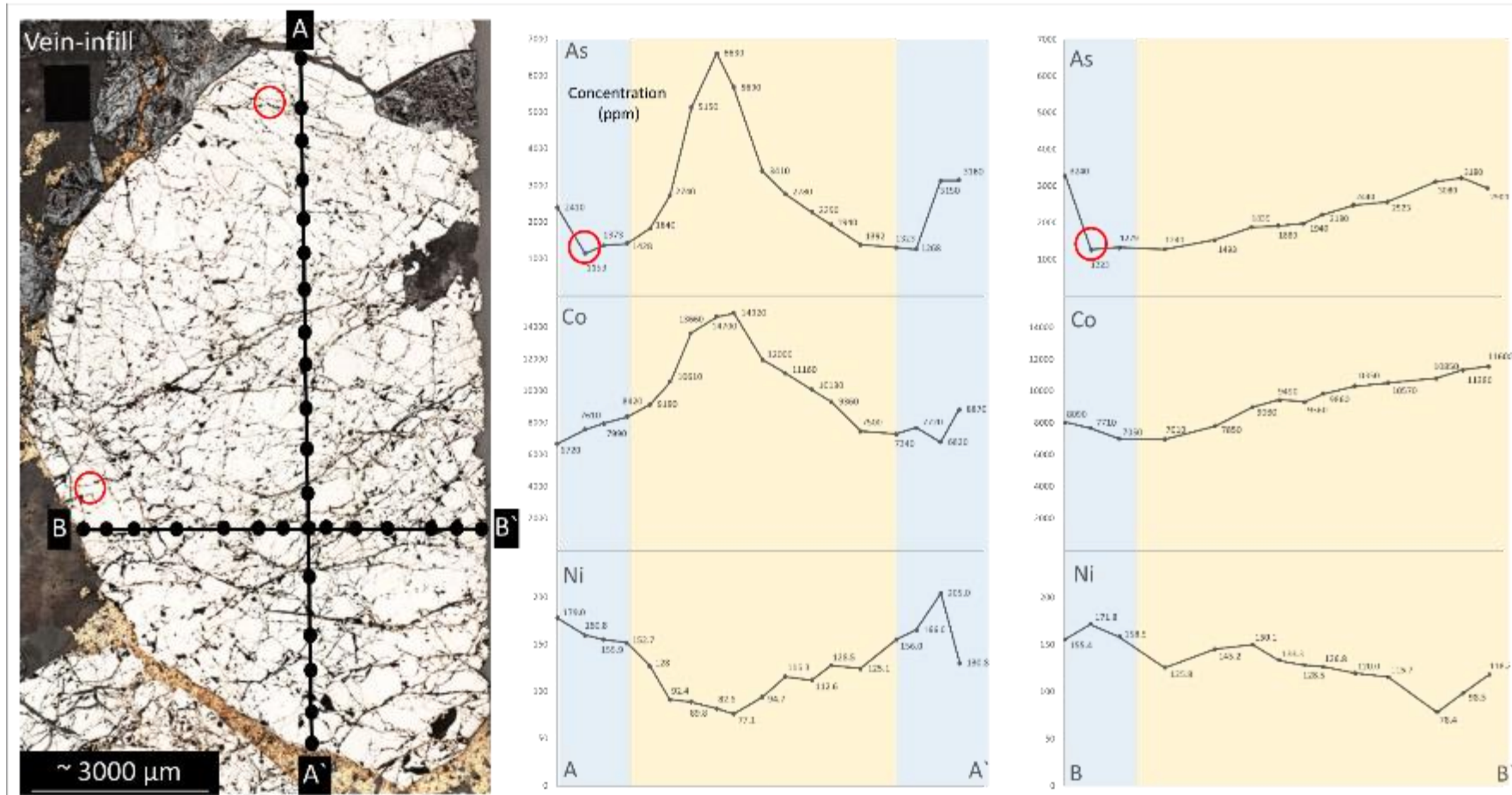


Figure 17: Vein-infill Pyrite grain (left optical image) with a complete (A – A`) and incomplete (B – B`) As-Co-Ni zonation transect. Blue and Orange have been used to represent the core (orange) and rim (blue) of the pyrite grain. The red circles are locations of free gold observed by SEM. The core was constrained to spots that had Ni < 150 ppm, and the rim was constrained to Ni > 150 ppm. There is an association between As and Co in the core which progressively diminishes towards the rim where there is an association between As and Ni. At no point is there a suspected association between Co and Ni. Note the location of free gold and the significant change in As proximal to the boundaries. The graph X axis labels correspond to the spot data (refer to Appendix B for data).

ARSENIAN PYRITE AND FREE GOLD

At the assay scale, there is a weak correlation ($R^2 = 0.28$) between As and Au (Figure 2), however, ICP-MS data does not support this correlation (Figure 18). The data indicates that a high As content in pyrite does not necessarily indicate the location of free gold.

Free gold is observed in the rim of Porphyroblastic and Vein-infill Pyrite, and although As is concentrated in the core of pyrite (Table 6), a significant and localised concentration of As was observed in the rim (Figure 17; Figure 19c). This data is consistent with Möller and Kersten (1994), who interpret that gold is not necessarily associated to the high As content of pyrite but in locations of high As concentration gradients.

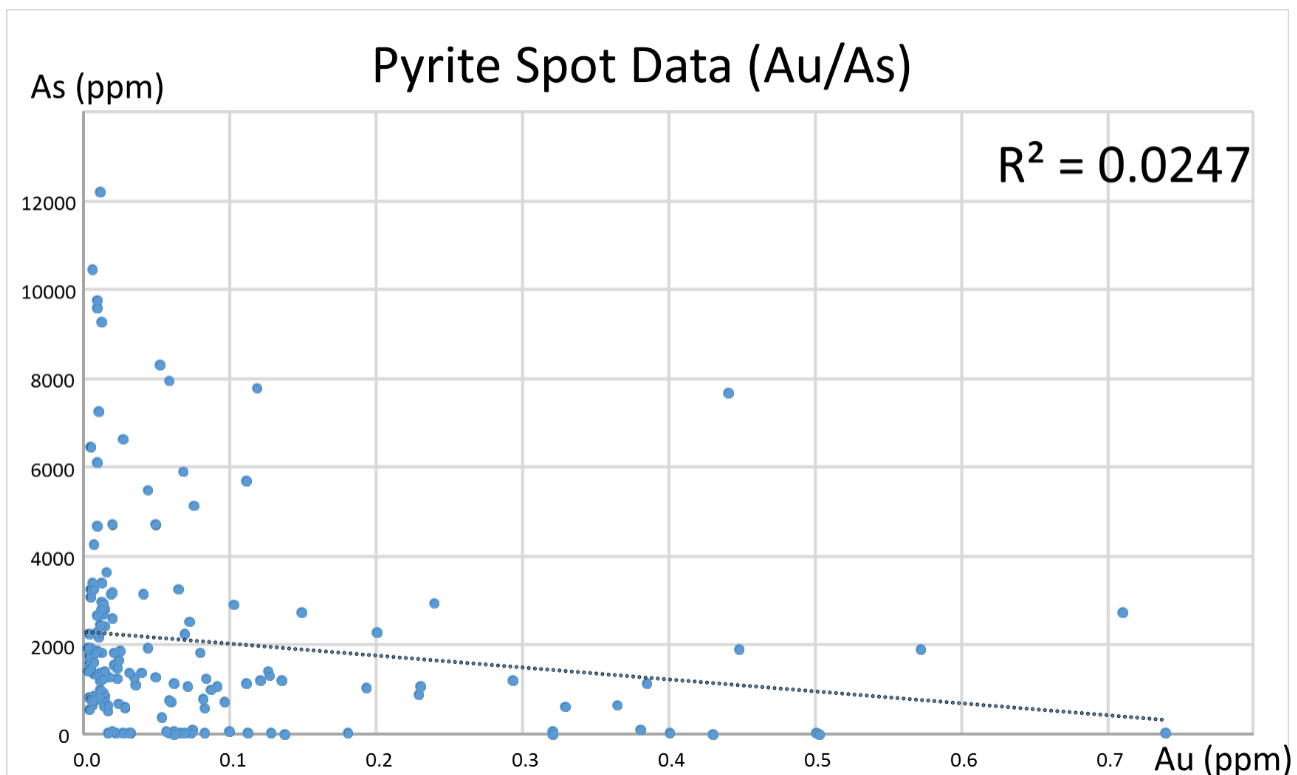


Figure 18: Pyrite ICP-MS spot data displaying no correlation between As and Au.

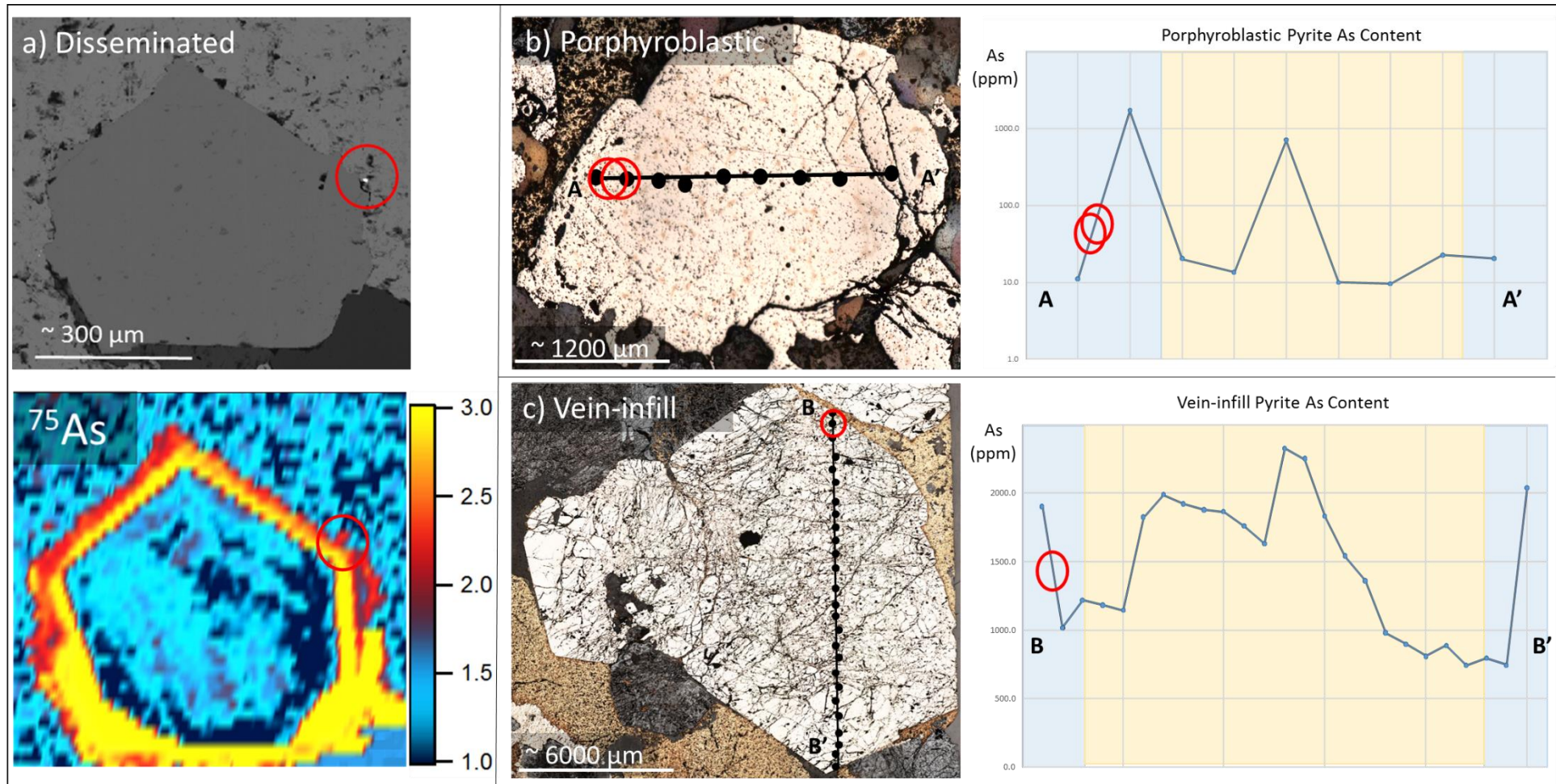


Figure 19: Spatial association of free gold (red circles) and As concentration gradient: a) Free gold located on the As-rich rim of Disseminated Pyrite. b and c) Free gold located on the sharp As gradients in Porphyroblastic and Vein-infill Pyrite. Blue and orange have been used to represent the core (orange) and rim (blue) of b and c. Note the common trend in where the free gold is located near the rim where the As gradient is high. These zones are not necessarily regions of the concentrated As, but are areas of increased As concentration gradients at the edge of grains.

OTHER FORMS OF GOLD

SEM analysis also detected gold in the form of free gold micro-grains and as invisible gold nano-inclusions (Figure 12a, b), hosted primarily in pyrite. ICP-MS has a greater resolution than the SEM enabling gold particles in the form of invisible gold nano-inclusions or solid solution to be quantifiably measured (Figure 20).

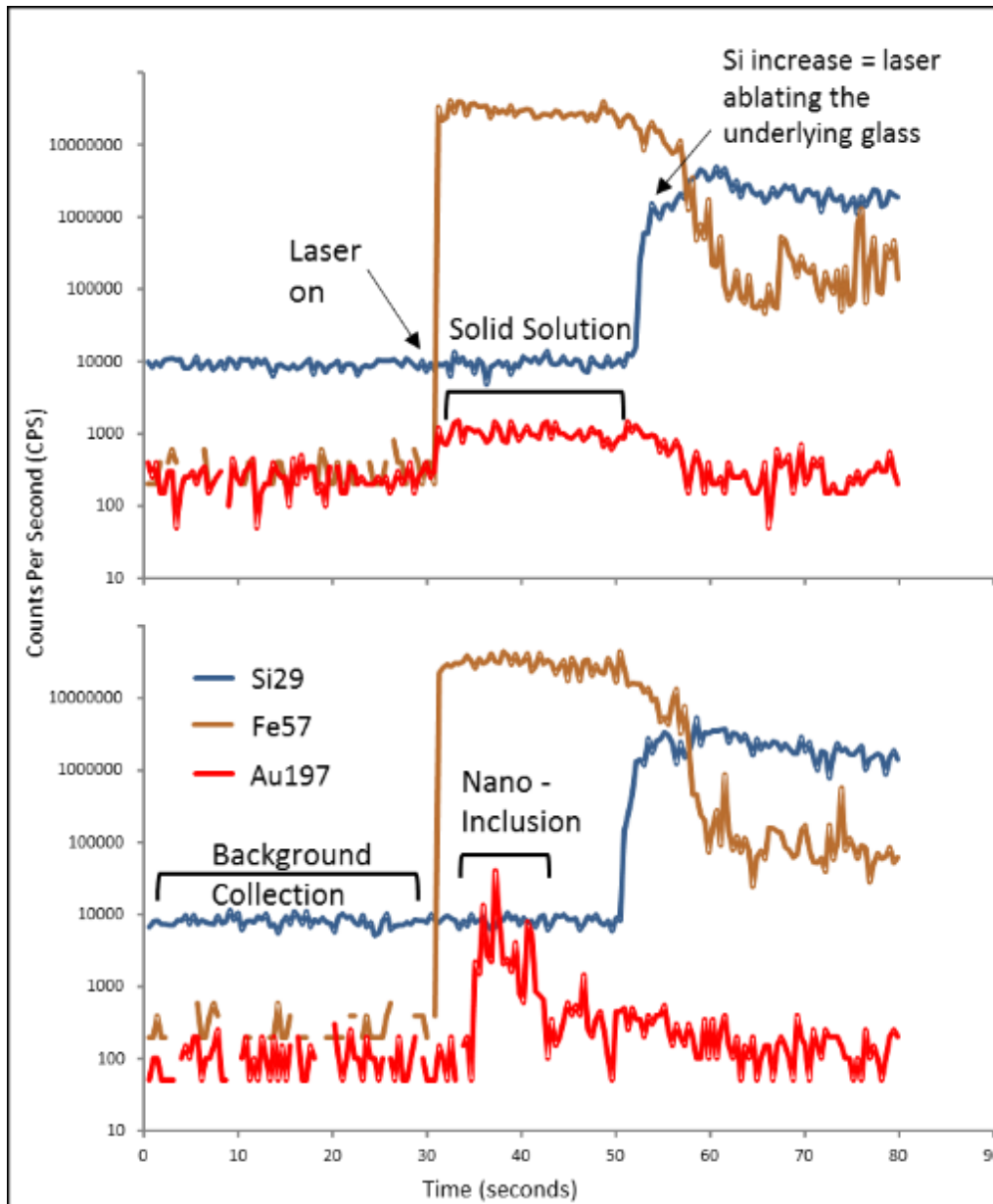


Figure 20: ICP-MS spot data from two pyrite samples of gold in solid solution (top) and nano-inclusions (bottom). The gold in solid solution maintains a relatively consistent concentration over the acquisition time, whereas the presence of gold as nano-inclusion is indicated by the data spike on the lower diagram. The Fe increase in counts per second (CPS) indicates that the laser is ablating pyrite, whereas the Si increase in CPS indicates when the laser has completely obliterated the pyrite and has started to ablate the glass thin section.

In pyrite, gold nano-inclusions are associated with relative enrichment in Ag, Bi, Cu, Sb, and Te. Solid solution gold within pyrite is associated with the same trace elements as nano-inclusions (Ag, Bi, Cu, Sb, and Te) as well as Cd, Mn, Pb, Sn, Tl, Se, and Zn.

Trace elements associated with invisible gold in chalcopyrite also vary depending on the form. Relative enrichments in Ag, As, Bi, Pb, Sb, Se, Sn, Te, and Tl are associated with nano-grains in chalcopyrite, while relative enrichments in Ag, Bi, Cd, and Te are associated with solid solution gold in chalcopyrite. Solid solution gold in magnetite is associated with relative enrichment in Bi, Cd, Pb, and Th.

Based on the ICP-MS data collected, an estimation of the total invisible gold was calculated to determine if further investigation was warranted. The calculation compared how much gold was identified as free gold and invisible gold in both pyrite and chalcopyrite, and can be found in Appendix 4. Gold concentrations were calculated to be in trace form of invisible gold in pyrite (1.6%), and in chalcopyrite (0.4%). The majority (98%) of gold is predicted to be free gold with the remaining (2%) associated to trace concentrations in gold-bearing minerals such as sylvanite, or as invisible gold in chalcopyrite, pyrite, and magnetite.

Table 7: The economic resource at EH, including the gold compositions of chalcopyrite and pyrite. The calculations can be view in Appendix 3.

<i>Gold Mass Balance</i>	<i>Original Resource Size (Ryan 1998)</i>	<i>Foster et al. (2007)</i>	<i>This Study (2017)</i>
<i>Resource Size (Mt)</i>	167	-	-
<i>Resource Gold Grade (ppm)</i>	0.55	-	0.54
<i>Resource Copper Grade (%)</i>	1.12	-	-
<i>Au in Chalcopyrite (ppm)</i>	-	0.06	0.07
<i>Au in Pyrite (ppm)</i>	-	0.12	0.18
<i>Au in Magnetite (ppm)</i>	-	-	0.00
<i>Estimated Pyrite in Core Log (%)</i>	-	4	5
<i>Total Invisible Gold in Chalcopyrite (%)</i>	-	0.34	0.41
<i>Total Invisible Gold in Pyrite (%)</i>	-	0.87	1.60

Summary of Results

- A total of 155 free gold grains were identified from 20 of the 22 samples.
- Individual free gold grains averaged 13 μm in length and 4 μm in diameter, with 2 to 5 μm diameter representing the majority (86%) of grains.
- A majority (74%) of free gold grains were in contact with pyrite, and of these contacts most gold (72%) was located in Vein-infill Pyrite and commonly hosted in microfractures with chalcopyrite infill (65%).
- All pyrite textures have a common As-Co-Ni zonation, with Co concentrated in the core, Ni enriched at the rim and As more enriched either at the rim or core.
- Free gold in pyrite appears to be associated with a high As concentration gradient proximal to the rim, where the abundance of As exhibits a relatively large variation over a short distance.
- Mass balance calculations indicate that the majority (98%) of gold is in the form of free gold.

DISCUSSION

From observations of pyrite texture, free gold distribution and the mineralogical associations, and pyrite trace element chemistry, it is possible to make some inferences as to the mechanisms and conditions of free gold precipitation, and therefore, a better understanding of the hydrothermal fluids that formed EH.

Pyrite Textures

Sample collection targeted pyrite with textures as defined by A. Foster et al. (2007). These textures provide an opportunity to understand the relative timing of mineralisation (Figure 4), and how this has influenced free gold precipitation.

The primary and most abundant pyrite texture was *Disseminated Pyrite*. This ‘relatively early’ generation pyrite in the *fv2* ore zone is associated with minor free gold that is typically located at contact boundaries between pyrite and chalcopyrite (Figure 13a), and supports the findings of A. Foster et al. (2007). Disseminated Pyrite is interpreted to pre-date the main mineralisation stage because of the absence of chalcopyrite (Figure 10a). The associated free gold could be explained by a unrecorded hydrothermal event that precipitated free gold on the grain boundaries of Disseminated Pyrite prior to the main mineralisation stage, or, that free gold precipitated at the pre-existing grain boundaries of Disseminated Pyrite during the main mineralising Cu-Au hydrothermal fluid influx.

Vein-infill Pyrite is interpreted as a relatively ‘later’ generation pyrite as it overprints Disseminated Pyrite (Figure 9), and this interpretation is consistent with the findings of A. Foster et al. (2007). The association of Vein-infill Pyrite, chalcopyrite, and most free gold (Figure 13a), indicates that the gold entered into the system with the main economic (chalcopyrite) mineralisation stage.

Porphyroblastic Pyrite appears to overprint Disseminated Pyrite and the red rock alteration assemblage (Figure 5b; Figure 9), indicating that this is also a relatively 'later' generation pyrite, which concurs with the work of A. Foster et al. (2007). The minor free gold associated with Porphyroblastic Pyrite could be explained by free gold preferentially precipitating onto Vein-infill Pyrite.

Gold Chemistry

Majority of the observed gold is in the form of free gold (~98%), and the remainder as invisible gold, and other (rare) gold-bearing minerals such as sylvanite. This concurs with the studies of Brodie (2001) and A. Foster et al. (2007), who also observed that the composition of free gold varies from electrum (~65 wt.% Au; Figure 21a) to native gold (~95 wt.% Au; Figure 21a), with individual grains compositionally zoned. Changes in fluid pH, fO_2 , aS_2 , Au-Ag ratio, and temperature during gold precipitation may be responsible for these changes in the free gold composition (A. Foster et al., 2007).

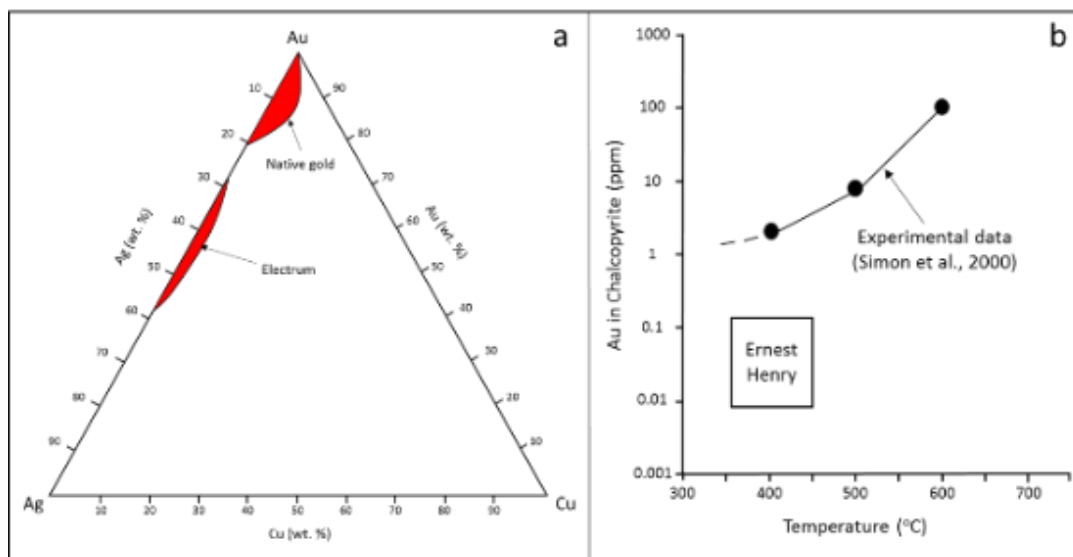


Figure 21: a) Ternary diagram of the Au-Ag-Cu system showing the regions for the most common compositions of electrum and native gold. Adapted from (Allan & Woodcock, 2001). b) Experimental data of Simon, Kesler, and Essene (2000) representing the expected Au content of chalcopyrite at different temperatures, compared with the actual Au content of chalcopyrite at EH. Adapted from Foster et al. (2007).

‘Invisible gold’ is the term given to gold present as sub-microscopic inclusions ($<1 \mu\text{m}$), or, as chemically bound (solid solution) gold in sulphides, particularly arsenian pyrite and arsenopyrite (Simon et al., 2000). Invisible gold in chalcopyrite and pyrite averaged 0.07 ppm and 0.18 ppm, with chalcopyrite ranging up to 0.23 ppm, and pyrite ranging up to 0.74 ppm, which concurs with the previous studies of Brodie (2001) and A. Foster et al. (2007).

Invisible gold in chalcopyrite and pyrite is an order of magnitude less than the saturation level from experimental data of Simon et al. (2000). The mineralisation temperature of EH has been modelled to be between 350°C and 450°C (Mark, Oliver, Williams, Valenta, & Crookes, 2000; Twyerould, 1997), and while the experimental data from Simon et al. (2000) indicates that at these temperatures, an upper value of ~5 ppm Au can substitute into chalcopyrite (Figure 21b), the average concentration of Au in chalcopyrite was 0.07 ppm. This indicates that either the chalcopyrite is undersaturated in Au and other mechanisms must have influenced the precipitation of free gold, or, the laboratory studies of Simon et al. (2000) do not accurately represent natural systems. A comprehensive study from George, Cook, Crowe, and Ciobanu (2017) investigated the trace element concentrations of chalcopyrite in natural systems and found that in hydrothermal deposits, chalcopyrite never hosted >0.24 ppm Au. This contributes to the growing evidence that chalcopyrite is a very poor gold host, and perhaps this contributes to why gold is mostly observed as free gold. Therefore, if pyrite, a typically good host for gold had already precipitated before the Cu-Au mineralisation, and since Au cannot partition to chalcopyrite in any significant concentrations, Au precipitated as free gold.

The amount of Au that can be dissolved in the structure of arsenian pyrite between 150°C and 250°C can be calculated from the following equation (1) by Reich et al. (2005).

$$C_{\text{Au}} = 0.02 \times C_{\text{As}} + 4 \times 10^{-5} \quad (1)$$

The average concentration of As in pyrite is ~2000 ppm, and from Equation 1 of Reich et al. (2005), the maximum amount of solid solution gold that can be in pyrite is ~40 ppm. This value is significantly higher than the average concentration of 0.18 ppm Au in pyrite, and indicates that either the fluid is undersaturated in Au, or, that the laboratory conditions of Reich et al. (2005) poorly represent natural environments at the higher temperatures of EH

Free gold grains are commonly present on pre-existing pyrite surfaces associated with chalcopyrite (Figure 13a). The lack of invisible gold in sulphides, and the abundance of free gold on pre-existing pyrite surfaces, indicates that Au has been selectively extracted onto pyrite surfaces during the main stage chalcopyrite precipitation.

As-Co-Ni Pyrite Chemistry

Pyrite commonly acts as a chemical ‘sponge’ in the sense that it readily adsorbs trace elements into its crystal lattice. Co and Ni commonly and more freely substitute for Fe in sulphur-poor, iron-rich fluids, creating n-type pyrite (Möller & Kersten, 1994). This substitution takes place at relatively high temperatures compared to the substitution of As for S, which creates p-type pyrite (Craig, Vaughan, & Higgins, 1979). Experimental studies from Craig et al. (1979) show that at 400°C, ~12 mol% CoS₂ and ~10 mol% NiS₂ are soluble in pyrite. At 700°C, solid solution between CoS₂ and pyrite is complete, however, there is a large miscibility gap between FeS₂ and NiS₂ at this temperature because of a bond length difference between Ni-S and Fe-S (Craig et al., 1979). We propose that from the trace

element data (Table 5; Table 6), and the experimental data of Craig et al. (1979), the composition of the hydrothermal fluids evolved as a result of co-precipitating mineral phases (similar to fractional crystallisation of melts), and that the pre-mineralisation hydrothermal fluid source which was saturated in As, evolved from a relatively high temperature (>500°C) to a relatively cooler temperature (350 to 450°C). The high Ni and low As content in pyrite samples from the iv lithology (Table 5) concurs with the interpretation that the fluids interacting with the ore body peripherals were cooler (allowing Ni to substitute with Fe) than the Cu-Au enriched fv2 lithology, and that is why Ni is more enriched in pyrite grains at the periphery of the ore system (Table 5). Additionally, the low As recorded in the peripherals of the iv lithology and the high As content in the fv1 and fv2 lithology supports the interpretation that the fluid was saturated in As.

A majority of the free gold was located in the rim-microfractures of Vein-infill Pyrite, which were not necessarily the locations most concentrated in As, but locations that represented sharp As concentration gradients (Figure 17; Figure 19). A. Foster et al. (2007) also found that free gold in pyrite was not always linked to locations highest As concentrations. Additionally, the microfractures indicate that the precipitation of free gold is partly controlled by physical conditions. Therefore, for pyrite to be a suitable host for free gold, it is necessary to have a fracture network for the gold-bearing solution to be able to permeate through the pyrite, and a sharp As concentration gradient for the gold to precipitate out of solution.

Electrochemical Reduction of Gold onto Pyrite

The proposed mechanism for free gold precipitation is the electrochemical reduction of Au^+ or Au^{3+} onto pre-existing pyrite surfaces (Figure 22). Depending on the chemical composition, pyrite can reflect either n- or p-type conductivity, with free gold deposited

predominantly on p-type surfaces (Möller & Kersten, 1994). Experimental studies (Hyland & Bancroft, 1989; Mironov, Zhmodik, & Maksimova, 1981; Möller & Kersten, 1994) and textural associations in natural systems (Möller & Kersten, 1994; Starling, Gilligan, Carter, Foster, & Saunders, 1989) propose that the semiconducting properties of pyrite surfaces are dependent on the ratio between sulphur and iron (Equation 2; Equation 3). Table 4 and Table 5 display that all pyrite classified by lithology and texture have an S/Fe ratio of ~0.12, indicating that pyrite is dominated by p-type conductivity.

$$\text{Equation 2: } S/Fe \text{ ratio } >2 = \text{n-type pyrite} \quad (2)$$

$$\text{Equation 3: } S/Fe \text{ ratio } <2 = \text{p-type pyrite} \quad (3)$$

The semiconducting properties of pyrite is demonstrated in the ability of As to extract Au from hydrothermal fluids through adsorption (Arehart, Chryssoulis, & Kesler, 1993; Fleet, Chryssoulis, Maclean, Davidson, & Weisener, 1993). In the examples of Arehart et al. (1993), and Fleet et al. (1993), pyrite acted as a catalyst at which free gold preferentially nucleated through physisorption (no bond formation between Au and FeS) or chemisorption (bond formed between Au and FeS).

Adsorption of free gold onto pyrite is facilitated by defects in the crystal lattice, which expose under-saturated S⁻ atoms to the gold-bearing solution (Figure 23) (Starling et al., 1989). Crystal defects may be more common along fractured pyrite surfaces, thus accounting for the high proportion of gold observed at these sites (Figure 13a). Starling et al. (1989) observed that free gold is most commonly located at defect locations in iron-bearing sulphides, particularly pyrite, in the study of lode-type gold deposits.

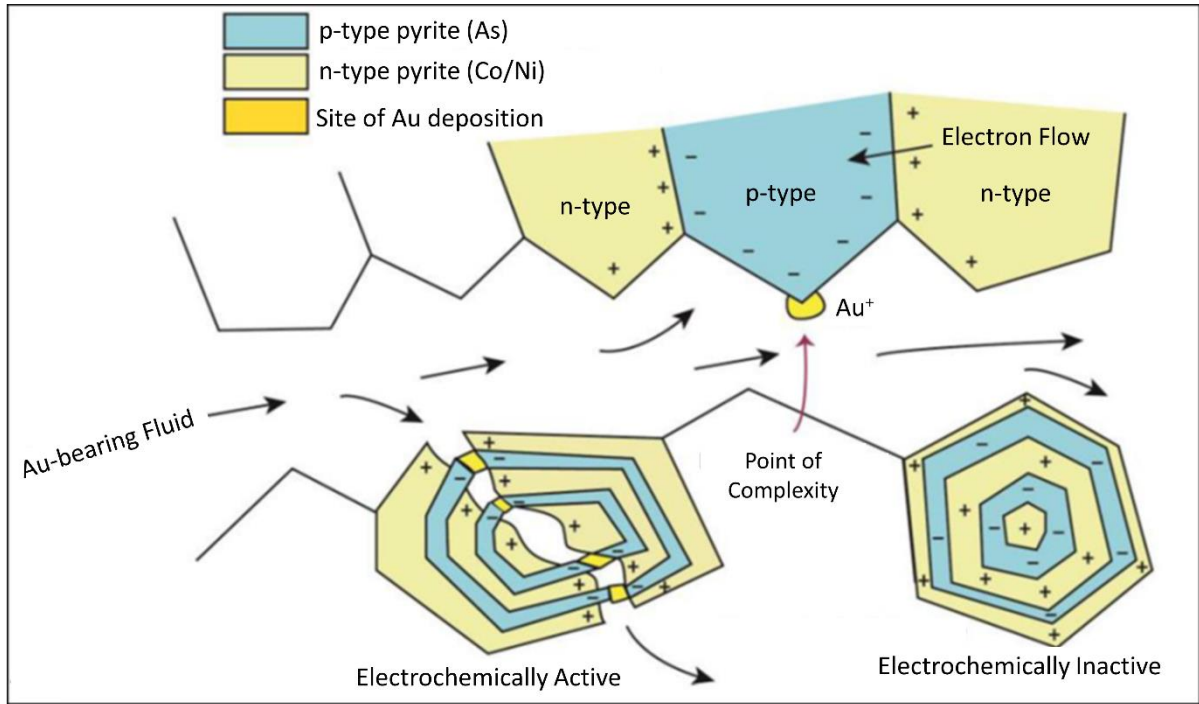


Figure 22: Electrochemical precipitation of free gold onto pre-existing pyrite surfaces with p-type (As-rich) conductivity. These n-p junctions create cell potential (>20 mV) that upon fracturing of the crystal become electrochemically active, promoting precipitation of Au^+ or Au^{3+} . Note the importance of the fracture network within grains to assist free gold precipitation. Adapted from Möller and Kersten (1994).

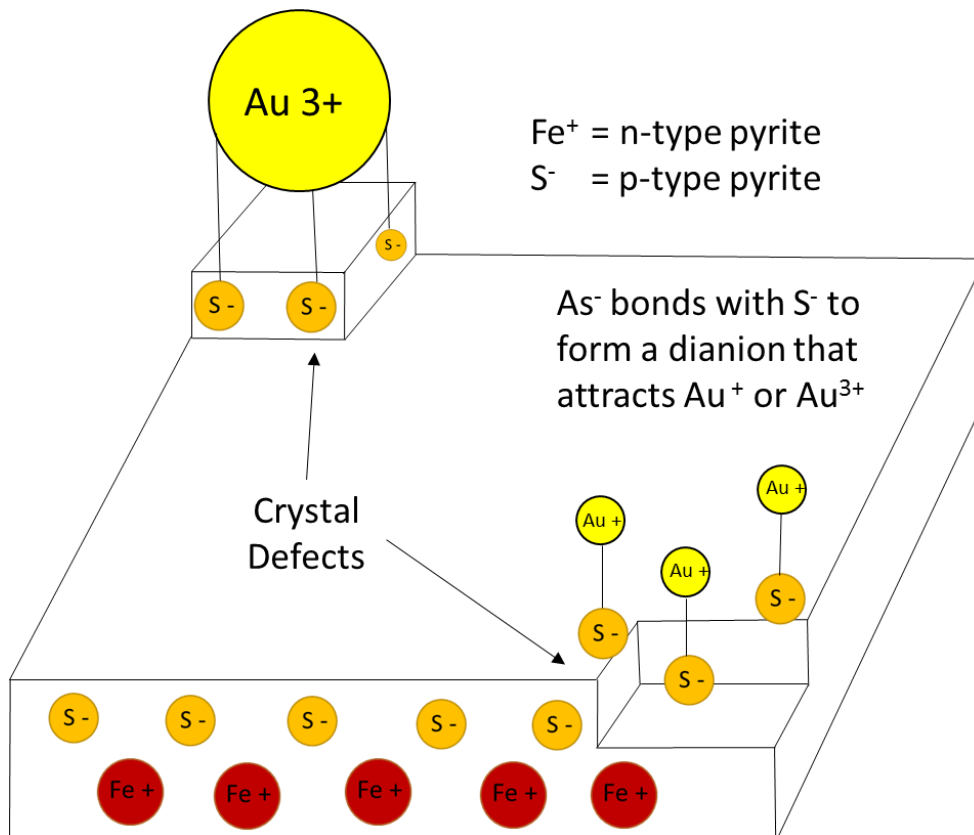


Figure 23: 3D illustration of the crystal defects that free S^- which attract Au^+ or Au^{3+} . Note that these crystal defects are caused by fractures as displayed in the pyrite grain from Figure 22.

Fluid Chemistry

The solubility of gold in pure water, even at moderately high temperatures (350 to 450°C) is negligible, so the formation of complexes (e.g. chlorides), is required to transport solutions for hydrothermal ore formation (Williams-Jones & Heinrich, 2005). The Naraku and Williams batholith has been proposed as the felsic source of the saline fluid required to produce the large quantities of pyrite present (P. Williams et al., 2005). The mineralising fluids may have transported gold as chloride complexes (AuCl_2^-) (Gammons & Williams-Jones, 1997), or, as hydrosulphide complexes ($\text{Au}[\text{HS}][\text{H}_2\text{S}]_3$) (Loucks & Mavrogenes, 1999).

Chloride and hydrosulphide complexes have separate mechanisms in which they precipitate gold in hydrothermal systems (Williams-Jones & Heinrich, 2005), and are largely controlled by temperature (Zhu, An, & Tan, 2011). Hydrosulphide complexes are the dominant phase at lower temperatures (<350°C), and precipitation of Au^+ or Au^{3+} as invisible gold (solid solution) takes place in response to sulphide precipitation (Cooke & Simmons, 2000; Robb, 2005). Chloride complexes are the dominant phase at higher temperature (>400°C), with decreasing temperature being the primary cause for gold precipitation (Gammons & Williams-Jones, 1997). Mark et al. (1999) analysed fluid inclusions of the economic mineralisation stage and detected chloride concentrations >10 molar, indicating that chloride complexes are the dominant source. The common occurrence of free gold on pre-existing pyrite, and the lack of invisible gold in solid solution of chalcopyrite and pyrite, is consistent with chloride complexes being the dominant source of transporting gold.

Natural pyrites contain small quantities of trace elements in addition to Fe and S. Pyrite trace elements can be divided into three groups according to the most likely occurrence of the element: (1) elements that occur mainly as inclusions (including Cu, Zn, Pb, Ba, Bi, Ag, and Sb), (2) elements that occur as nonstoichiometric substitutions in the sulphur lattice

(including As, Tl, Au, Se, Te and possibly Mo), and (3) elements that occur as stoichiometric substitutions for Fe such as; Co, Ni, and less commonly, Cu (Huston et al., 1995).

Pyrite commonly exhibits As-Co-Ni zonation with an As-rich core or rim, Co-rich core, and a Ni-rich rim (Figure 16a; Figure 17), and has concentrations of up to 2 wt.% As, 2 wt.% Co, and 1 wt.% Ni (Rusk et al., 2010). The high standard deviation of As, Co, and Ni (Table 6), in particular for Disseminated Pyrite, reflects the variation in these trace elements, and this is further supported by observations of complex As-Co-Ni zonation with irregular gradients, which can be symmetrical or asymmetrical (Figure 16a; Figure 17). These characteristics indicate that physiochemical interactions of the changing fluid composition have influenced the distribution of trace elements in pyrite.

Ion probe analyses on sulphur isotopes targeting high and low As-Co-Ni concentrations in pyrite grains prove that there is no significant isotopic trend from core to rim, and there is no obvious correlation between $\delta^{34}\text{S}$ and minor element concentration among the various growth zones (Mark, Williams, Ryan, vanAchterbergh, & Prince, 2004b). In all zones $\delta^{34}\text{S}$ ranges between ~2 and 4‰, consistent with most of bulk sulphur isotope analyses (Mark, Oliver, & Williams, 2006b; Mark, Williams, Oliver, Ryan, & Mernagh, 2005a). This lack of association between the sulphur isotope ratio values and trace element concentration, indicates that even though conditions of sulphide precipitation vary enough to cause large and abrupt shifts in minor element composition, the source of fluid remained relatively constant during pyrite precipitation.

Regional Deposits: A Result of Fluid Mixing

Mixing of two or more hydrothermal fluids is important in the formation of many IOCG deposits, and may have been an efficient means of changing the physiochemical conditions of the hydrothermal fluids resulting in ore deposition. Mineralisation is proposed to have been

sourced by the mixing of oxidised magmatic fluids released by the Williams and Naraku batholiths, and reduced basinal brines (P. Williams et al., 2005). The average Co to Ni ratio in pyrite is ~200 (Figure 24), which plots in the volcanogenic and magmatic range (Bralia, Sabatini, & Troja, 1979; Loftus-Hills & Solomon, 1967; Price, 1972). The Co-Ni zonation reflects that the physiochemical conditions changed during the growth of pyrite. We propose that the hot magmatic fluid sourced from the Williams and Naraku batholith has been cooled by a basinal fluid, which has facilitated the precipitation of pyrite, and this is why Ni is observed in the rim of pyrite (Figure 16a; Figure 17; Table 6). Rusk et al. (2010) concluded that pyrite in copper-mineralised and non-mineralised prospects in the Cloncurry district also exhibit As-Co-Ni zonation, and proposed that the hydrothermal fluid source of EH is spatially related to other district IOCG occurrences.

There is a positive correlation between Au concentration, and the concentration of trace elements, including Ag, As, Co, Cu, Fe, Mo, Ni, and U at the 1 m composite assay scale (Figure 2). Mark et al. (1999) proposes that the different solubilities of the listed metals was facilitated by the mixing of a magmatic and basinal fluid, which can be accounted for by their positive correlation with gold at the assay scale. At the micro-scale (ICP-MS data), no Au-As correlation exists (Figure 18), which supports the minor observed and calculated invisible gold (Table 7; Appendix 4). The minor invisible gold further supports the transportation of Au^+ or Au^{3+} by chloride complexes (Gammons & Williams-Jones, 1997). At the assay-scale, the Au-As correlation ($R^2 = 0.28$) is consistent with observation that As is associated with gold deposits (Cook, Ciobanu, Meria, Silcock, & Wade, 2013; Zhu et al., 2011), and which As is commonly used as a pathfinder element during exploration (R. Lilly personal communication, August, 2017).

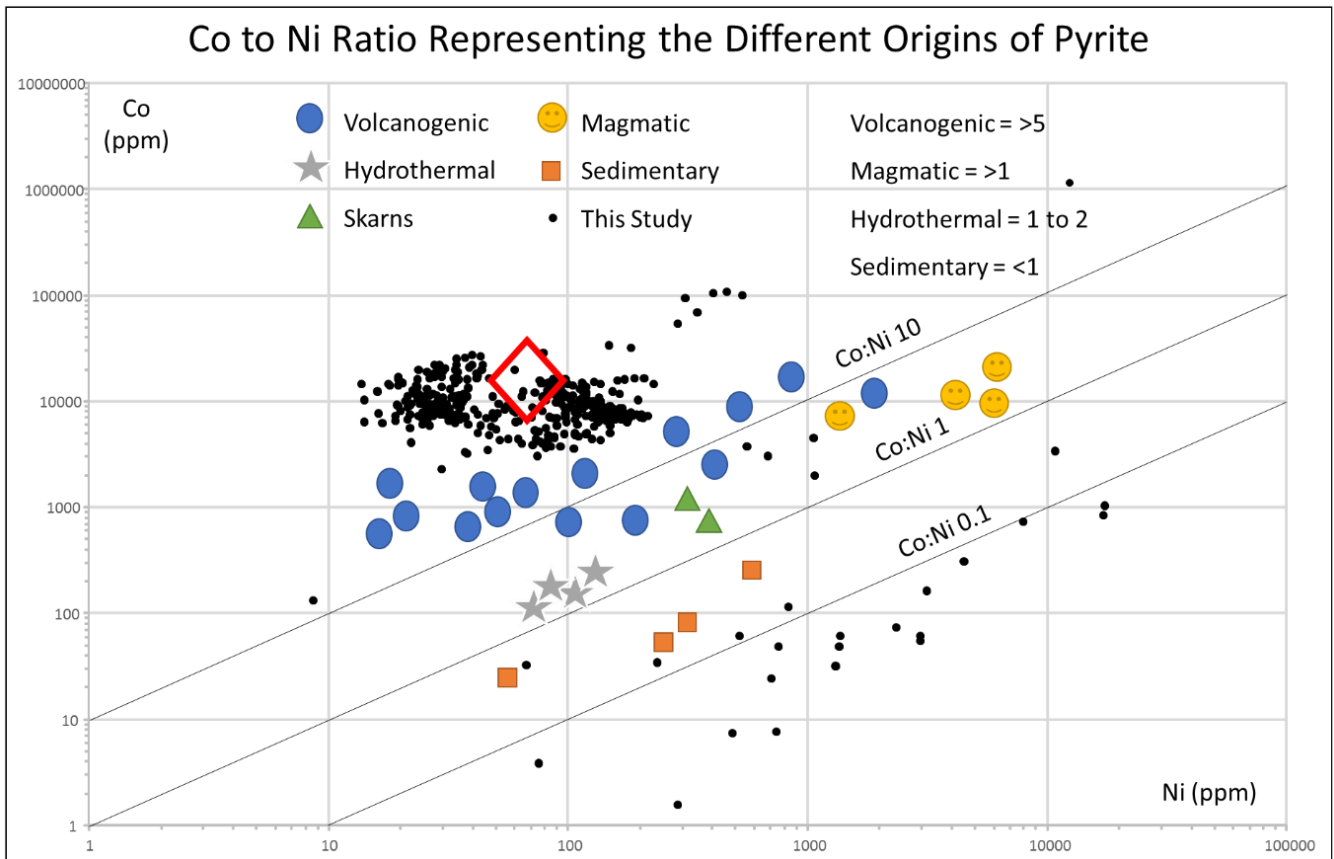


Figure 24: Bivariate scatter plot representing the Co to Ni ratios for pyrite of different origins. The red diamond is the median value for this study. Note the average pyrite Co and Ni ratio plots in the region of a magmatic and volcanogenic source.

Mining Challenges

The challenge of improving gold recovery lies with extracting gold from gangue minerals such as pyrite prior to being separated to the tailings. Recovering gold from the tailings is currently not economic and would require reprocessing of large amounts of material and the use of expensive reagents.

Pyrite contains significant quantities of ‘penalty’ elements such as As and S, and it is desirable to remove such environmental contaminants prior to smelting. Occasionally, pyrite may carry significant concentrations of valuable metals as impurities including gold. In addition, the presence of pyrite in chalcopyrite (copper) concentrates effectively dilutes the value of the material. Setting aside gold-bearing pyrite, or selling to a sub-contractor for

reprocessing could be an alternative to minimise the challenges of diluting the copper concentrate.

If no free gold is liberated from pyrite during the milling process, and only the free gold associated to chalcopyrite is processed, then the estimated gold recovery is 7%, which is significantly lower than reported 65% recovery from EH Mining (2000). This indicates that the current milling process is successful at liberating ~58% of gold from gangue minerals. Because a large proportion of gold grains $\leq 5\mu\text{m}$ associated to pyrite, gravity concentration, with or without reduction in the grind size, may increase the recovery of gold. Such a process is used at the Osborne IOCG deposit (Figure 1), where a large proportion of the free gold is associated to pyrite, and has a gold recovery of ~80%.

Extrapolating the data from this study into the entire EH ore body must be done with caution, as the data is sourced from 22 polished thin sections of typically fv1, and fv2 lithology, totalling $\sim 150\text{ cm}^2$ of ore from three drill-holes. However, confidence in the findings of this study can be made from the previous research of Brodie (2001) and A. Foster et al. (2007) at the upper levels of the ore body.

CONCLUSIONS

This project has established that ~98% of the gold at EH is in the form of free gold with observed grains having an average diameter of 4 μm . Pyrite hosted the majority of the free gold, and microfractures in the Vein-infill Pyrite texture was the most common precipitation site.

Gold entered the system with the main mineralisation stage of chalcopyrite and was adsorbed onto pre-existing pyrite surfaces. We propose that the electrochemical reduction of Au^+ or Au^{3+} facilitated the precipitation free gold from chloride complexes, and that the fluid may have been undersaturated in gold, or, the laboratory experiments may not be an accurate representation for the lack of invisible gold in chalcopyrite and pyrite. The high proportion of free gold located in pyrite microfractures can be explained by the semi-conducting potential that is released from surface defects, such as microfractures, which free S^- atoms that are required to adsorb Au^+ or Au^{3+} .

FURTHER RESEARCH

This study found that 74% of the free gold is associated with pre-existing pyrite surfaces. Further research could focus on how successful the milling process liberates gold from these pyrite surfaces by investigating concentrate samples. Additionally, because gold is malleable and pyrite is brittle, investigating pyrite textures in the tailings and different final grind sizes would resolve how successful the milling process is at liberating gold from gangue minerals.

ACKNOWLEDGMENTS

Thank you to Brad Miller, Dan Ashton, Jack Gurney, Vanessa Sexton, and the rest of the team at Ernest Henry for assisting the field work and financially supporting this project. Across the road I need to thank Dave Kelsey and Sarah Gilbert from Adelaide Microscopy for their warm welcoming and expert advice throughout the year. To the Honours cohort and Alec Walsh, working with you all on our projects has been a fun and lively year. And the last person I would like send a huge thank you too is Richard Lilly, my supervisor. Your organisation, commitment, and keenness has made this year the highlight of my university experience. My personal development is a direct reflection of the time and effort you have put into helping me. Cheers!

REFERENCES

- ALLAN, G., & WOODCOCK, J. (2001). A Review of the Flotation of Native Gold and Electrum. *Minerals Engineering*, 14(9), 931-962.
- AREHART, G., CHRYSOULIS, S., & KESLER, S. (1993). Gold and Arsenic in Iron Sulphides from Sediment-hosted Disseminated Gold Deposits: Implications for Depositional Processes. *Economic Geology*, 88, 171-185.
- AUSTIN, J., & BLENKINSOP, T. (2009). Local to Regional Scale Structural Controls on Mineralisation and the Importance of a Major Lineament in the Eastern Mount Isa Inlier Australia: Review and Analysis with Autocorrelation and Weights of Evidence. *Ore Geology Reviews*, 35, 298-316.
- BAKER, T., MUSTAD, R., WILLIAMS, P., DONG, G., FISHER, L., MARK, G., & RYAN, C. (2008). Mixed Messages in Iron Oxide Copper-Gold Systems of the Cloncurry District, Australia: Insights from PIXE Analysis of Halogens and Copper in Fluid Inclusions. *Mineralium Deposita*, 43, 599-608.
- BLAKE, D. (1987). *Geology of the Mount Isa Inlier and Environs, Queensland and Northern Territory*.
- BLAKE, D., & STEWART, A. (1992). Stratigraphic and Tectonic Framework, Mount Isa Inlier. *Australian Geological Survey Organisation*, 1-12.
- BRALIA, A., SABATINI, G., & TROJA, F. (1979). A Reevaluation of the Co/Ni Ratio in Pyrite as a Geochemical Tool in Ore Genesis Problems. Evidence from Southern Tuscany Pyritic Deposits. *Mineralium Deposita*, 14, 353-374.
- BRODIE, A. (2001). *Gold Distribution in Hypogene Ore at the Ernest Henry Cu-Au Mine, NW Queensland; Implications for Minerals Processing and Ore Deposition*. University of Tasmania, Unpublished.
- CAVE, B. (2017). *U-Pb Geochronology and Trace Element Analysis of Apatite and Calcite from the Ernest Henry Deposit, NW Queensland*. (Bachelor of Science (Honours)), University of Adelaide.
- CIOBANU, C., COOK, N., UTSUNOMIYA, S., KOGAGWA, M., GREEN, L., GILBERT, S., & WADE, B. (2012). Gold-telluride Nanoparticles Revealed in Arsenic-free Pyrite. *American Mineralogist*, 97, 1515-1518.
- COOK, N., & CHRYSOULIS, S. (1990). Concentration of "Invisible Gold" in the Common Sulphides. *Canadian Mineralogist*, 28, 1-16.
- COOK, N., CIOBANU, C., MERIA, D., SILCOCK, D., & WADE, B. (2013). Arsenopyrite-Pyrite Association in an Orogenic Gold Ore: Tracing Mineralization History from Textures and Trace Elements. *Economic Geology*, 108(6), 1273-1283. doi: 10.2113/econgeo.108.6.1273
- COOKE, D., & SIMMONS, S. (2000). Characteristics and Genesis of Epithermal Gold Deposits. *Economic Geology*, 13, 221-244.
- CRAIG, J., VAUGHAN, D., & HIGGINS, J. (1979). Phase Relations in the Cu-Co-S System and Mineral Associations of the Carrollite (CuCo₂S₄)-Linnaeite (Co₃S₄) Series. *Society of Economic Geologists*, 74(3). doi: 10.2113/gsecongeo.74.3.657
- DENARO, T., RAMSDEN, C., & BROWN, D. (2007). Queensland Minerals: A Summary of Major Mineral Resources, Mines and Projects.: Queensland Department of Mines and Energy.
- ETHERIDGE, M., RUTLAND, R., & WYBORN, L. (1987). Orogenesis and Tectonic Processes in the Early to Middle Proterozoic of North Australia. *American Geophysical Union*, 131-147.
- FLEET, M., CHRYSOULIS, S., MACLEAN, P., DAVIDSON, R., & WEISNER, C. (1993). Arsenian Pyrite from Gold Deposits; Au and As Distribution Investigated by SIMS and EMP and Colour Staining and Surface Oxidation by XPS and LIMS. *Canadian Mineralogist*, 31, 1-17.
- FOSTER, A., WILLIAMS, P., & RYAN, C. (2007). Distribution of Gold in Hypogene Ore at the Ernest Henry Iron Oxide Copper-Gold Deposit, Cloncurry District, NW Queensland. *Exploration and Mining Geology*, 16, 3-4, 125-143.
- FOSTER, D. (2003). *Proterozoic Low-pressure Metamorphism in the Mount Isa Inlier, Northwest Queensland, Australia, with Particular Emphasis on the use of Calcic Amphibole Chemistry as Temperature-pressure Indicators*. James Cook University, Unpublished PhD.
- FOSTER, D., & AUSTIN, J. (2008). The 1800-1610 Ma Stratigraphic and Magmatic History of the Eastern Succession, Mount Isa Inlier, and Correlations with Adjacent Paleoproterozoic Terranes. *Precambrian Research*, 163, 7-30. doi: 10.1016/j.precamres.2007.08.010
- FOSTER, D., & RUBENACH, M. (2006). Isograd Pattern and Regional Low-pressure, High-temperature Metamorphism of Pelitic, Mafic and Calc-silicate Rocks along an East-west Section through the Mt Isa Inlier. *Australian Journal of Earth Sciences*, 53, 167-186.
- FUSS, M. (2014). *Isotopic (⁸⁷Sr/⁸⁶Sr, $\delta^{13}C$ and $\delta^{18}O$) Indicators of Fluid Source from Carbonates in the Ernest Henry Deposit, Queensland, Australia: Implications for Genesis and Exploration*. (Bachelor of Geology (Honours)), James Cook University.
- GAMMONS, C., & WILLIAMS-JONES, A. (1997). Chemical Mobility of Gold in the Porphyry-epithermal Environment. *Economic Geology*, 92(45-59).

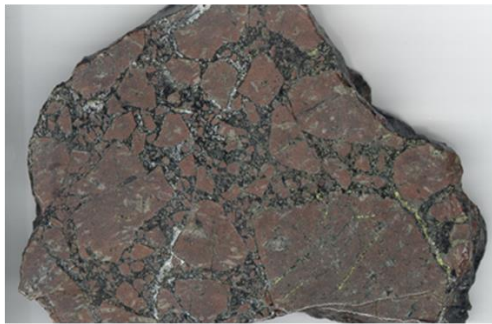
- GEORGE, L., COOK, N., CROWE, B., & CIOBANU, C. (2017). Trace Elements in Hydrothermal Chalcopyrite. *Mineralogical Magazine*.
- HYLAND, M., & BANCROFT, G. (1989). An XPS Study of Gold Deposition at Low Temperatures on Sulphide Minerals: Reducing Agents. *Geochimica et Cosmochimica Acta*, 53, 367-372.
- KENDRICK, M., MARK, G., & PHILLIPS, D. (2007). Mid-crustal Fluid Mixing in a Proterozoic Fe Oxide-Cu-Au Deposit, Ernest Henry, Australia: Evidence from Ar, Kr, Xe, Cl, Br, and I. *Earth Planetary Science*, 256, 328-343.
- LILLY, R., CASE, R., & MILLER, B. (2017). Ernest Henry Iron Oxide Copper-Gold Deposit. *Australian Ore Deposits*.
- LOFTUS-HILLS, G., & SOLOMON, M. (1967). Cobalt, Nickel, and Selenium in Sulphides as Indicators of Ore Genesis. *Mineralium Deposita*, 2(3), 228-242.
- LOUCKS, R., & MAVROGENES, J. (1999). Gold Solubility in Supercritical Hydrothermal Brines Measure in Synthetic Fluid Inclusions. *Science*, 284, 2159-2163.
- MARK, G., FOSTER, D., OLIVER, N., RICHMOND, J., POLLARD, P., & TOLMAN, J. (2001). The Role of Magmatism in Regional Sodic-Calcic Alteration in the Cloncurry District, Northern Australia. *Geological society of Australia* 44-63.
- MARK, G., OLIVER, N., & WILLIAMS, P. (2006). Mineralogical and Chemical Evolution of the Ernest Henry Fe Oxide Cu-Au Ore System, Cloncurry District, North-West Queensland, Australia. *Mineralium Deposita*, 40, 769-801.
- MARK, G., OLIVER, N., & WILLIAMS, P. (2006b). Mineralogical and Chemical Evolution of the Ernest Henry Fe Oxide Cu-Au Ore System, Cloncurry District, Northwest Queensland, Australia. *Mineralium Deposita*, 40, 769-801.
- MARK, G., OLIVER, N., WILLIAMS, P., VALENTA, R., & CROOKES, R. (1999). Characteristics and Origins of the Ernest Henry Iron Oxide Copper-Gold Hydrothermal System; Results of the 1999 Collaborative SPIRT Research Project, James Cook University, Townsville.
- MARK, G., OLIVER, N., WILLIAMS, P., VALENTA, R., & CROOKES, R. (2000). The Evolution of the Ernest Henry Hydrothermal System. *Adelaide, Porter GeoConsultancy Publishing*, 1, 123-136.
- MARK, G., WILLIAMS, P., OLIVER, N., RYAN, C., & MERNAGH, T. (2005a). Fluid Inclusion and Stable Isotope Geochemistry of the Ernest Henry Iron Oxide-Copper-Gold Deposit, Queensland, Australia. *Mineral deposit research: Meeting the global challenge: Berlin, Springer*, 785-788.
- MARK, G., WILLIAMS, P., RYAN, C., VANACHTERBERGH, E., & PRINCE, K. (2004b). A Couples Microanalytical Approach to Resolving the Origin of Fluids and the Genesis of Ore Formation in Hydrothermal Deposits. *Geological society of Australia*, 73, 97.
- MIRONOV, A., ZHMODIK, S., & MAKSIMOVA, E. (1981). An Experimental Investigation of the Sorption of Gold by Pyrites with Different Thermoelectric Properties. *Geochemistry International*, 18, 153-160.
- MÖLLER, P., & KERSTEN, G. (1994). Electrochemical Accumulation of Visible Gold on Pyrite and Arsenopyrite Surfaces. *Mineralium Deposita*, 29, 404-413.
- O'BRIEN, S. (2016). *Structural and Mineralogical Controls on the Formation of the 'Inter-lens' at the Ernest Henry Deposit, Queensland.*, University of Adelaide, Unpublished.
- OLIVER, N., BUTERA, K., RUBENACH, M., MARSHALL, L., CLEVERLEY, J., MARK, G., . . . ESSER, D. (2008). The Protracted Hydrothermal Evolution of the Mount Isa Eastern Succession: A Review and Tectonic Implications. *Precambrian Research*, 163, 108-130.
- OLIVER, N., RUBENACH, M., FU, B., BAKER, T., BLENKINSOP, T., CLEVERLEY, J., & RIDD, P. (2006). Granite-related Overpressure and Volatile Release in the Mid Crust: Fluidized Breccias from the Cloncurry District, Australia. *Geofluids*, 6(4), 346-358. doi: 10.1111/j.1468-8123.2006.00155.x
- PAGE, R., & SUN, S. (1998). Aspects of Geochronology and Crustal Evolution in the Eastern Fold Belt, Mount Isa Inlier. *Australian Journal of Earth Sciences*, 45, 219-232.
- POLLARD, P. (2006). An Intrusion-related Origin for Cu-Au Mineralisation in Iron Oxide Copper-Gold (IOCG) Provinces. *Mineralium Deposita*, 41, 179-187.
- PRICE, B. (1972). *Minor Elements in Pyrites from the Smithers Map Area, British Columbia, and Exploation Applications of Minor Element Studies.* (M.Sc.), British Columbia.
- REICH, M., KESLER, S., UTSUNOMIYA, S., PALENIK, C., CHRYSOULIS, S., & EWING, R. (2005). Solubility of Gold in Arsenian Pyrite. *Geochimica et Cosmochimica Acta*, 69, 2781-2796. doi: 10.1016/j.gca.2005.01.011
- ROBB, L. (2005). Introduction to Ore-forming Processes., 373.
- RUSK, B., OLIVER, N., CLEVERLEY, J., BLENKINSOP, T., ZHANG, D., WILLIAMS, P., & HABERMANN, P. (2010). Physical and Chemical Characteristics of the Ernest Henry Iron Oxide Copper-Gold Deposit, Australia; Implications for IOCG Genesis. *Hydrothermal Iron Oxide Copper-Gold and Related Deposits: A Global Perspective*, 3, 201-218.

- RYAN, A. (1998). Ernest Henry Copper-Gold Deposit. *Australasian Institute of Mining and Metallurgy, Monograph 22*, 759-767.
- SCHWARTZ, G. (1944). The Host Minerals of Native Gold. *Economic Geology*, 39, 371-411.
- SIMON, G., KESLER, S., & ESSENE, E. (2000). Gold in Porphyry Copper Deposits: Experimental Determination of the Distribution of Gold in the Cu-Fe-S System at 400o to 700oC. *Economic Geology*, 95, 259-270.
- STARLING, A., GILLIGAN, J., CARTER, A., FOSTER, R., & SAUNDERS, R. (1989). High-Temperature Precipitation of Precious Metals on the Surface of Pyrite. *Nature*, 340, 298-300.
- TWYEROULD, S. (1997). *The Geology and Genesis of the Ernest Henry Fe-Cu-Au Deposit, Northwest Queensland, Australia.*, University of Oregon, Eugene, Unpublished PhD thesis.
- WILLIAMS-JONES, A., & HEINRICH, C. (2005). Vapor Transport of Metals and the Formation of Magmatic-Hydrothermal Ore Deposits. *Economic Geology*, 100(7), 1287-1312. doi: 10.2113/gsecongeo.100.7.1287
- WILLIAMS, M., HOLWELL, D., LILLY, R., CASE, G., & McDONALD, I. (2015). Mineralogical and Fluid Characteristics of the Fluorite-rich Monakoff and E1 Cu-Au Deposits, Cloncurry Region, Queensland, Australia: Implications for Regional F-Ba-rich IOCG Mineralisation. *Ore Geology Reviews*, 64, 103-127. doi: 10.1016/j.oregeorev.2014.05.0210169-1368
- WILLIAMS, P., BARTON, M., JOHNSON, D., FRONTBOTE, L., DE HALLER, A., MARK, G., . . . MARSCHIK, R. (2005). Iron Oxide Copper-Gold Deposits: Geology, Space-Time Distribution, and Possible Modes of Origin. *Economic Geology*, 100, 371-405.
- ZHU, Y., AN, F., & TAN, J. (2011). Geochemistry of Hydrothermal Gold Deposits: A Review. *Geoscience Frontiers*, 2(3), 367-374.

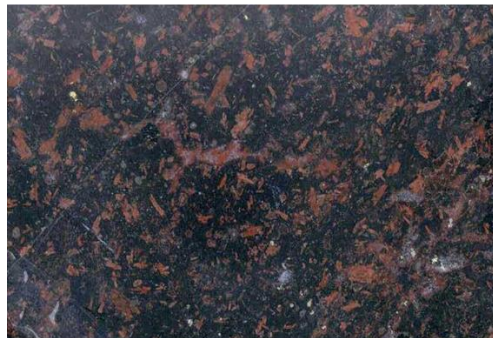
APPENDIX 1.A: EXTENDED LITHOLOGY DESCRIPTIONS



fv2 msbx – (**Matrix Supported Felsic Volcanic Breccia**) - The primary high grade ore zone is composed of fine grained hematite-altered matrix supported brecciated felsic volcanics. The matrix is predominantly composed of magnetite, carbonate, biotite with economic chalcopyrite and minor pyrite. Clasts contain some remnant fine grain dark rock (biotite & magnetite) and albite alteration.





















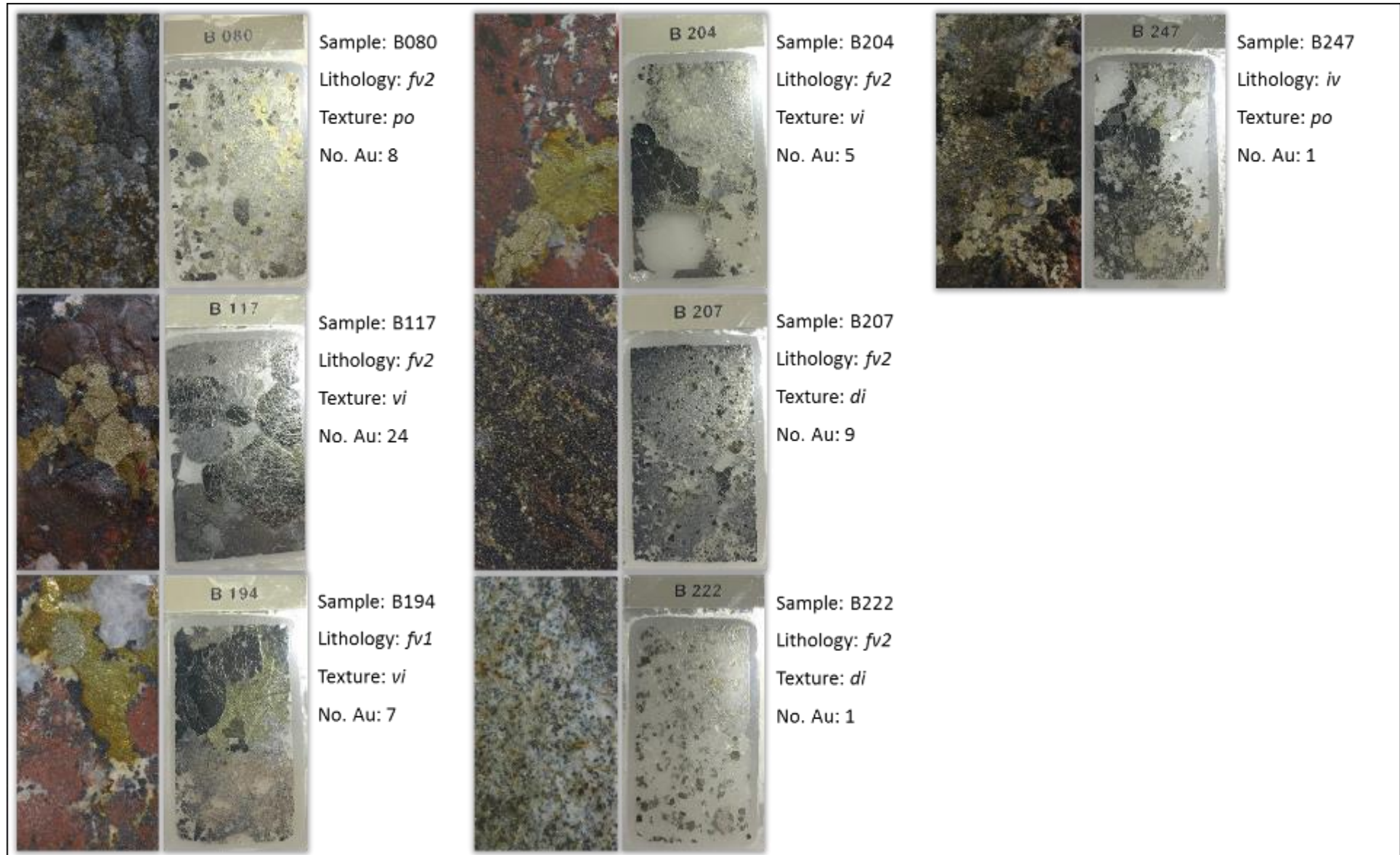
fv1 csbx – (**Clast Supported Felsic Volcanic Breccia**) - The high grade *fv2* (*msbx*) breccia grades into fine grained, hematite-k-feldspar-altered clast supported brecciated felsic volcanics. The matrix is composed of magnetite, carbonate, biotite with economic chalcopyrite and minor pyrite. Furthermore, *fv1* grades into a lower grade crackle breccia (*fv*).

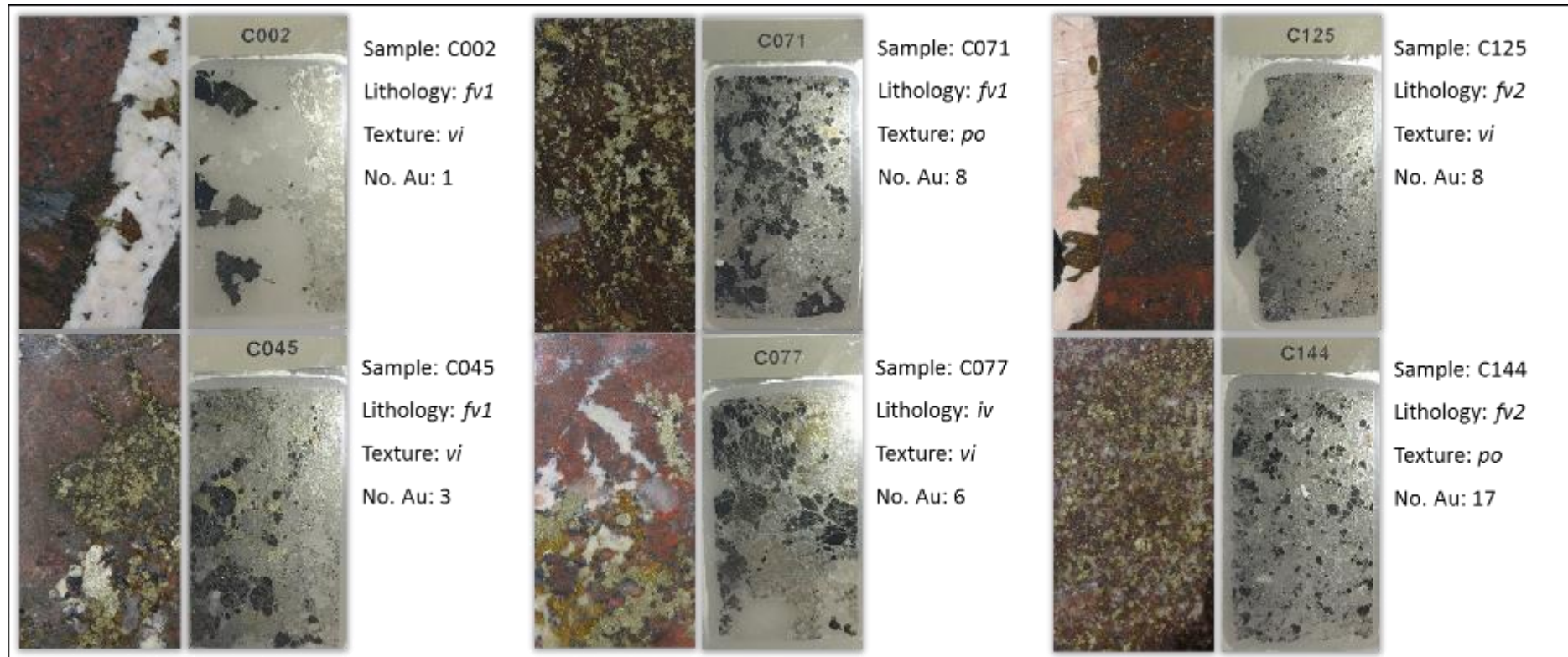


iv – (**Hanging wall-Type Meta-Volcanics**) – Intermediate volcanic rocks commonly seen on the southern side of the hanging wall shear zone. The unit is porphyritic with a dark-grey to black matrix. The phenocrysts are plagioclase, and the dark-grey black matrix is fine-grained magnetite + biotite (dark-rock alteration) replacing the fine grained plagioclase groundmass. Varieties of this rock type have been overprinted/re-placed by red-rock alteration (albite/k-feldspar), replacing primary plagioclase phenocrysts. Sometimes forms a “trachytic” texture, with the aligned plagioclase laths and biotite wrapping around larger plagioclase laths.

APPENDIX 1.B: SAMPLE SUMMARY

		<p>Sample: A034 Lithology: <i>fv2</i> Texture: <i>di</i> No. Au: 2</p>			<p>Sample: A121b Lithology: <i>fv2</i> Texture: <i>vi</i> No. Au: 10</p>			<p>Sample: A157 Lithology: <i>fv1</i> Texture: <i>vi</i> No. Au: 0</p>
		<p>Sample: A036 Lithology: <i>fv2</i> Texture: <i>vi</i> No. Au: 10</p>			<p>Sample: A127 Lithology: <i>fv2</i> Texture: <i>vi</i> No. Au: 15</p>			<p>Sample: A168 Lithology: <i>fv2</i> Texture: <i>vi</i> No. Au: 17</p>
		<p>Sample: A121a Lithology: <i>fv2</i> Texture: <i>vi</i> No. Au: 0</p>			<p>Sample: A155 Lithology: <i>fv1</i> Texture: <i>po</i> No. Au: 1</p>			<p>Sample: A177 Lithology: <i>fv2</i> Texture: <i>po</i> No. Au: 2</p>





APPENDIX 2.A: EXTENDED MINERALOGICAL AND TEXTURAL SETTING OF FREE GOLD

<i>Sample A</i>	<i>Image ID</i>	<i>Size (µm)</i>	<i>Mineralogical association</i>	<i>Textural Site</i>	<i>py Texture</i>	<i>Lithology</i>	<i>ID</i>
A034	1	8x2	ccp in py	mf	di	fv2	1
A034	2	5x2	ca/qz in py	mf	di	fv2	2
A036	3	30x10	ccp/py	cm	vi	fv2	3
A036	4	10x5	ba in py	mf	vi	fv2	4
A036	5	5x5	ca/fl in py	mf	vi	fv2	5
A036	5	2x2	ca/fl in py	mf	vi	fv2	6
A036	5	2x2	ca/fl in py	mf	vi	fv2	7
A036	8	20x3	fl in py	mf	vi	fv2	8
A036	9	18x2	ca/fl/mt in py	mf	vi	fv2	9
A036	9	10x2	ca/fl/mt in py	mf	vi	fv2	10
A036	9	8x3	ca/fl/mt in py	mf	vi	fv2	11
A036	9	2x2	ca/fl/mt in py	mf	vi	fv2	12
A121a	-	-	-	-	vi	fv2	13
A121b	14	8x4	ccp in py	mf	vi	fv2	14
A121b	15	50x4	ccp in py	mf	vi	fv2	15
A121b	16	8x4	ccp in py	mf	vi	fv2	16
A121b	17	8x2	py	mf	vi	fv2	17
A121b	18	15x10	ca+qz in py	dp	vi	fv2	18
A121b	19	5x3	ccp in py	mf	vi	fv2	19
A121b	19	2x2	ccp in py	mf	vi	fv2	20
A121b	21	20x4	ccp in py	mf	vi	fv2	21
A121b	22	5x3	ccp in py	mf	vi	fv2	22
A121b	23	40x2	py	mf	vi	fv2	23
A127	24a	20x4	ccp in py	mf	vi	fv2	24
A127	24b	10x4	ca/ccp	cm	vi	fv2	25
A127	24b	15x5	ca/ccp/py	cm	vi	fv2	26
A127	24b	20x8	ca/py	cm	vi	fv2	27
A127	28	15x5	ccp/fl/py	cm	vi	fv2	28
A127	N/A	15x4	ccp in py	mf	vi	fv2	29
A127	30	20x4	ccp in py	mf	vi	fv2	30
A127	31	5x2	ccp in py	mf	vi	fv2	31
A127	31	15x6	ccp in py	mf	vi	fv2	32
A127	33	5x5	ccp in py	mf	vi	fv2	33
A127	33	35x4	ccp in py	mf	vi	fv2	34
A127	35	5x2	py	dp	vi	fv2	35
A127	36	7x4	ccp in py	mf	vi	fv2	36
A127	37	5x2	ccp in py	mf	vi	fv2	37
A127	38	8x3	ccp in py	mf	vi	fv2	38
A155	39	5x4	ccp/py	cm	po	fv1	39
A157	-	-	-	-	vi	fv1	40

James Hewett
Ernest Henry Gold and Pyrite

A168	41	50x5	ccp in py	mf	vi	fv2	41
A168	42	15x2	ccp in py	mf	vi	fv2	42
A168	43	10x5	ccp in py	mf	vi	fv2	43
A168	44	20x5	py	dp	vi	fv2	44
A168	45	5x5	py	dp	vi	fv2	45
A168	46	4x2	py	mf	vi	fv2	46
A168	46	6x2	py	mf	vi	fv2	47
A168	46	10x2	py	mf	vi	fv2	48
A168	49a	4x4	kf/mt/py/ru	mf	vi	fv2	49
A168	49a	2x2	kf/mt/py/ru	mf	vi	fv2	50
A168	49a	20x5	kf/mt/py/ru	mf	vi	fv2	51
A168	49b	20x5	mt	mf	vi	fv2	52
A168	49b	10x5	mt	mf	vi	fv2	53
A168	49c	8x3	kf/mt/py/ru	cm	vi	fv2	54
A168	49c	12x4	kf/mt/py/ru	mf	vi	fv2	55
A168	49d	12x3	mt	mf	vi	fv2	56
A168	49d	8x2	mt	mf	vi	fv2	57
A177	58	10x4	ccp in py	mf	po	fv2	58
A177	59	8x3	ccp/py	mf	po	fv2	59

Sample B	Image ID	Size (µm)	Mineralogical association	Textural Site	py Texture	Lithology	ID
B080	60	8x6	mt	dp	po	fv2	60
B080	61	8x8	ccp	cm	po	fv2	61
B080	62	3x2	ccp	dp	po	fv2	62
B080	63	8x6	ccp	dp	po	fv2	63
B080	64	30x20	ccp	dp	po	fv2	64
B080	64	8x5	ccp	dp	po	fv2	65
B080	66	20x5	ccp/py	cm	po	fv2	66
B080	67	15x10	mt	dp	po	fv2	67
B117	68	5x4	ccp in py	mf	vi	fv2	68
B117	69	4x2	ccp in py	mf	vi	fv2	69
B117	69	6x4	ccp in py	mf	vi	fv2	70
B117	71	6x4	ccp in py	mf	vi	fv2	71
B117	72	9x5	ccp in py	mf	vi	fv2	72
B117	73	5x5	py	mf	vi	fv2	73
B117	73	15x2	py	mf	vi	fv2	74
B117	73	5x2	py	mf	vi	fv2	75
B117	73	10x2	py	mf	vi	fv2	76
B117	77a	10x5	ccp in py	mf	vi	fv2	77
B117	77a	5x2	ccp in py	mf	vi	fv2	78
B117	77a	10x2	ccp in py	mf	vi	fv2	79
B117	77b	10x5	ccp in py	mf	vi	fv2	80
B117	81	30x10	ccp in py	mf	vi	fv2	81
B117	82	30x3	ccp in py	mf	vi	fv2	82

James Hewett
Ernest Henry Gold and Pyrite

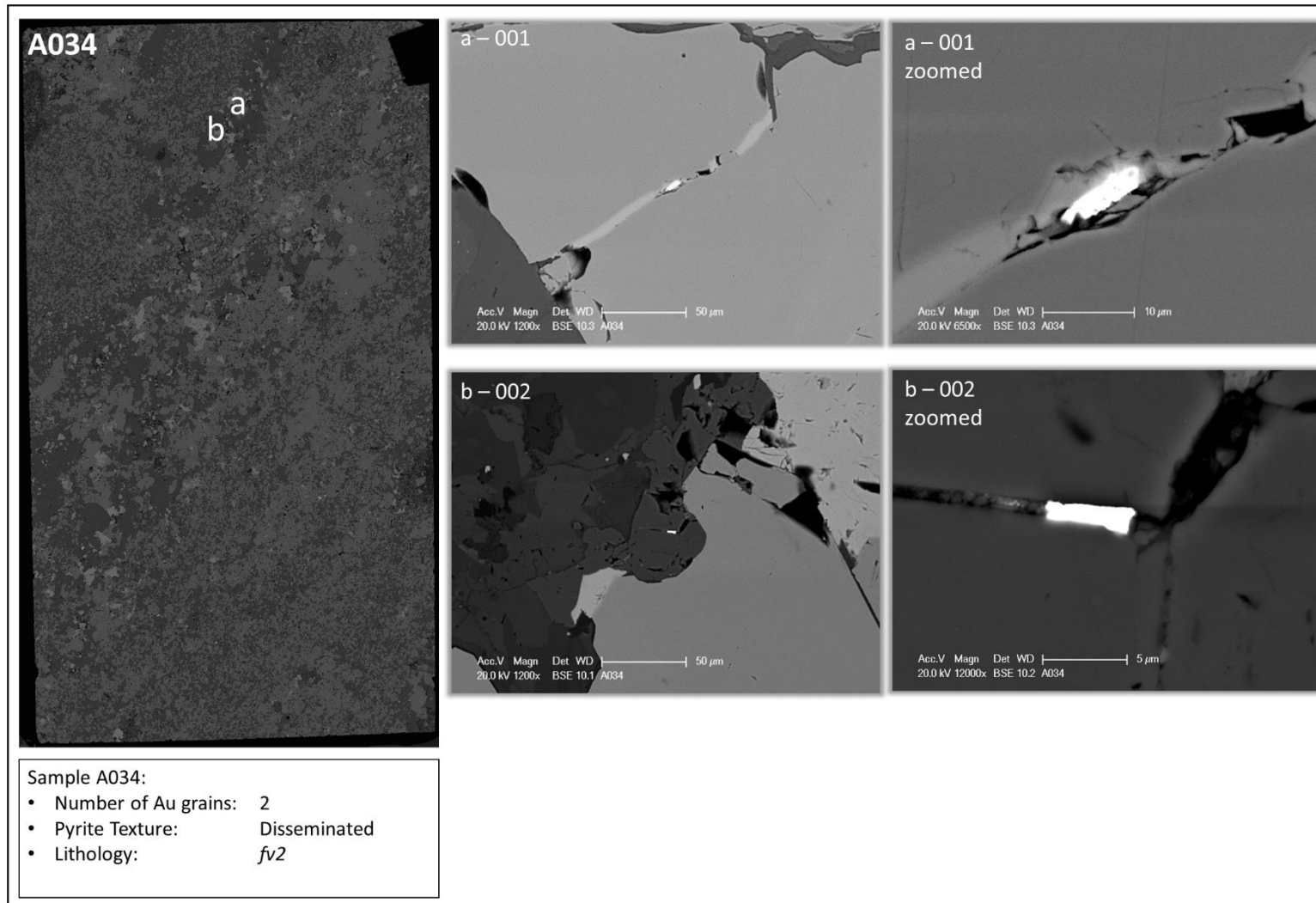
B117	83	10x5	ccp in py	mf	vi	fv2	83
B117	84	20x3	ccp in py	mf	vi	fv2	84
B117	84	8x4	ccp in py	mf	vi	fv2	85
B117	84	5x3	ccp in py	mf	vi	fv2	86
B117	87a	15x4	py	mf	vi	fv2	87
B117	87b	15x10	py	mf	vi	fv2	88
B117	89	5x2	ccp in py	mf	vi	fv2	89
B117	89	15x3	ccp in py	mf	vi	fv2	90
B117	91	2x2	ccp in py	mf	vi	fv2	91
B194	92a	7x4	ccp in py	mf	vi	fv1	92
B194	92b	15x2	ccp in py	mf	vi	fv1	93
B194	94a	8x2	ccp in py	mf	vi	fv1	94
B194	94a	8x4	ccp in py	mf	vi	fv1	95
B194	94b	110x2	ccp in py	mf	vi	fv1	96
B194	97	30X4	ccp/py	cm	vi	fv1	97
B194	98	3x2	In La-Ce-O-F	dp	vi	fv1	98
B204	99a	30X5	py	dp	vi	fv2	99
B204	99b	14x5	py	dp	vi	fv2	100
B204	99c	5x5	py	dp	vi	fv2	101
B204	102	20x4	py	mf	vi	fv2	102
B204	103	12x2	py	dp	vi	fv2	103
B207	104	3x3	ccp/py	dp	di	fv2	104
B207	105	10x2	py	mf	di	fv2	105
B207	105	5x5	ccp/py	cm	di	fv2	106
B207	107	20x2	ca in py	mf	di	fv2	107
B207	107	10x2	ca in py	mf	di	fv2	108
B207	107	4x2	ca in py	mf	di	fv2	109
B207	107	6x2	ca in py	mf	di	fv2	110
B207	111	10x4	mt	mf	di	fv2	111
B207	112	20x10	qz/mt	cm	di	fv2	112
B222	113	10x5	ccp/kf/py	cm	po	fv2	113
B247	114	5x2	ccp in py	mf	po	iv	114

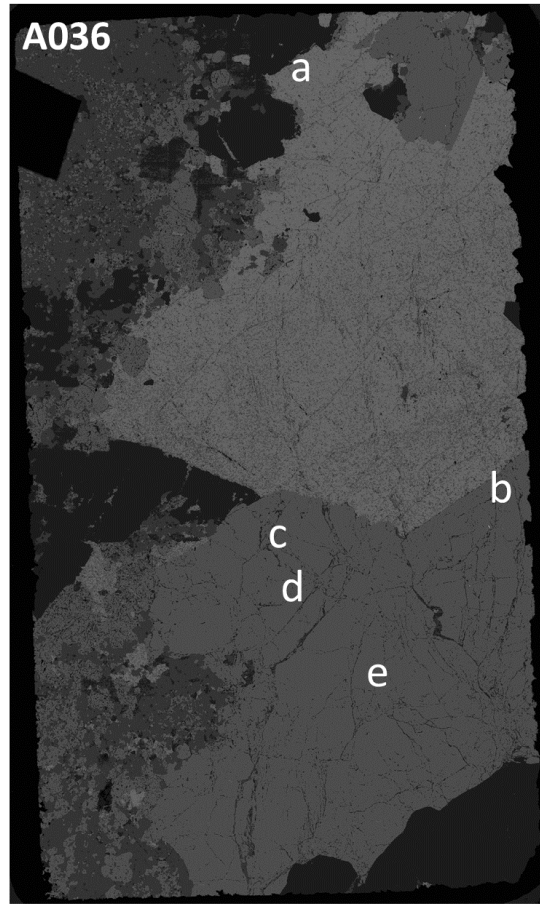
Sample C	Image ID	Size (µm)	Mineralogical association	Textural Site	py Texture	Lithology	ID
C002	115	5x3	ca/py	cm	vi	fv1	115
C045	116a	20x3	ccp in py	mf	po	fv1	116
C045	116b	8x8	ccp in py	mf	po	fv1	117
C045	116b	3x2	ccp in py	mf	po	fv1	118
C071	119	5x4	ccp/py	dp	po	fv1	119
C071	120	15x6	py	dp	po	fv1	120
C071	121	4x2	ccp in py	mf	po	fv1	121
C071	122	20x10	ccp/py	mf	po	fv1	122
C071	123	10x5	py	dp	po	fv1	123
C071	124	15x4	ca/kf in py	mf	po	fv1	124

James Hewett
Ernest Henry Gold and Pyrite

C071	125	30x10	ccp/py	cm	po	fv1	125
C071	126	30x4	ccp/qz/py	mf	po	fv1	126
C077	127	25x20	ccp	dp	vi	piv	127
C077	127	4x2	ccp	dp	vi	piv	128
C077	127	8x3	ccp	dp	vi	piv	129
C077	127	4x4	ccp	dp	vi	piv	130
C077	127	4x4	ccp	dp	vi	piv	131
C077	132	20x10	ccp	dp	vi	piv	132
C125	133	4x2	kf in py	mf	vi	fv2	133
C125	133	5x2	kf in py	mf	vi	fv2	134
C125	133	6x2	kf in py	mf	vi	fv2	135
C125	136	2x2	ccp in py	mf	vi	fv2	136
C125	137	2x2	ccp in py	mf	vi	fv2	137
C125	138	8x8	ccp/py	dp	vi	fv2	138
C125	138	2x2	ccp/py	dp	vi	fv2	139
C125	140	4x4	bi/kf	dp	vi	fv2	140
C144	141	15x5	ccp/py	dp	po	fv2	141
C144	142a	10x2	ccp in py	mf	po	fv2	142
C144	142b	5x2	ccp in py	mf	po	fv2	143
C144	142c	10x2	ccp in py	mf	po	fv2	144
C144	142c	14x2	ccp in py	mf	po	fv2	145
C144	146	10x2	ccp in py	mf	po	fv2	146
C144	146	4x4	ccp in py	mf	po	fv2	147
C144	146	4x4	ccp in py	mf	po	fv2	148
C144	149	5x2	ccp in py	mf	po	fv2	149
C144	149	5x2	ccp in py	mf	po	fv2	150
C144	151a	15x5	ccp in py	mf	po	fv2	151
C144	151a	4x2	ccp in py	mf	po	fv2	152
C144	151b	35x5	ccp/py	cm	po	fv2	153
C144	154a	5x5	bi/ca/kf/py	cm	po	fv2	154
C144	154b	15x2	py	mf	po	fv2	155
C144	154b	2x2	py	mf	po	fv2	156
C144	157	6x3	py	dp	po	fv2	157

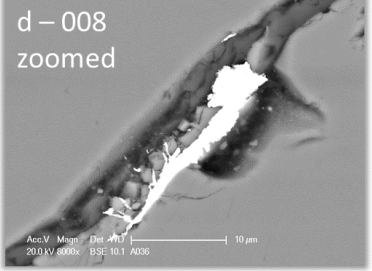
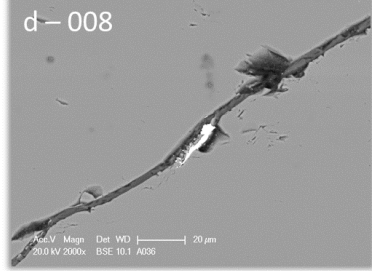
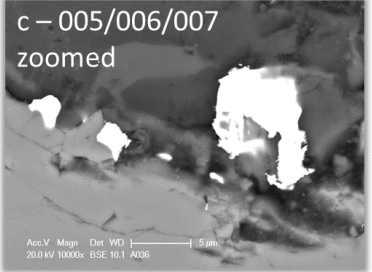
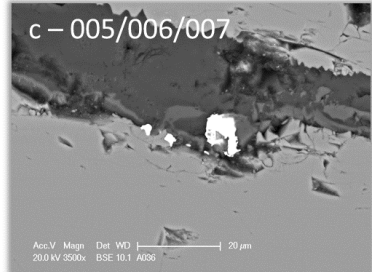
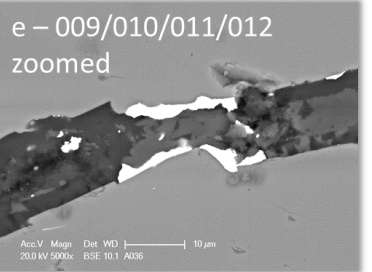
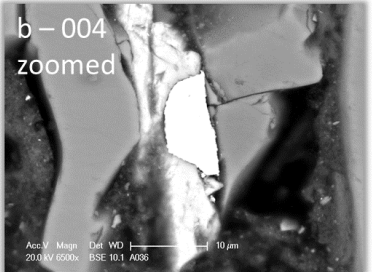
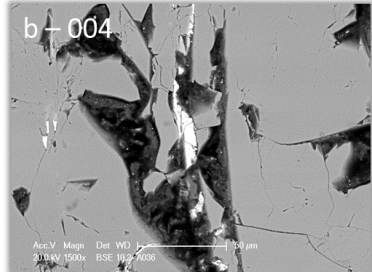
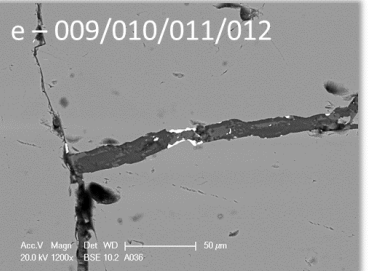
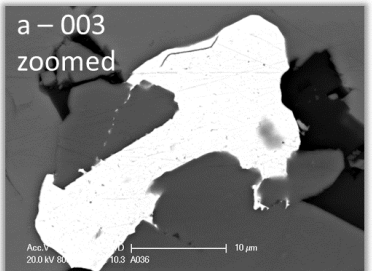
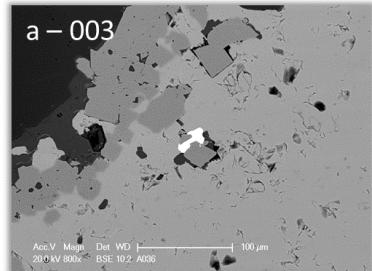
APPENDIX 2.B: EXTENDED IMAGES OF FREE GOLD

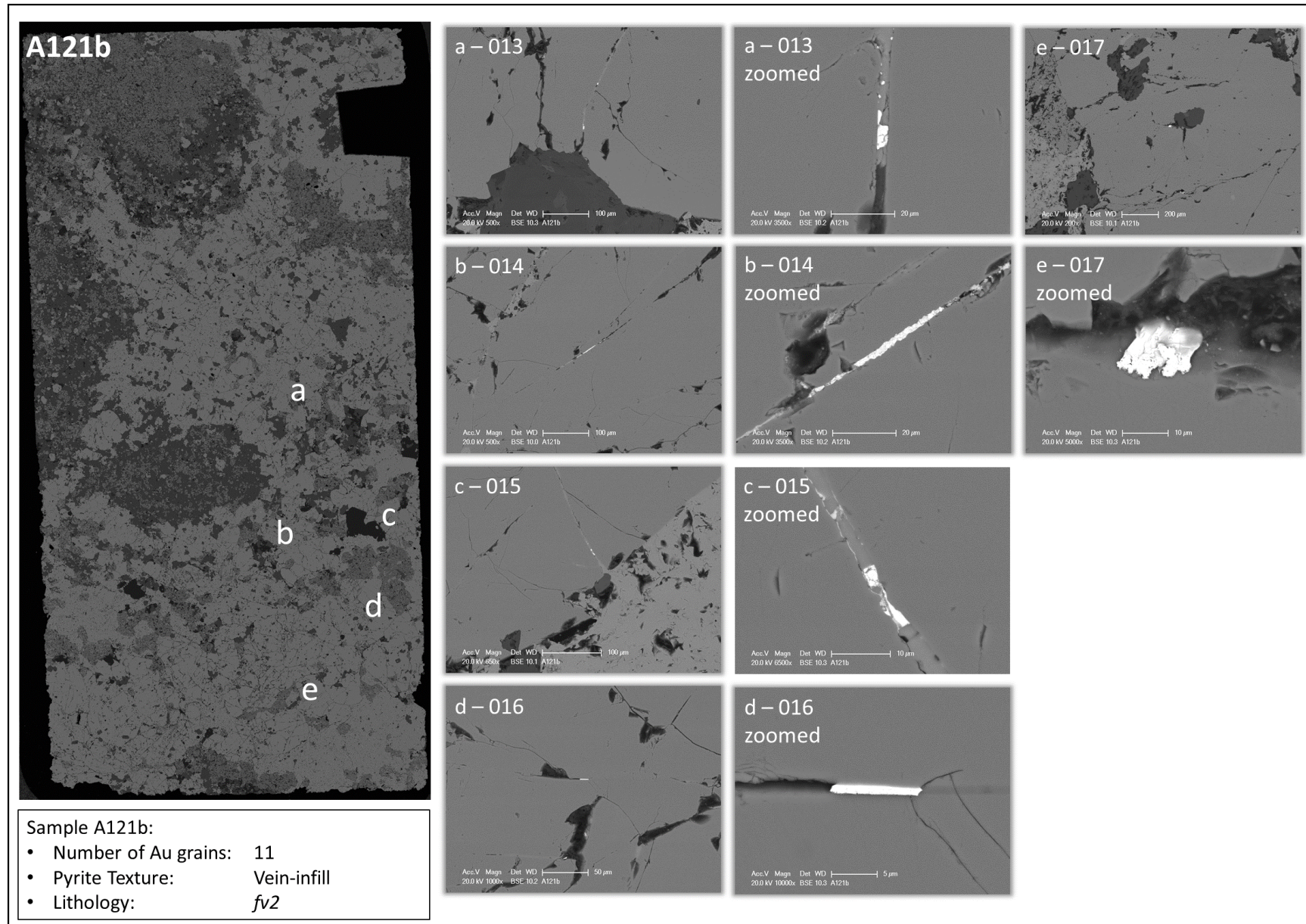


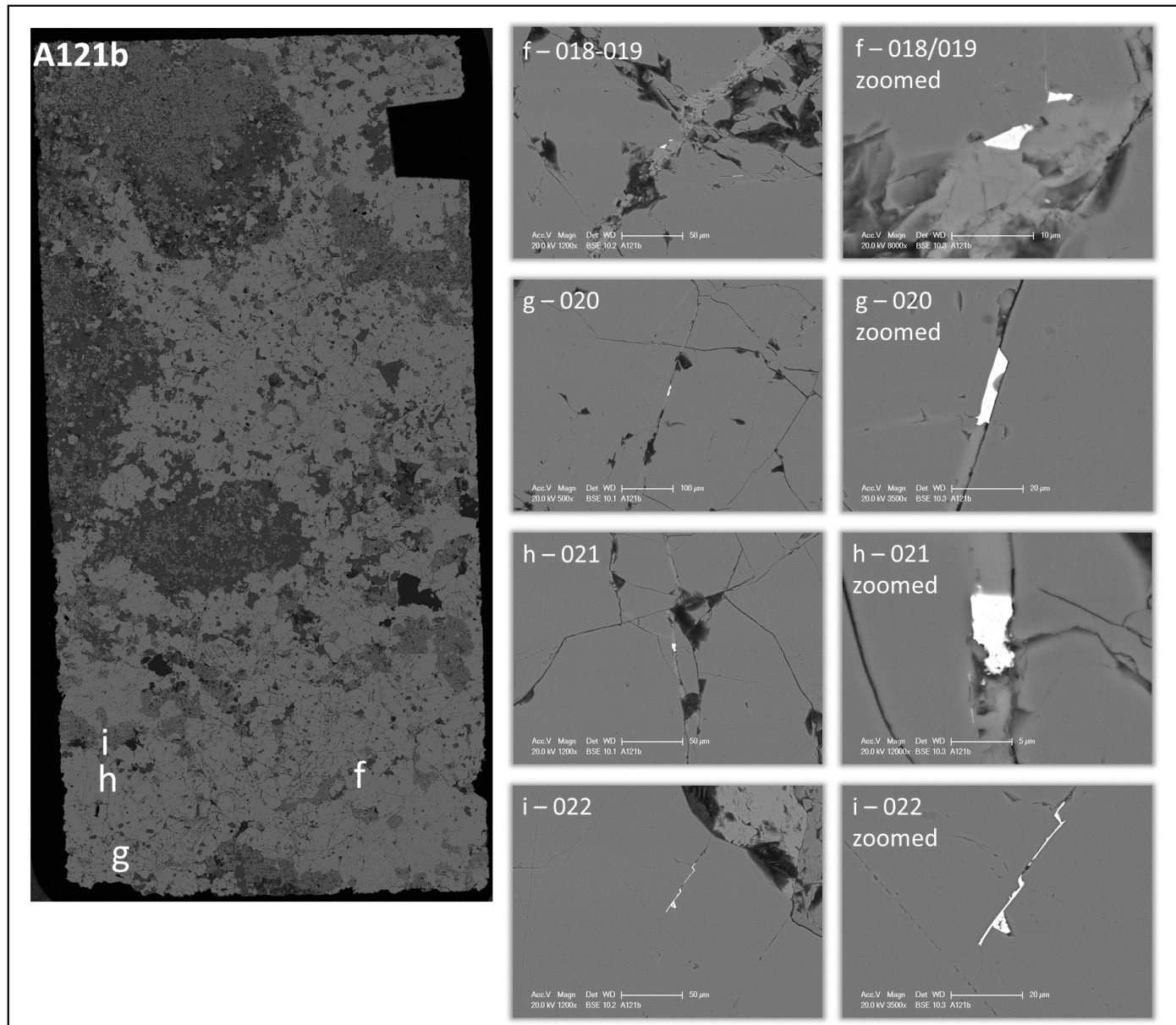


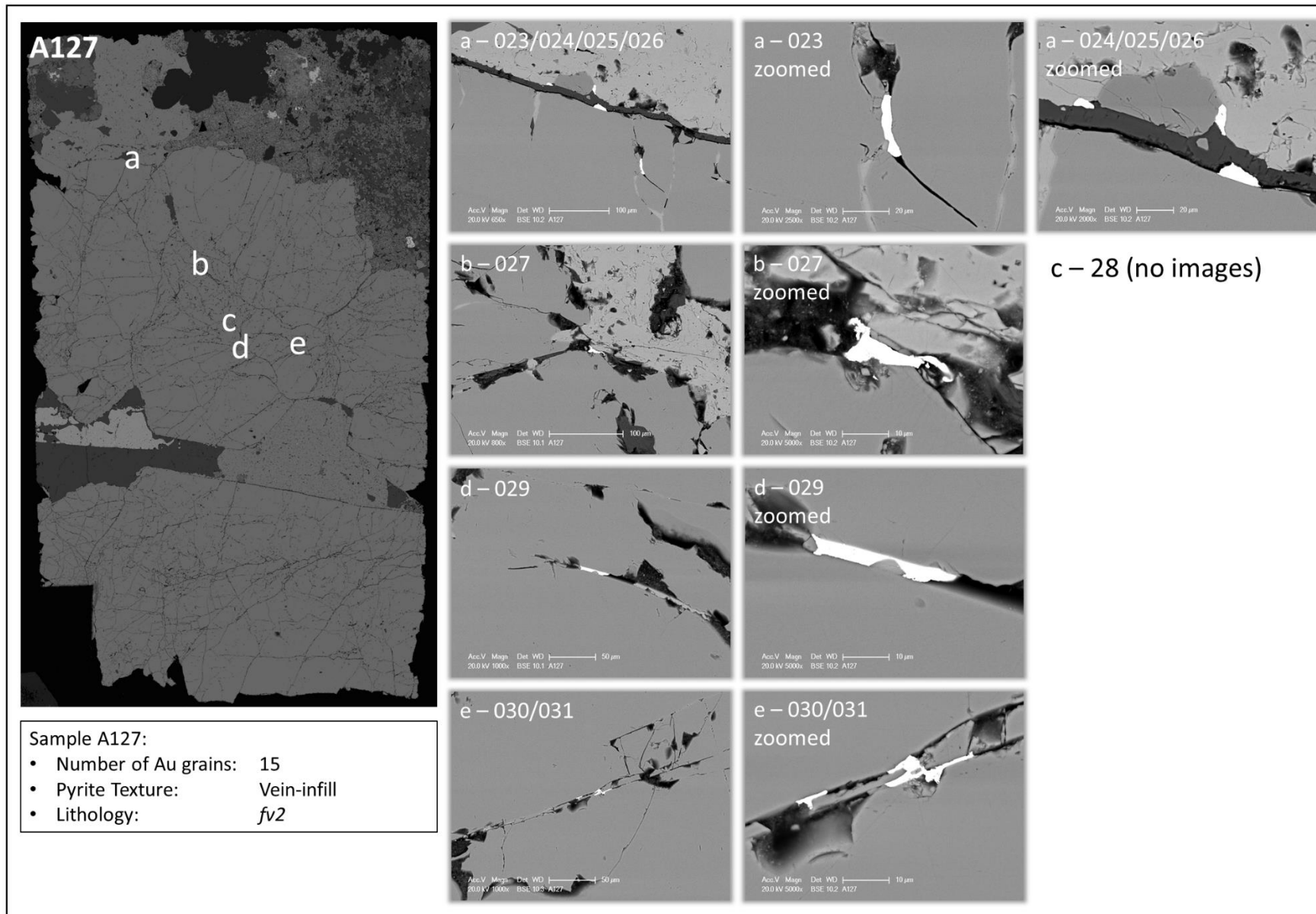
Sample A036:

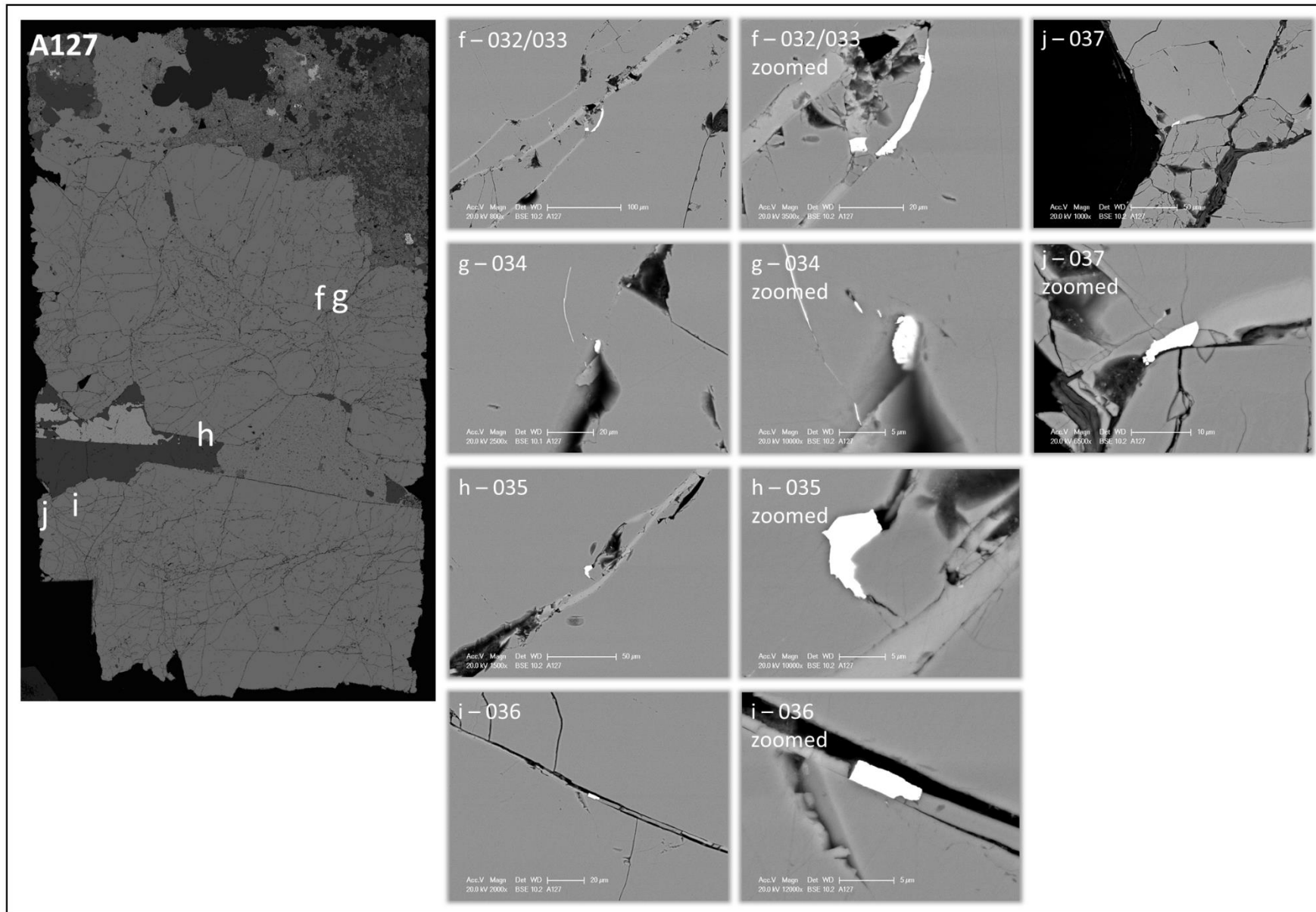
- Number of Au grains: 10
- Pyrite Texture: Vein-infill
- Lithology: fv2

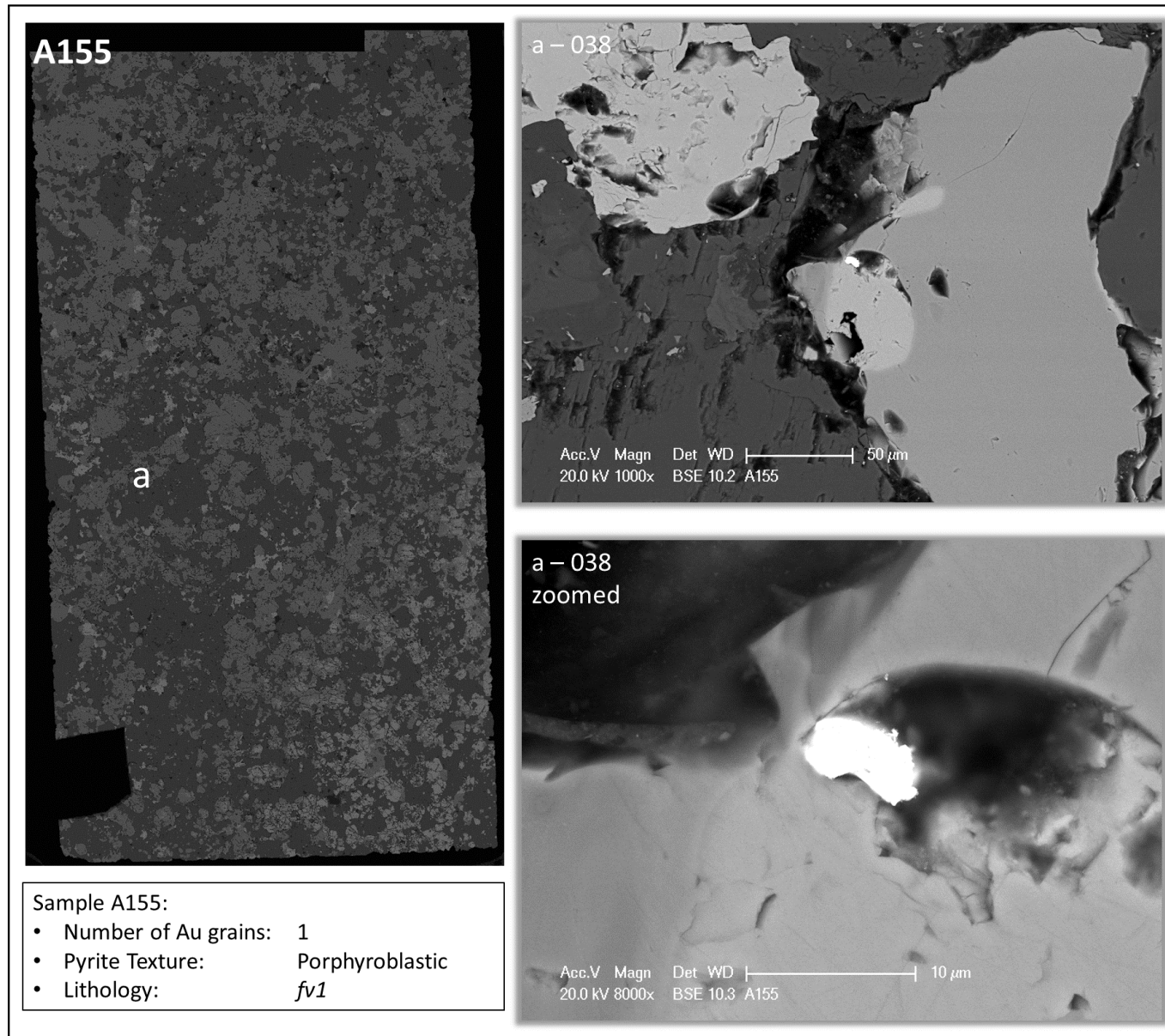


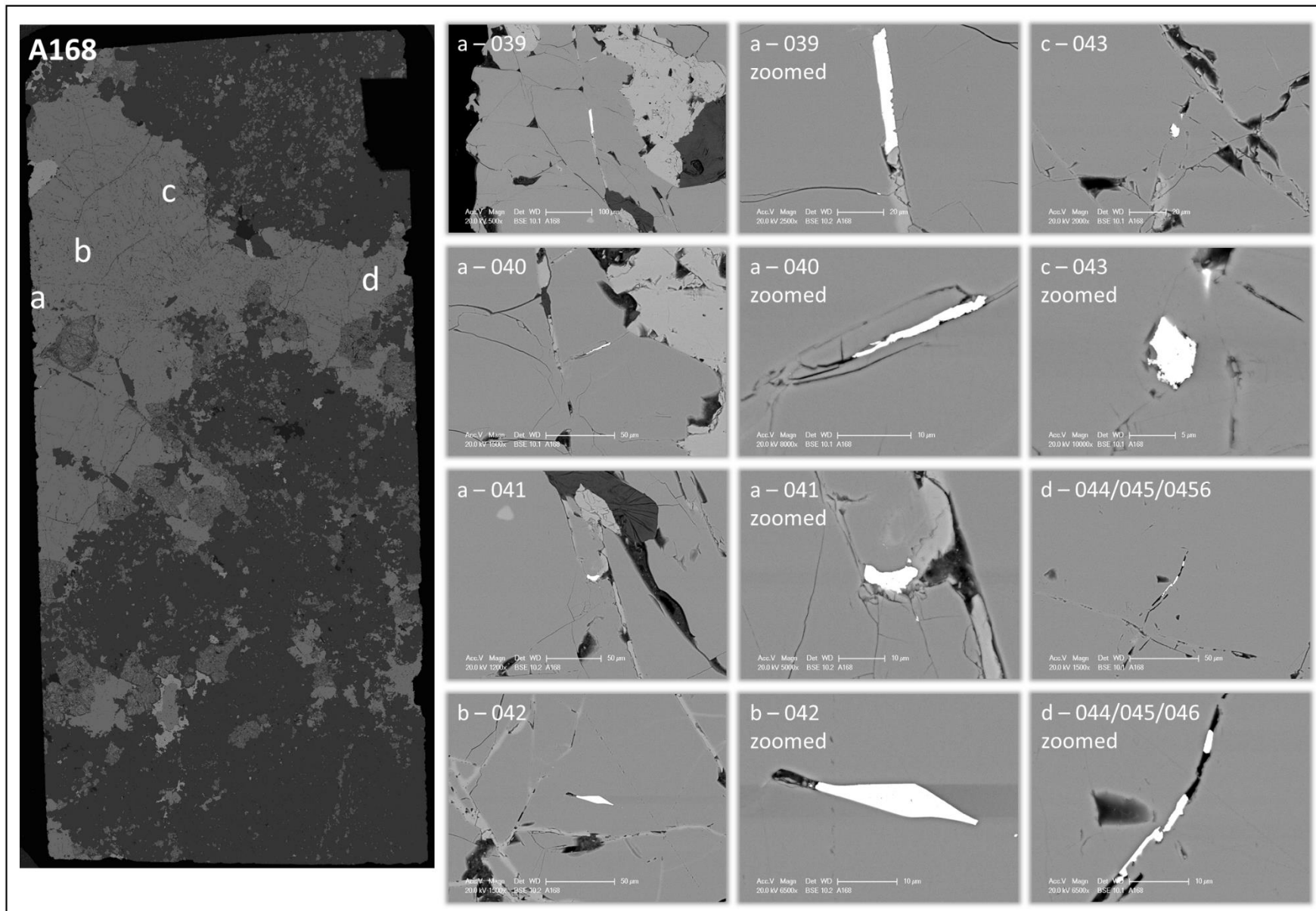


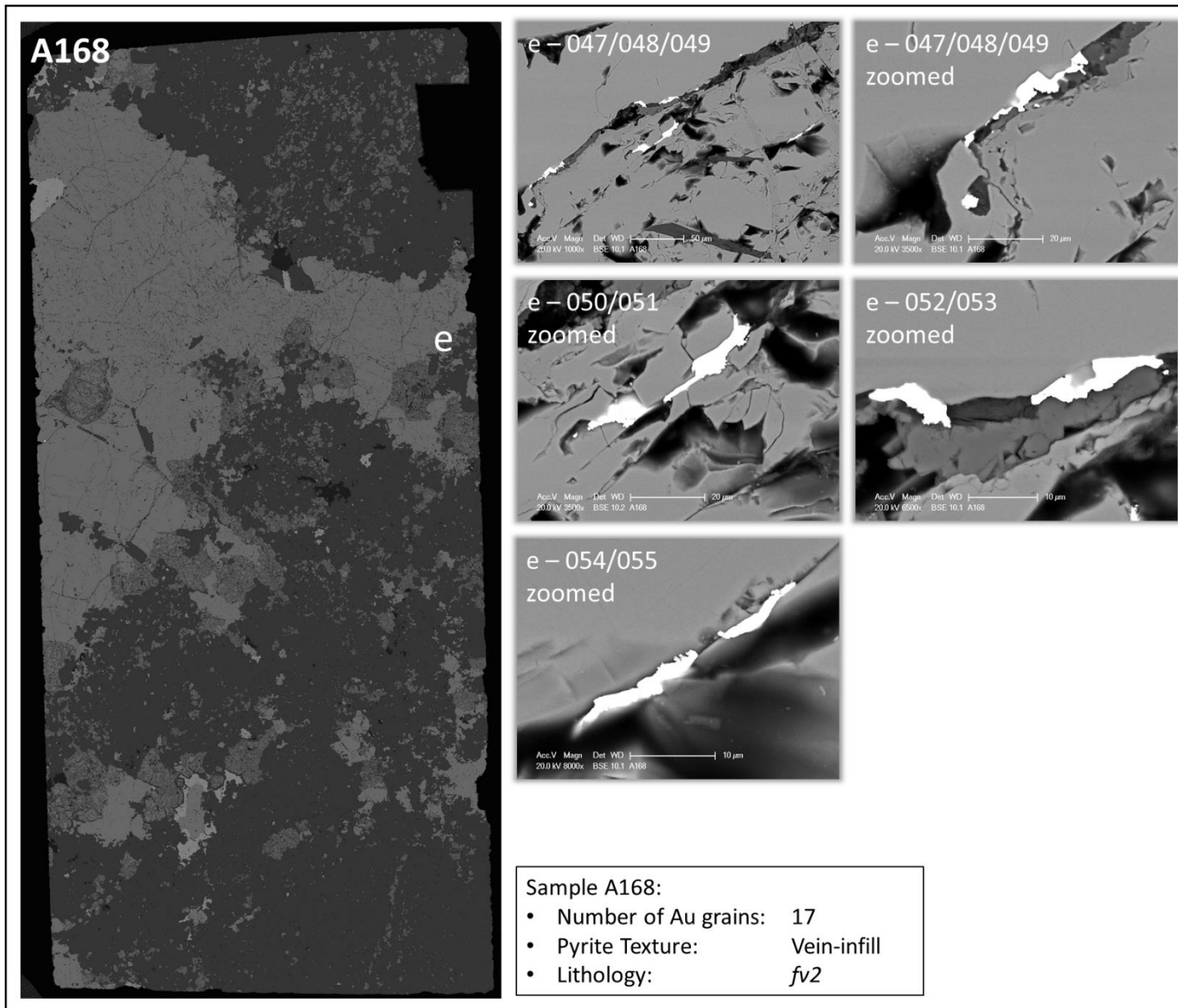


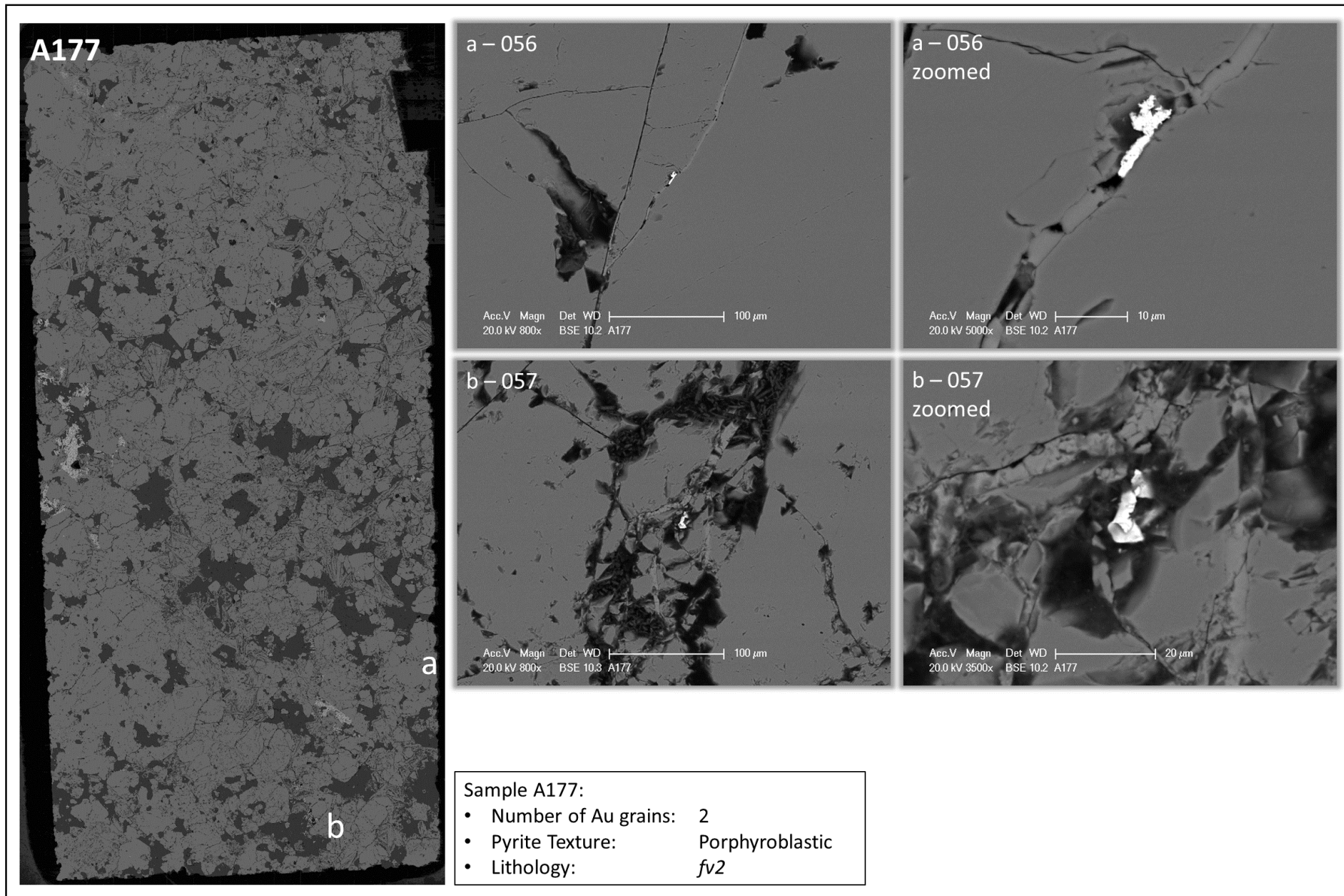


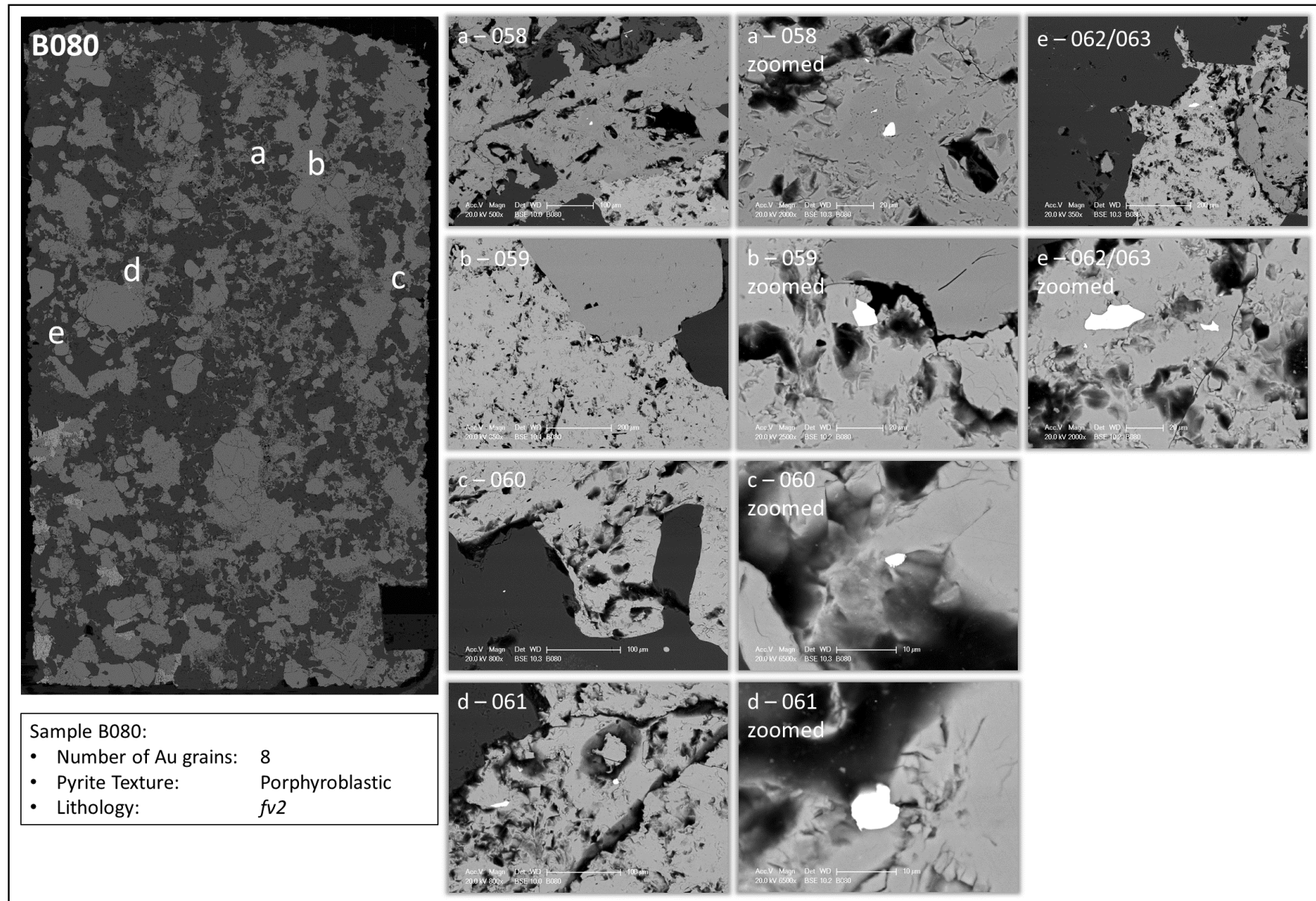


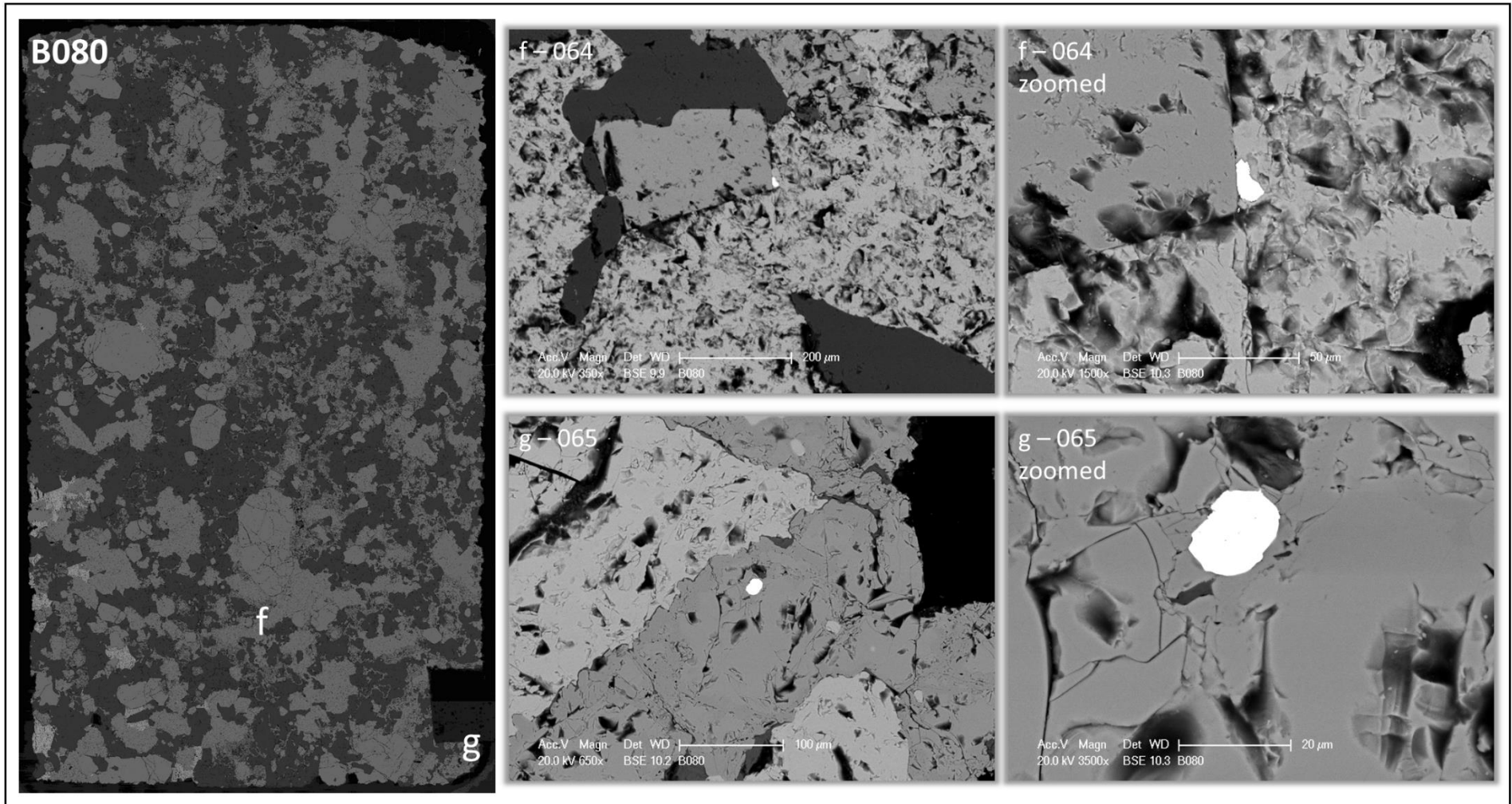


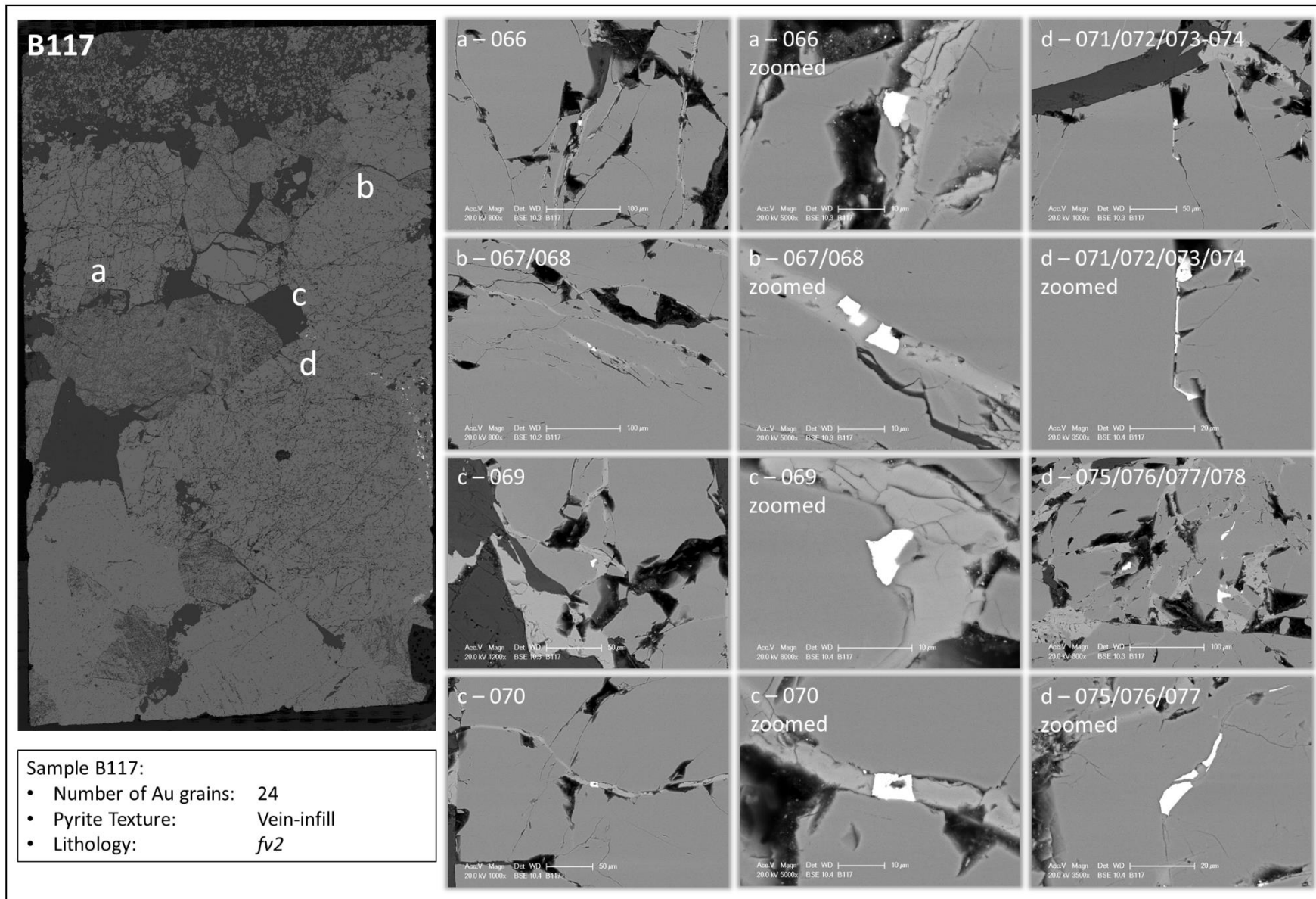


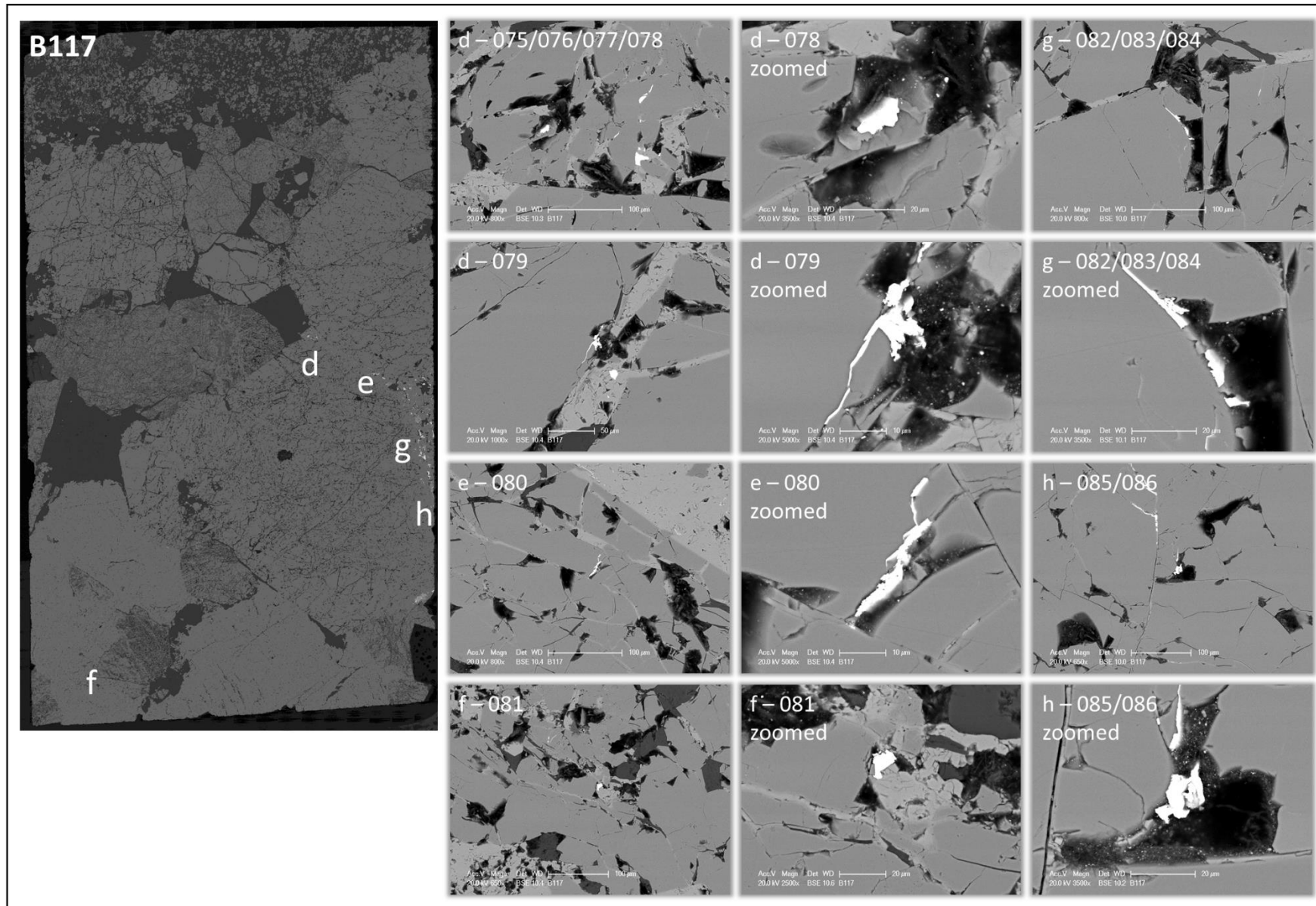


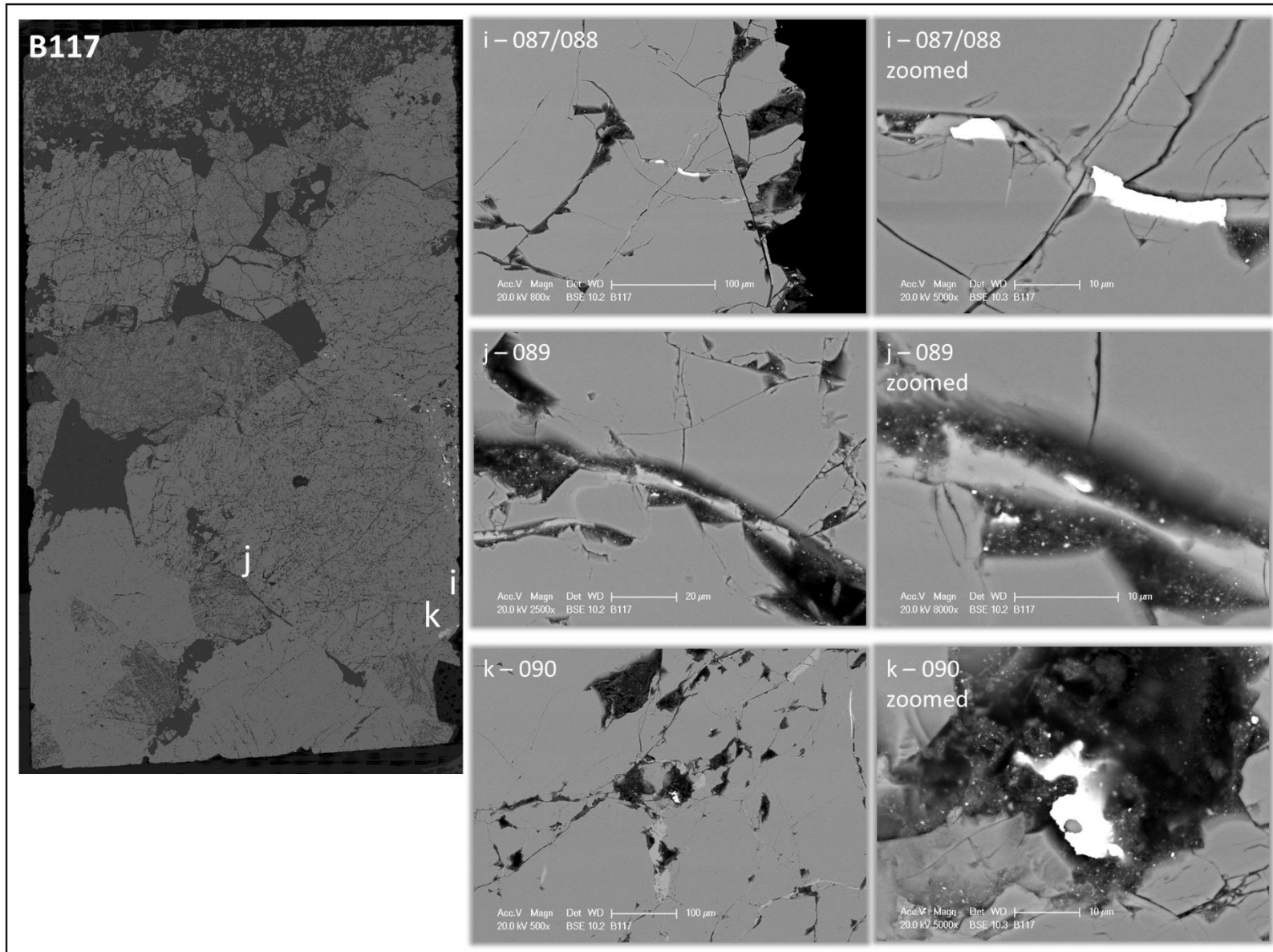


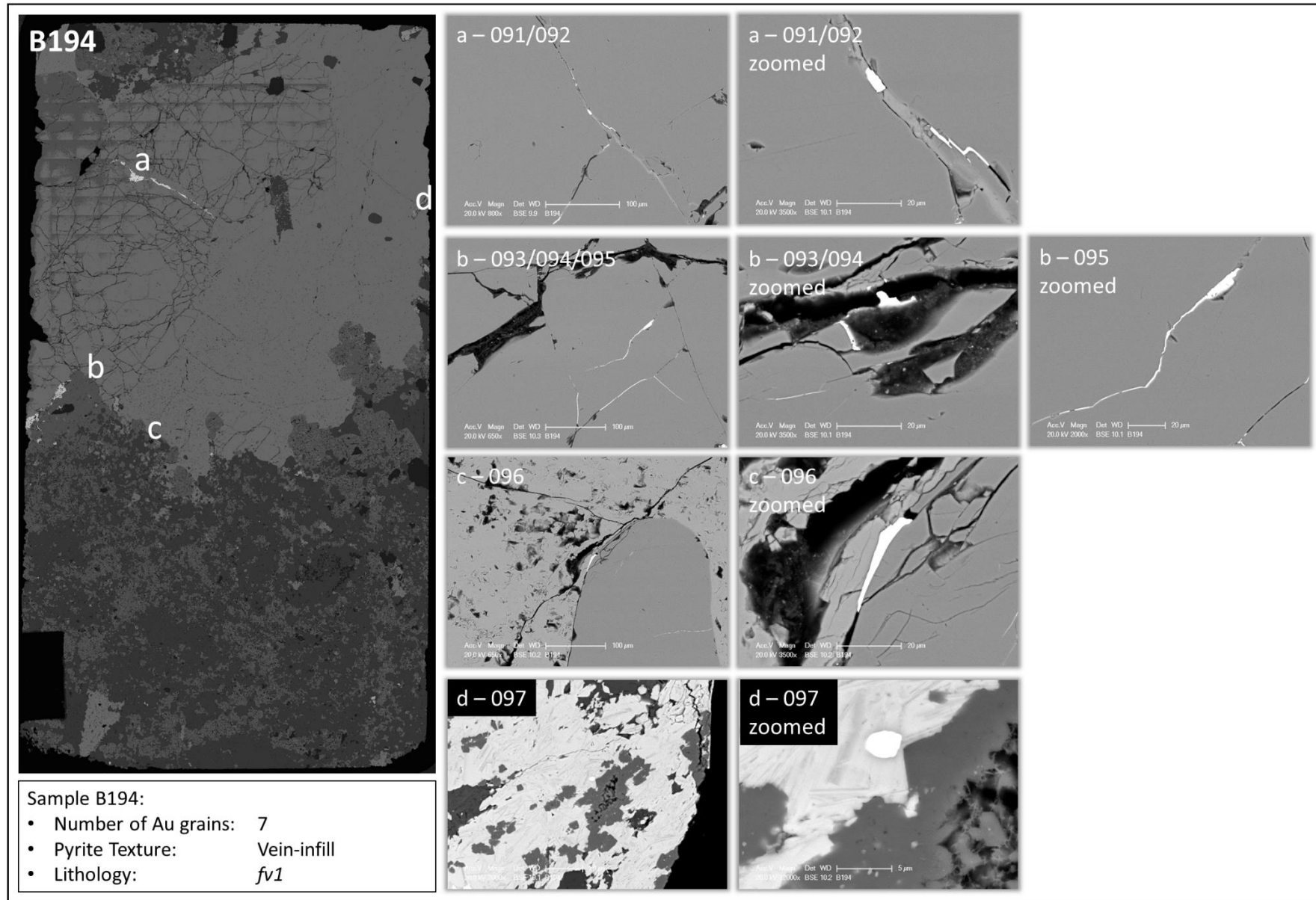


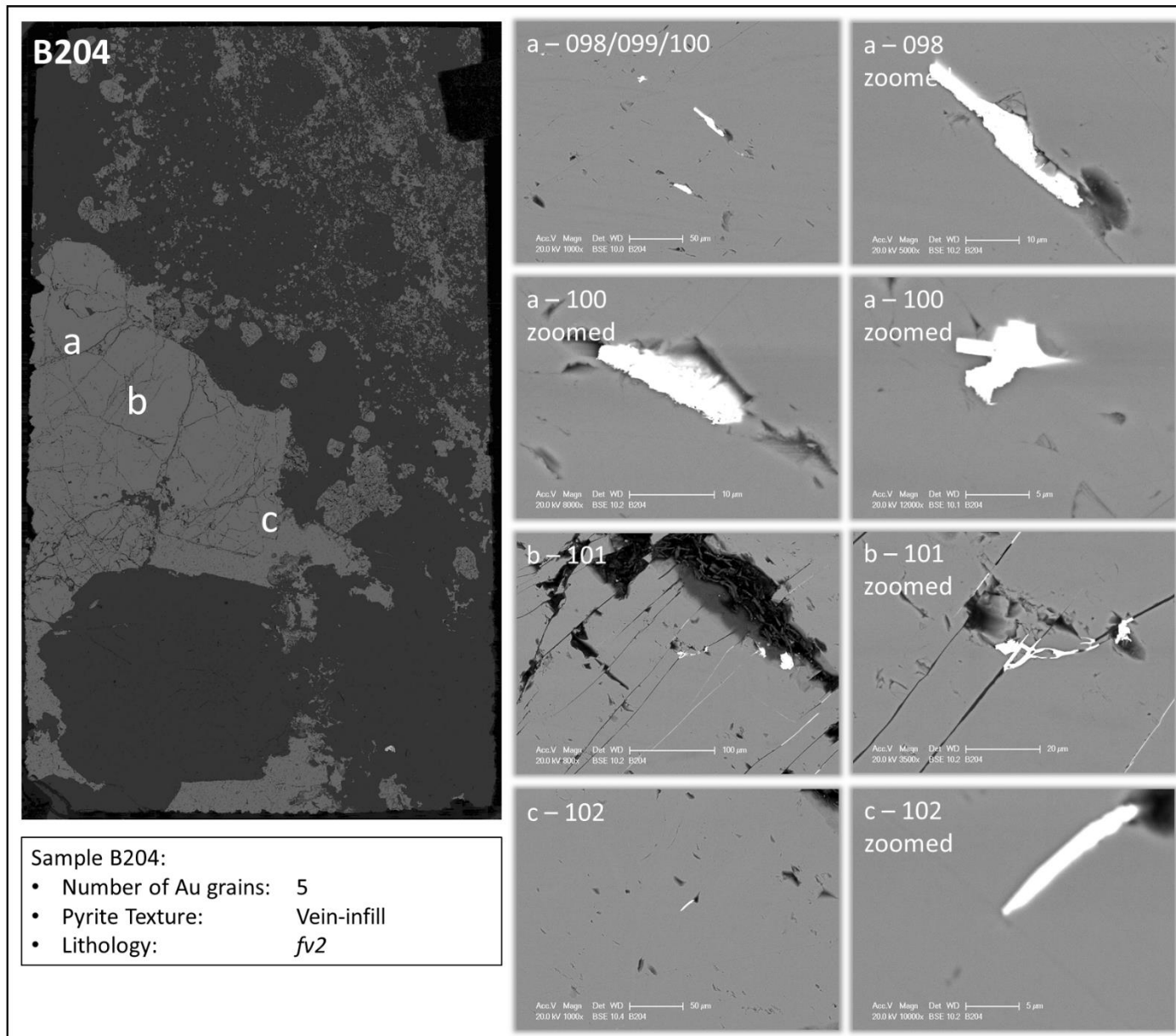


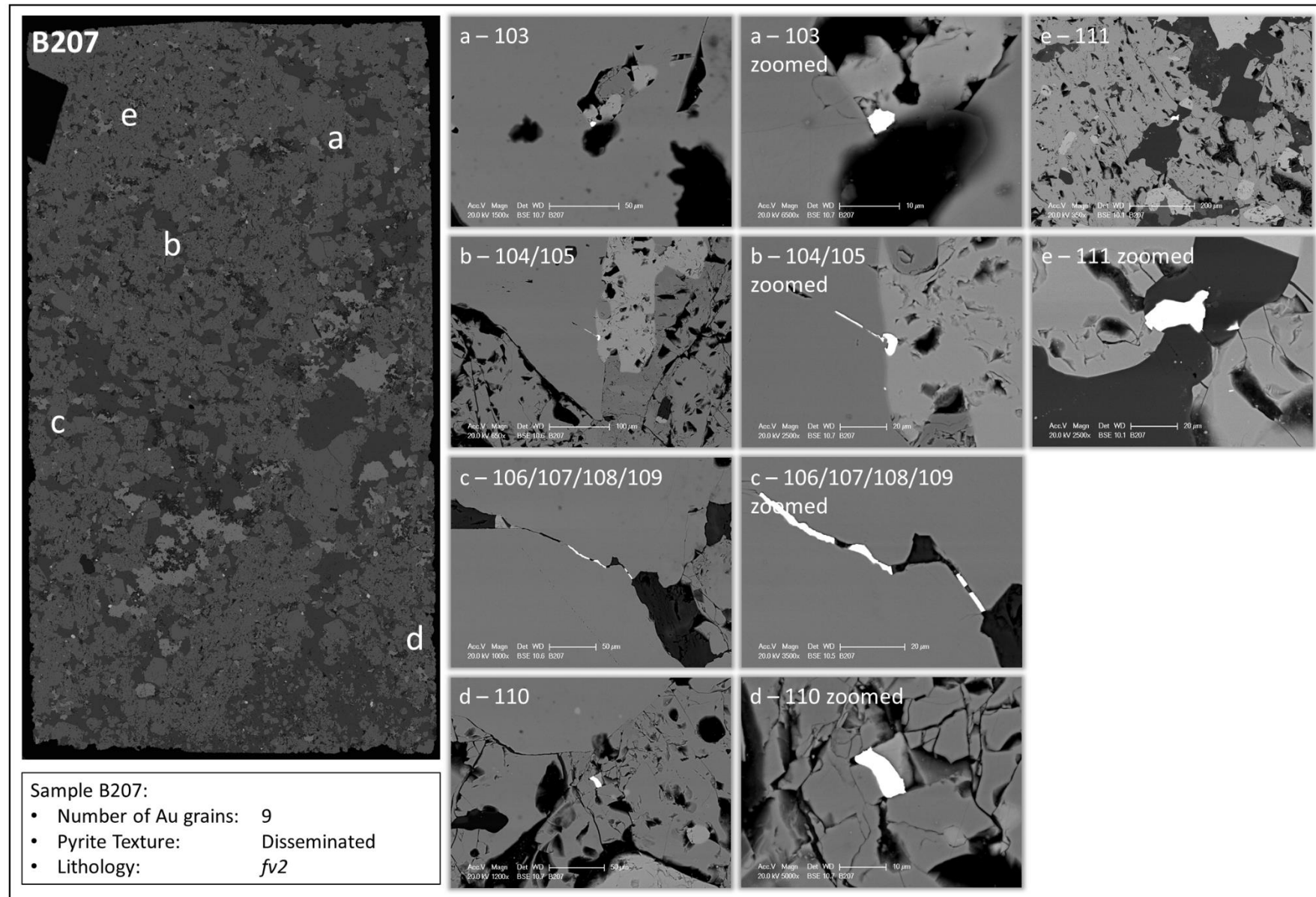


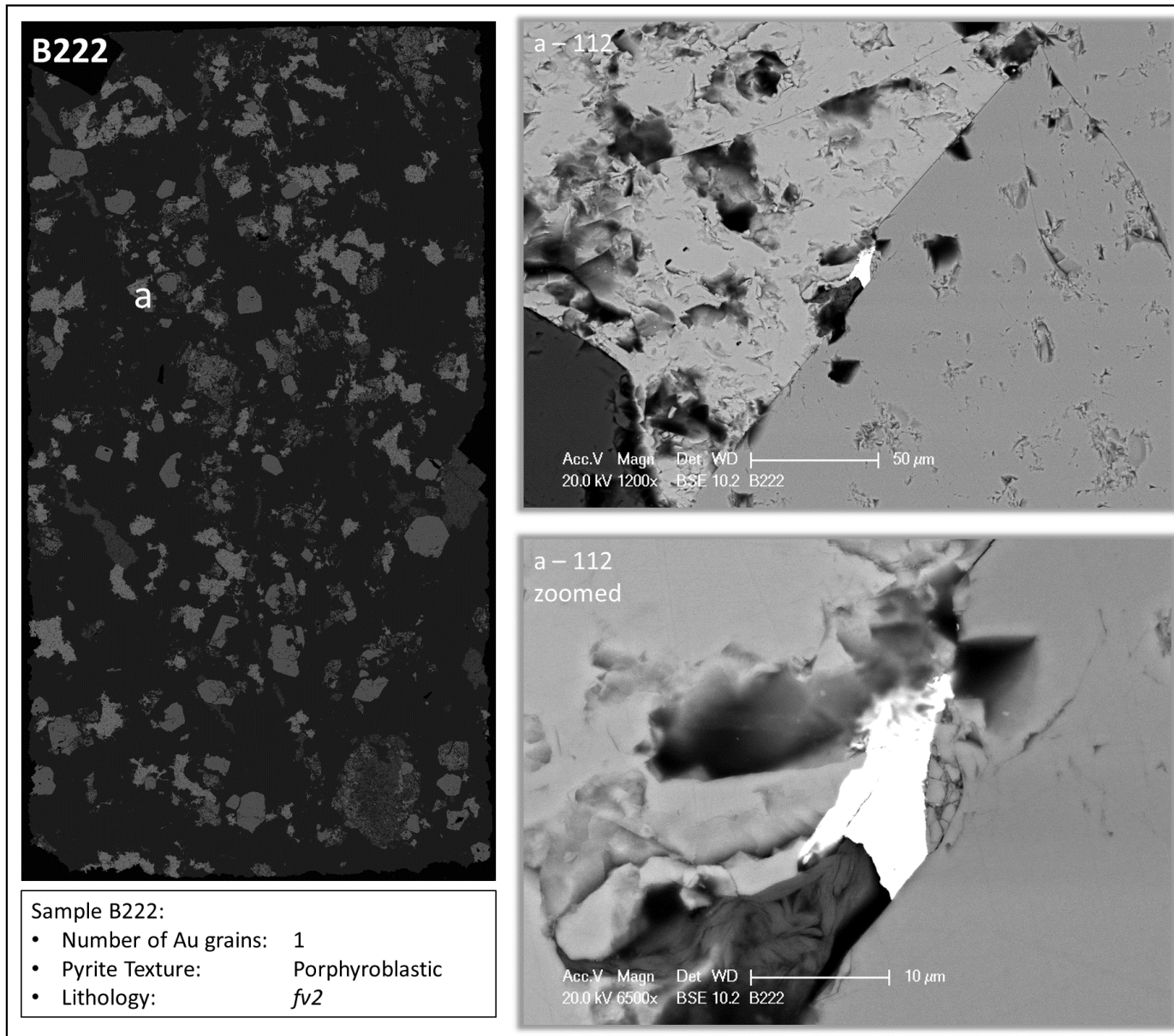


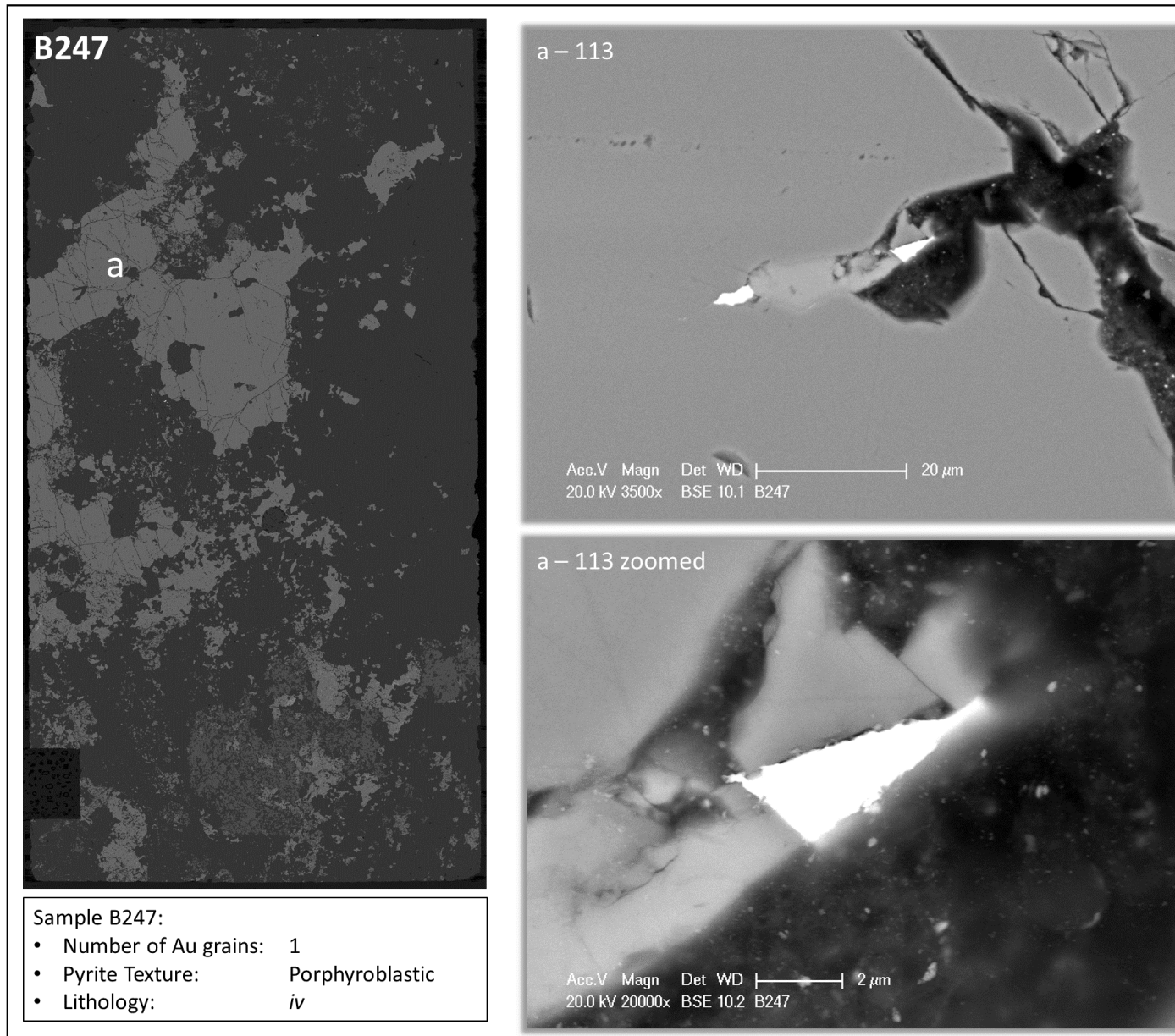


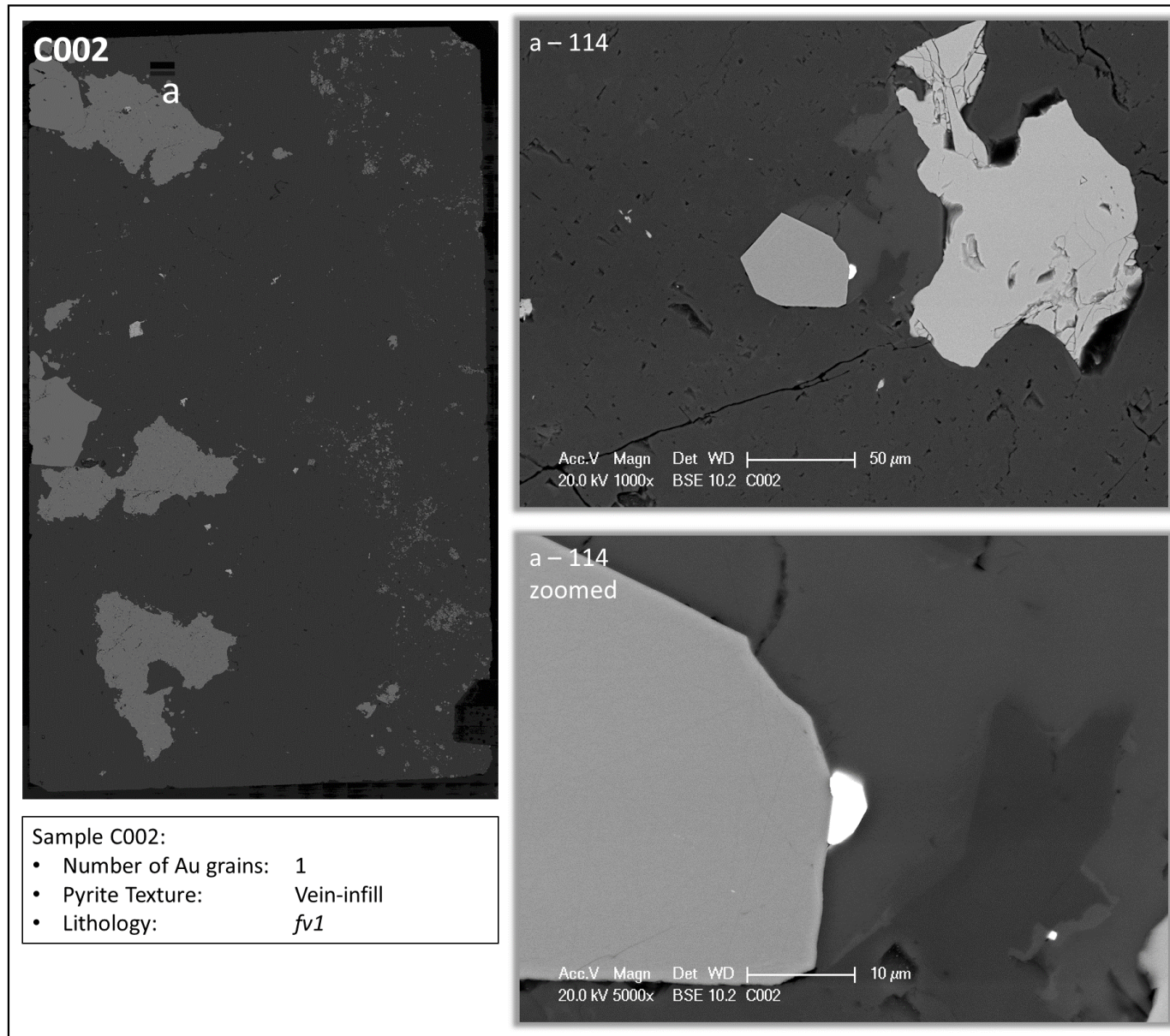


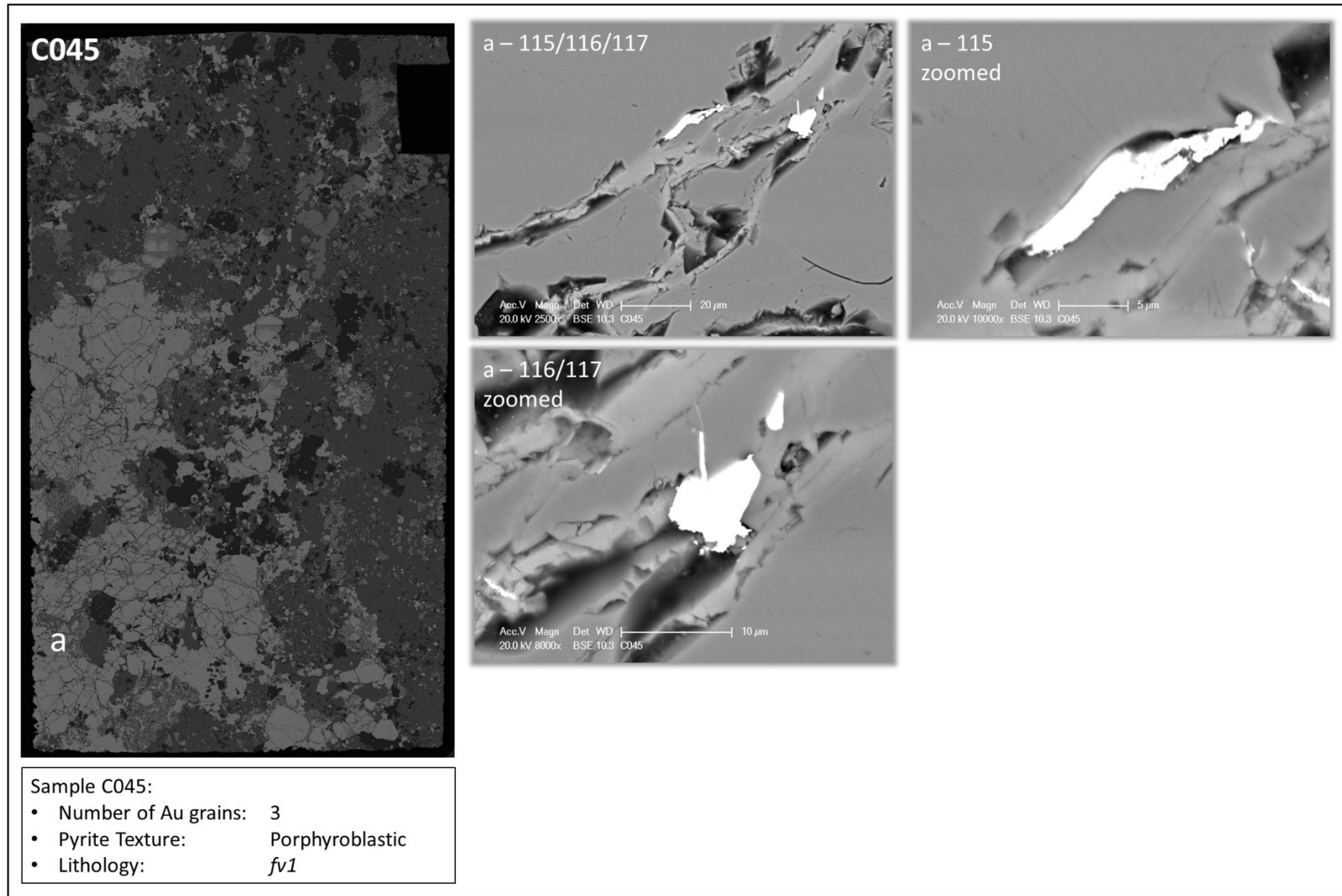


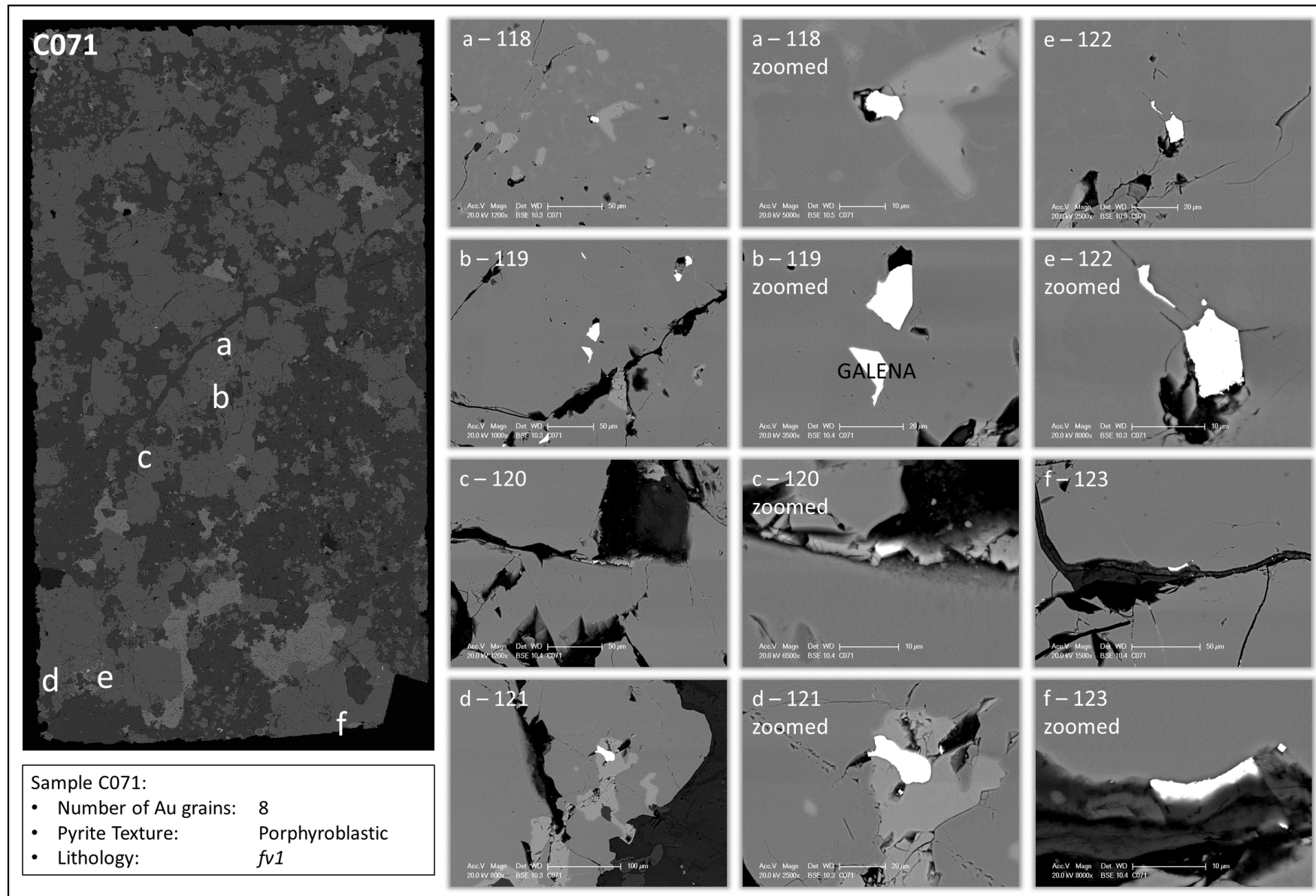


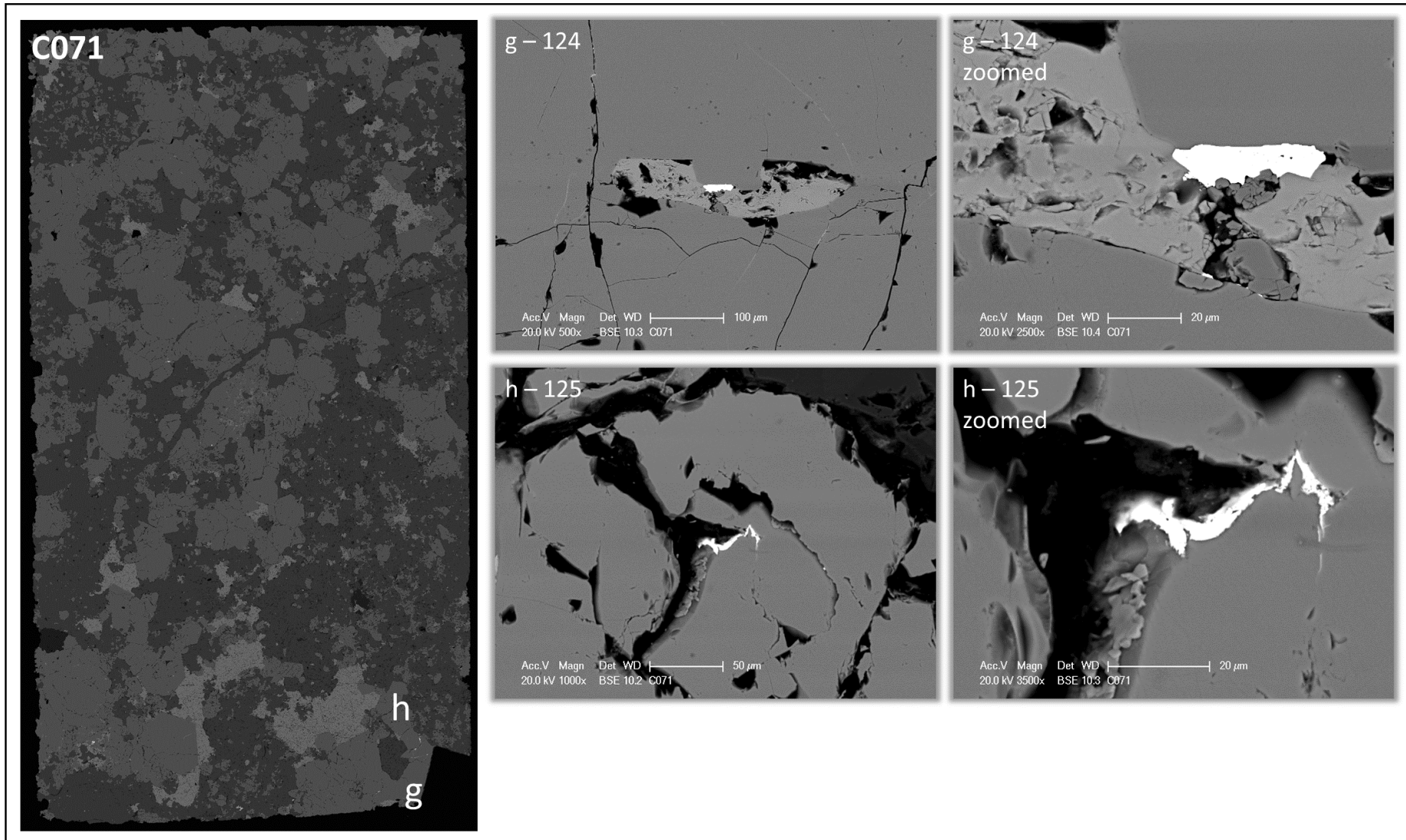


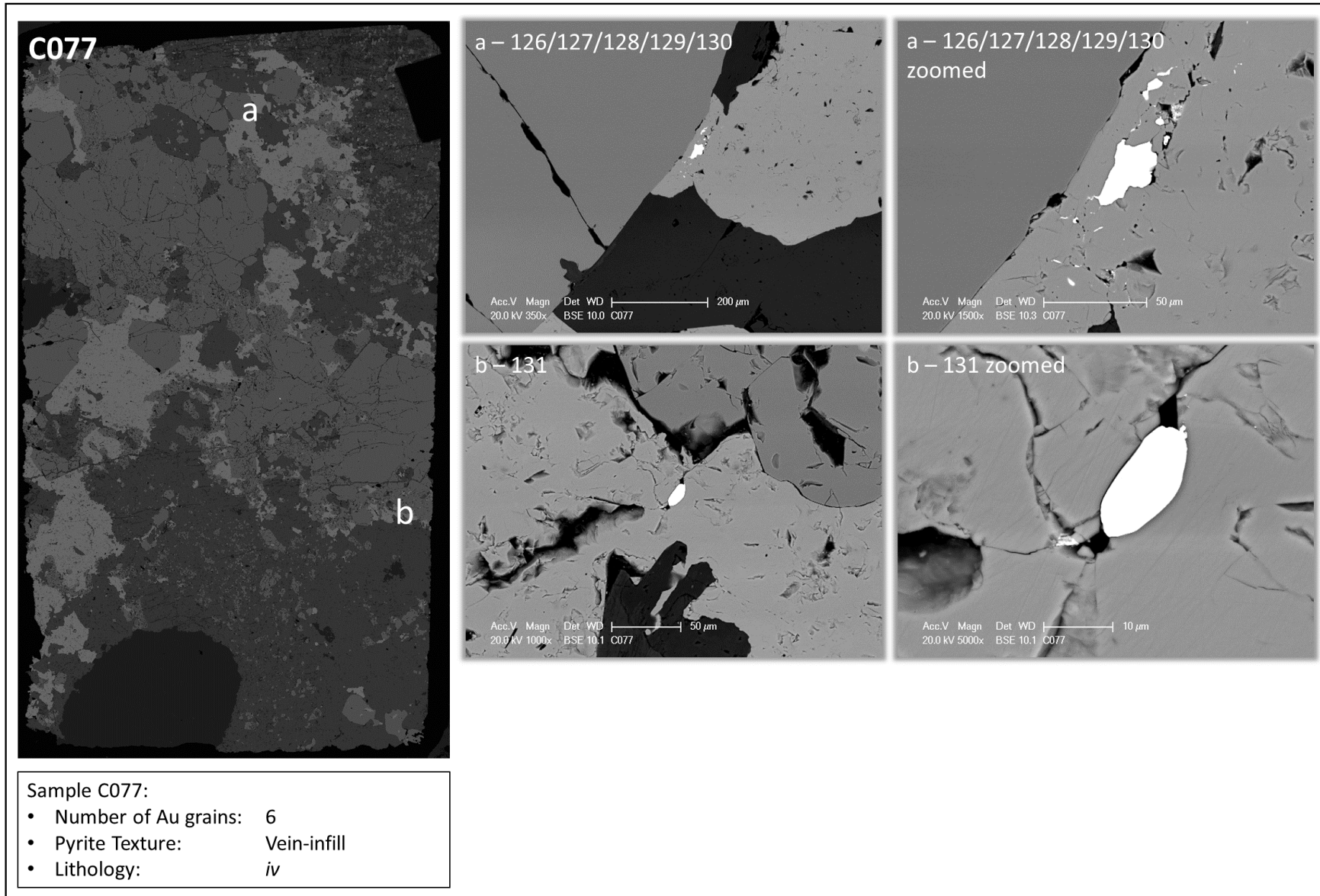


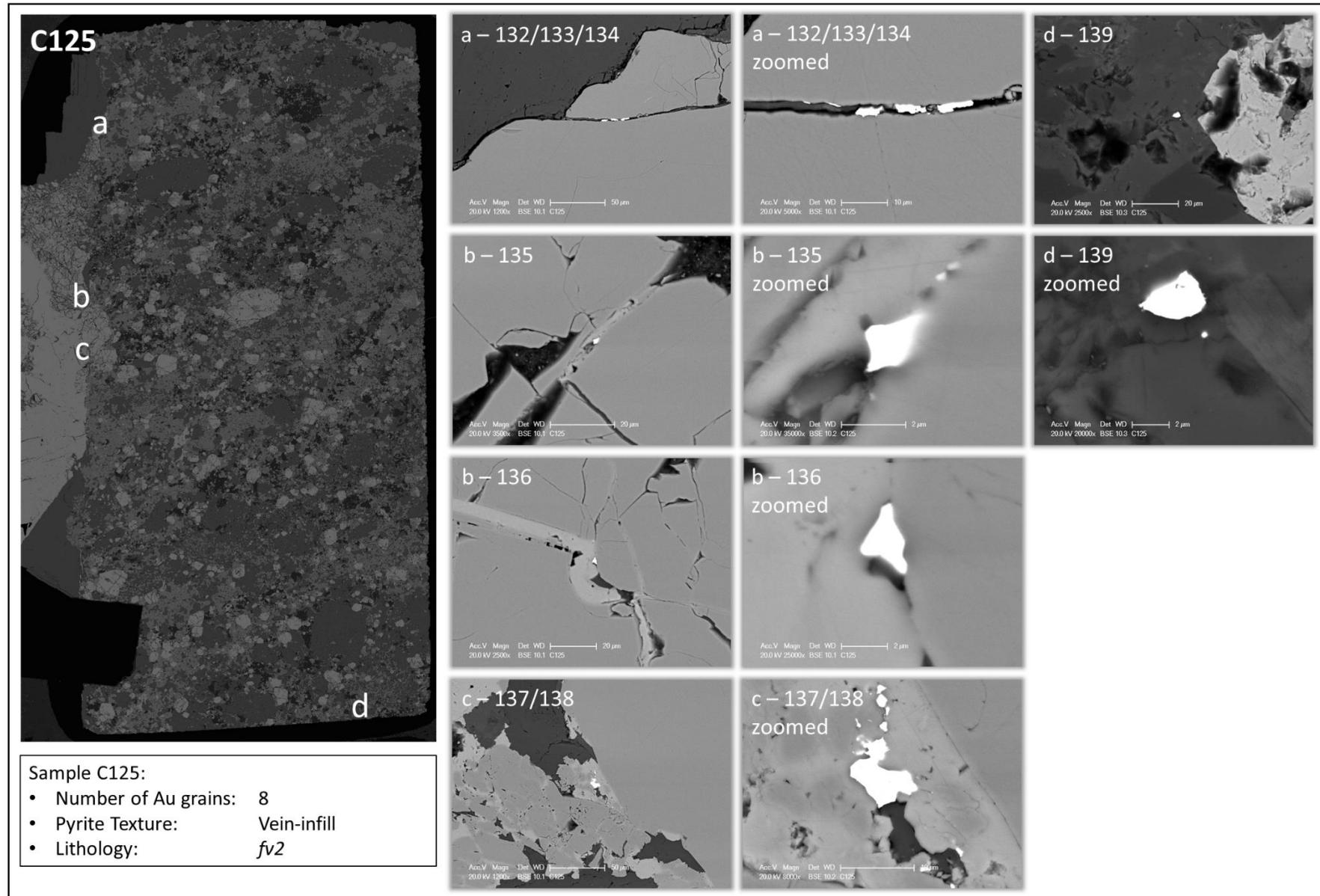


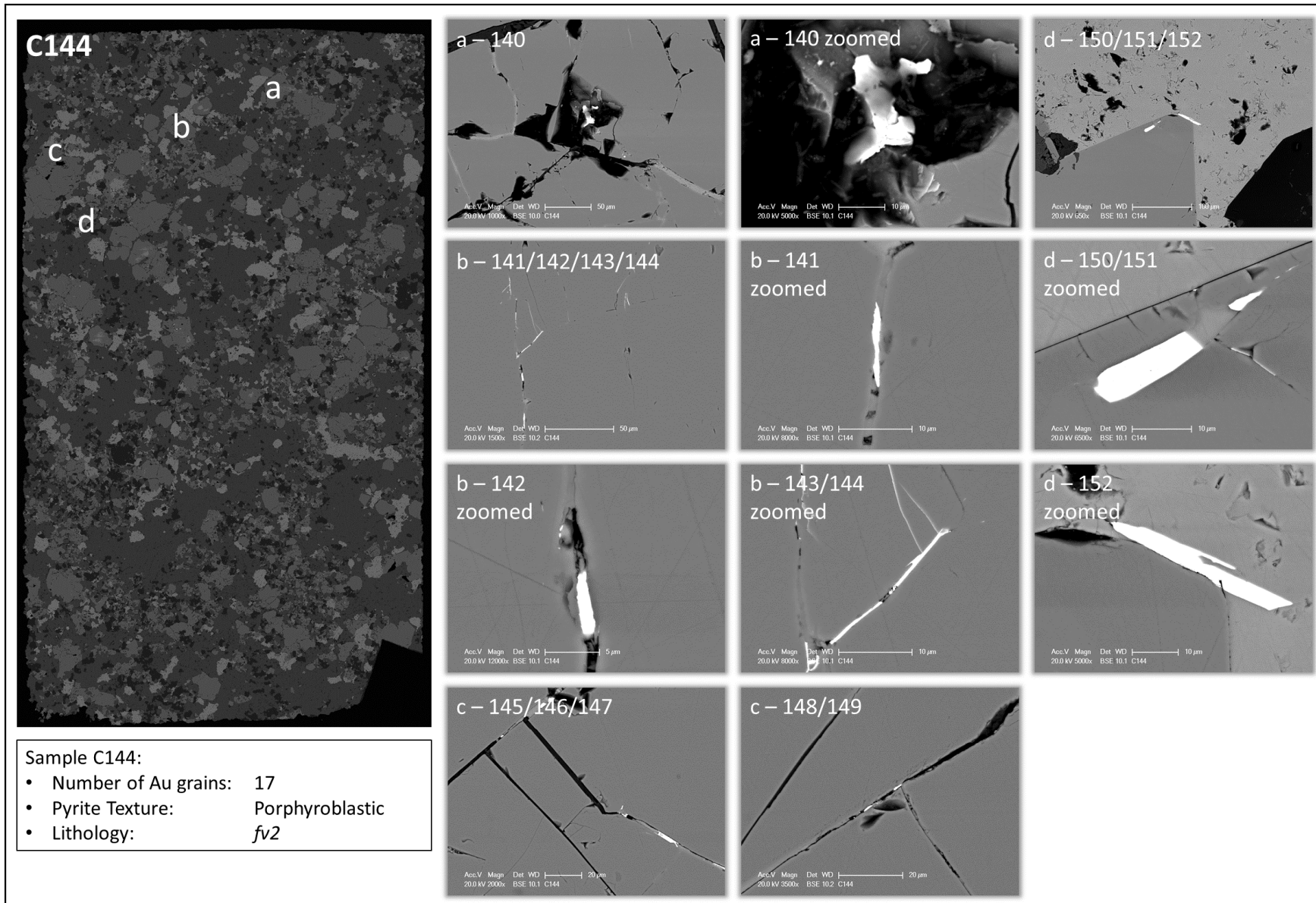


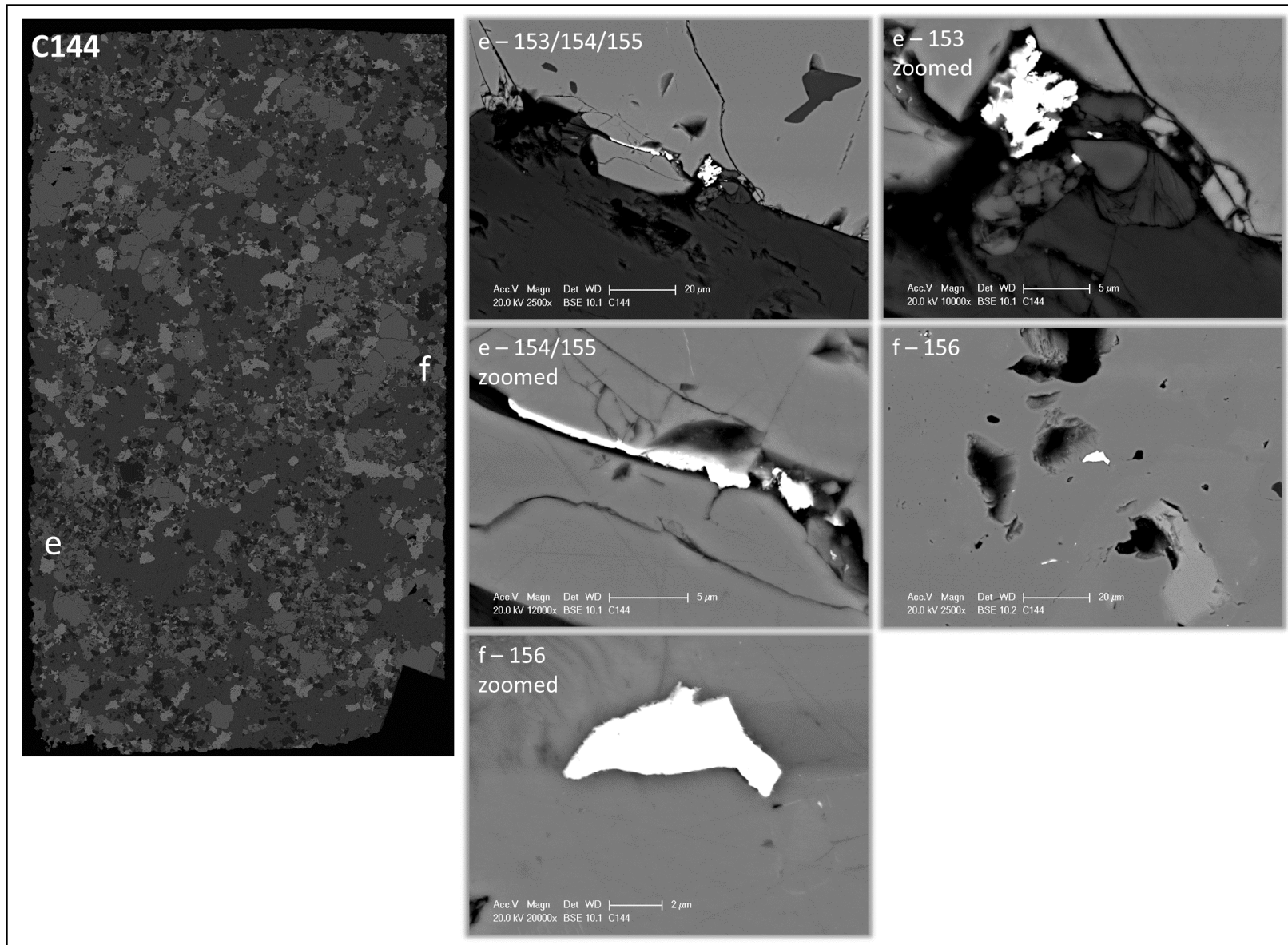






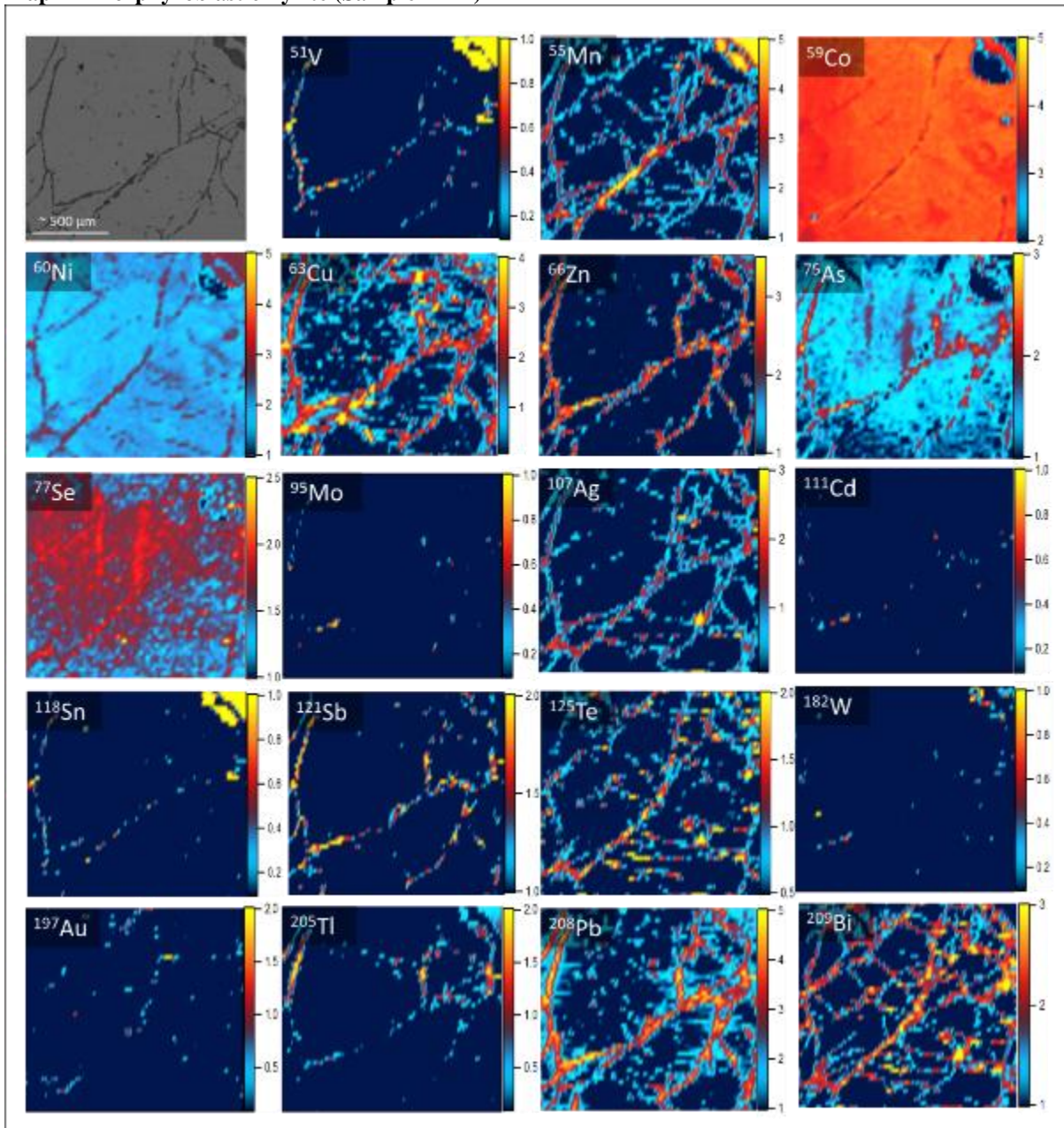




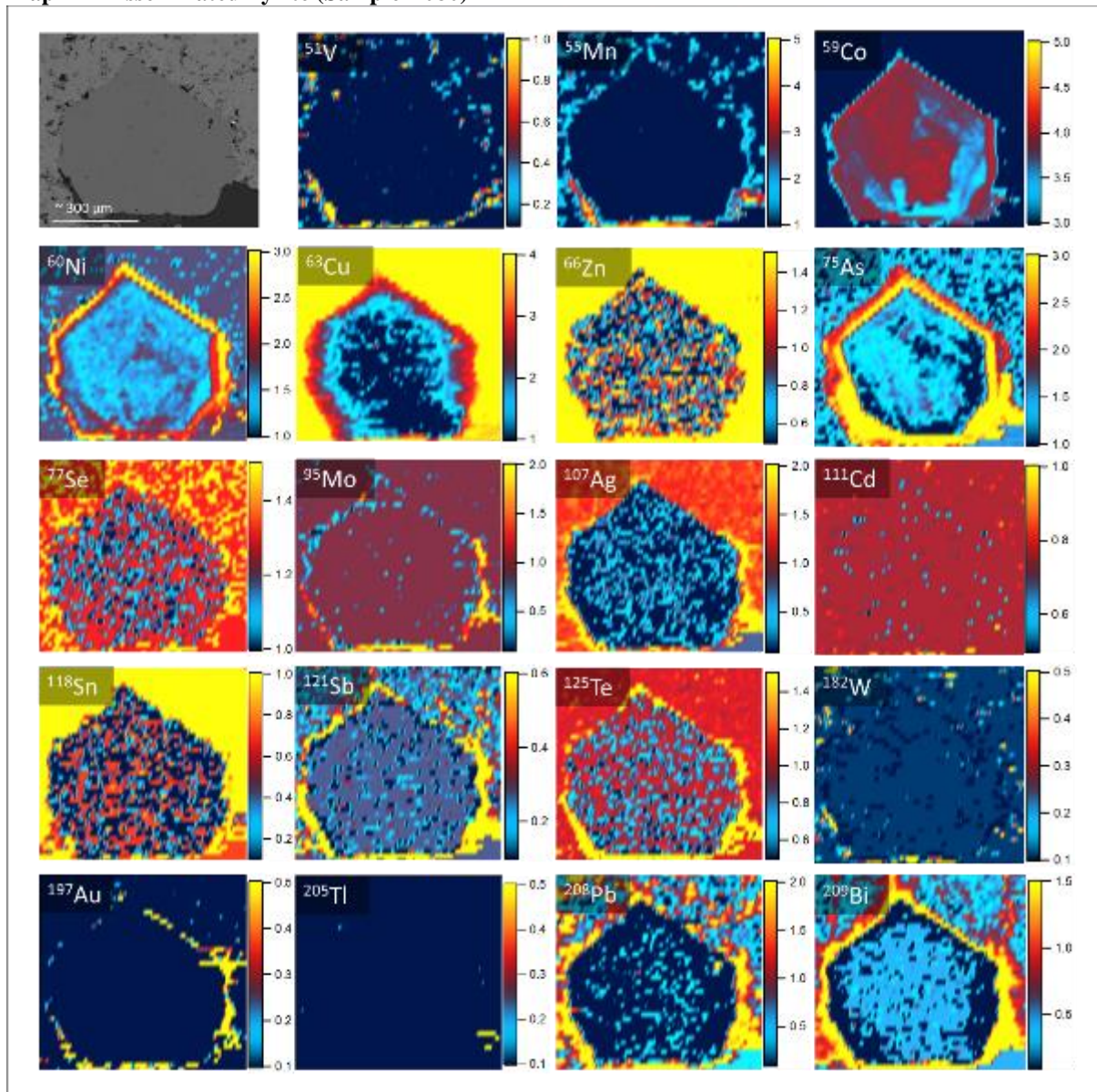


APPENDIX 3.A: EXTENDED GEOCHEMICAL PYRITE MAPS

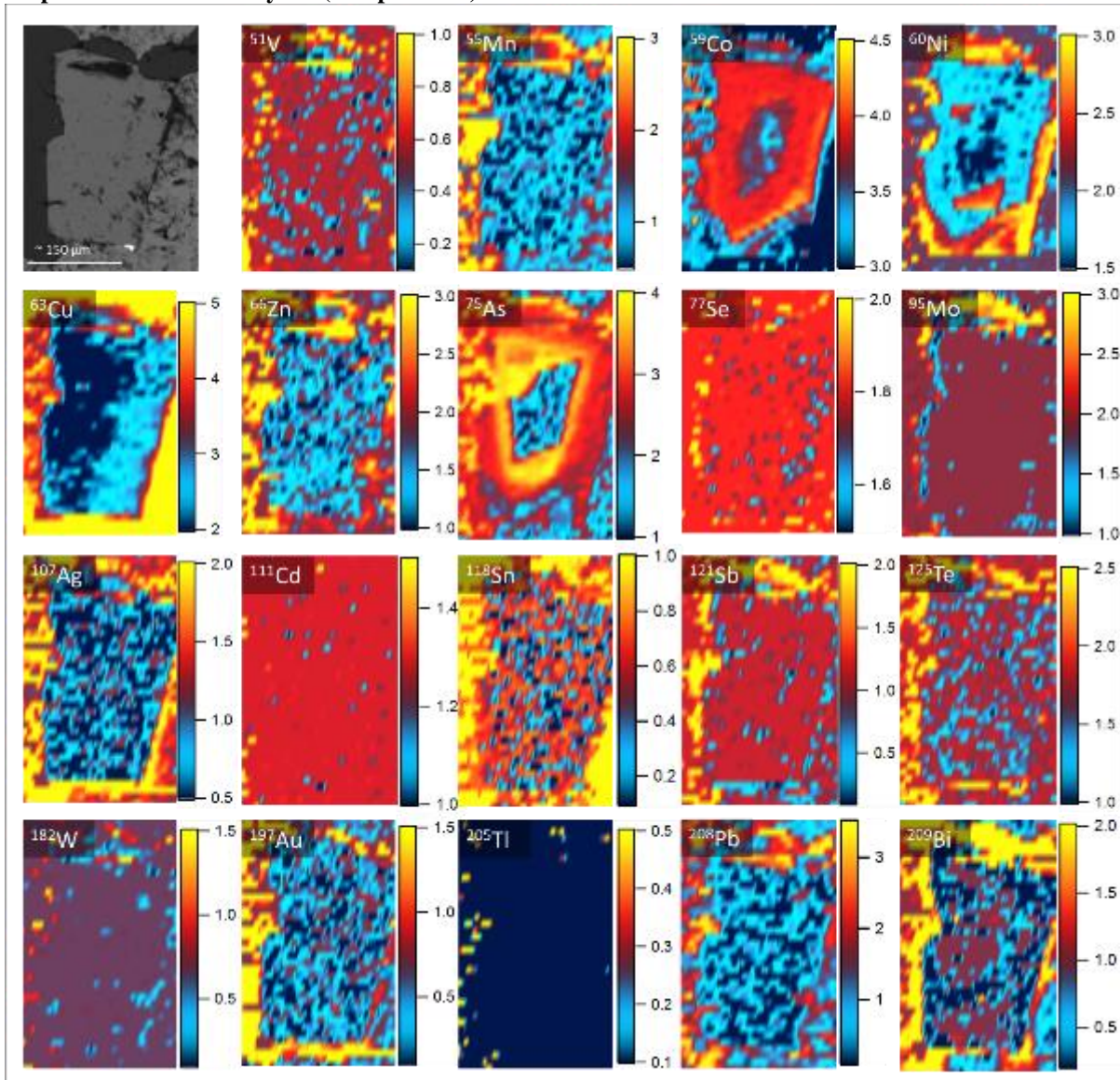
Map A – Porphyroblastic Pyrite (Sample B247)



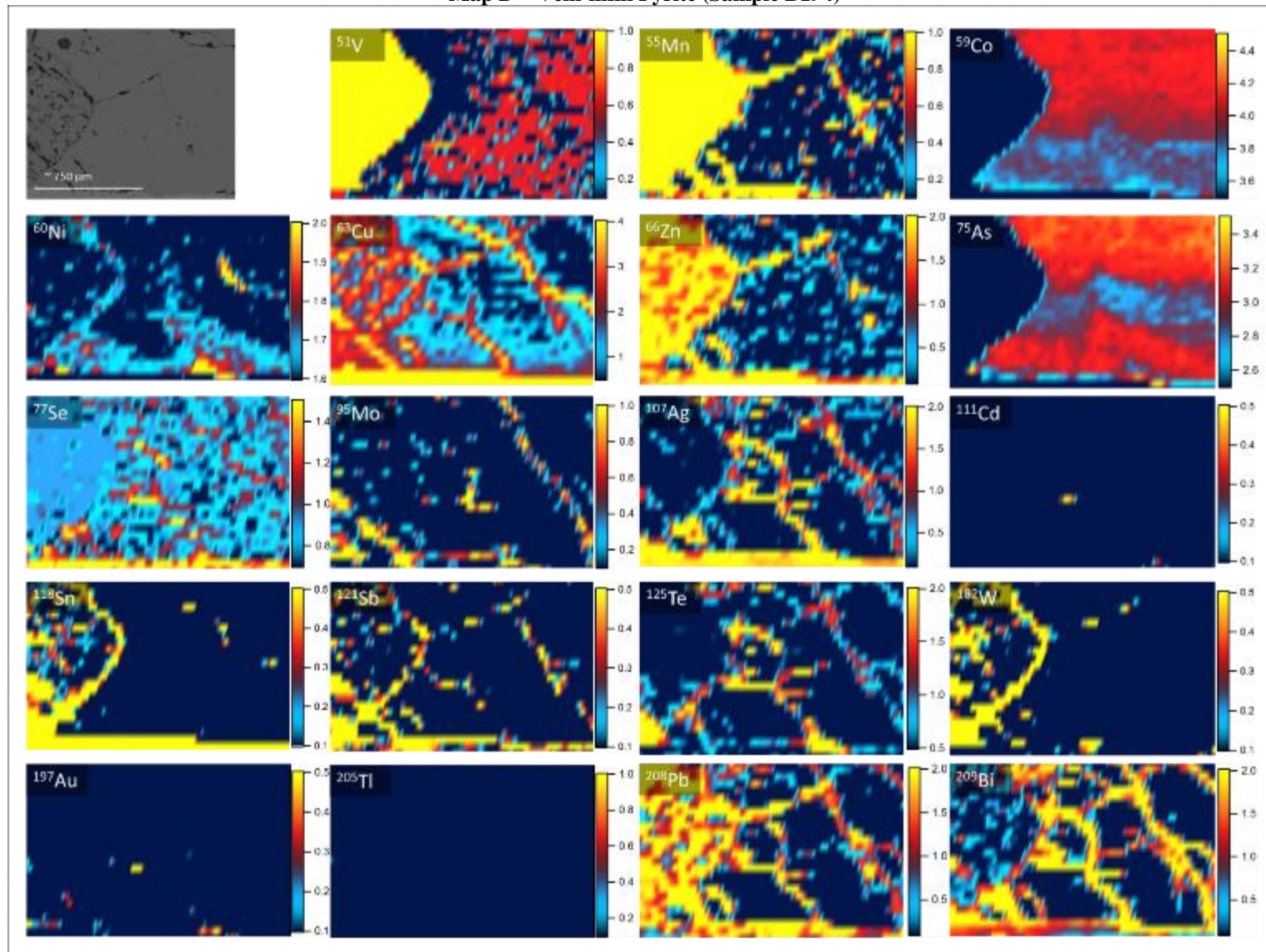
Map B – Disseminated Pyrite (Sample B080)



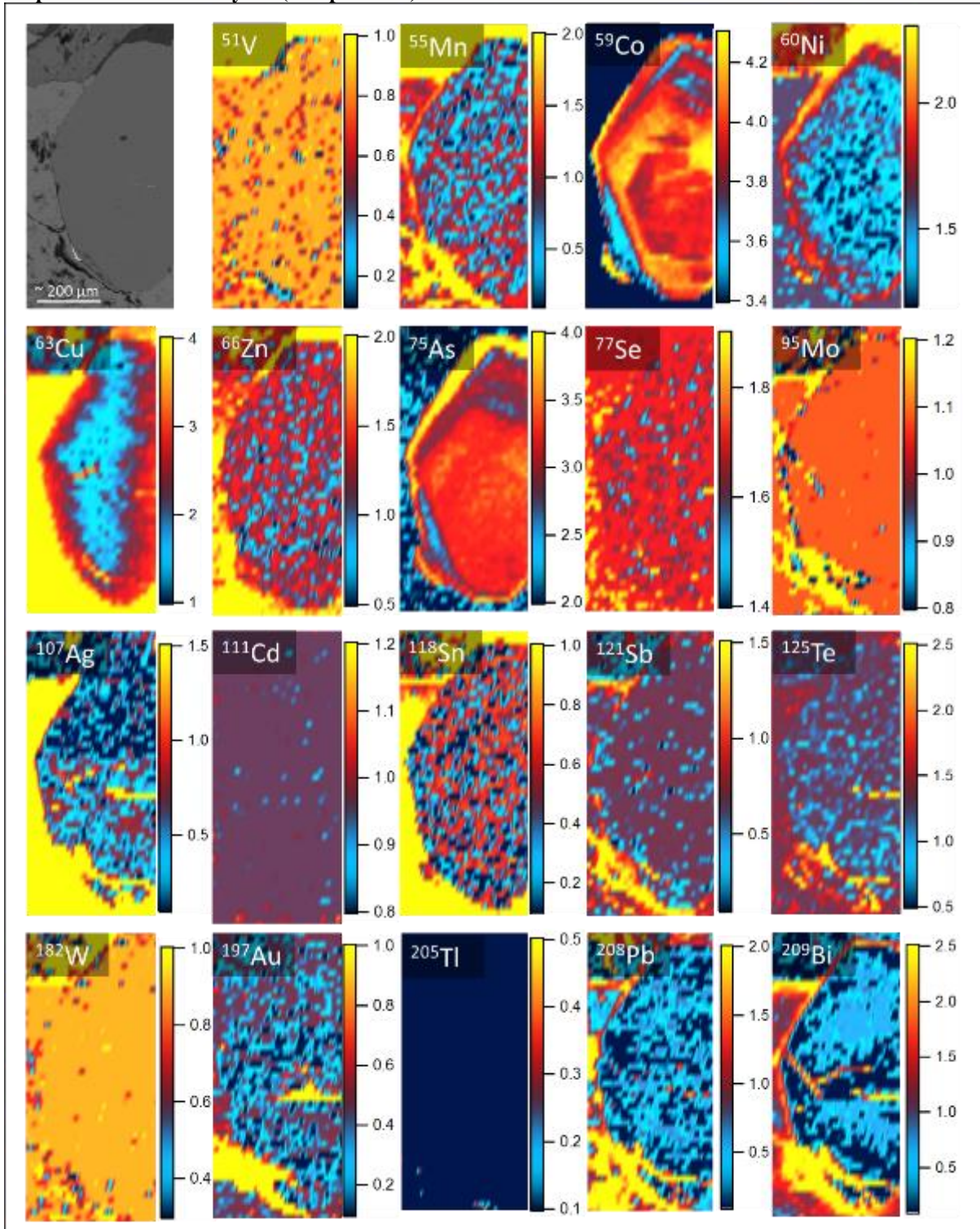
Map C – Disseminated Pyrite (Sample B080)



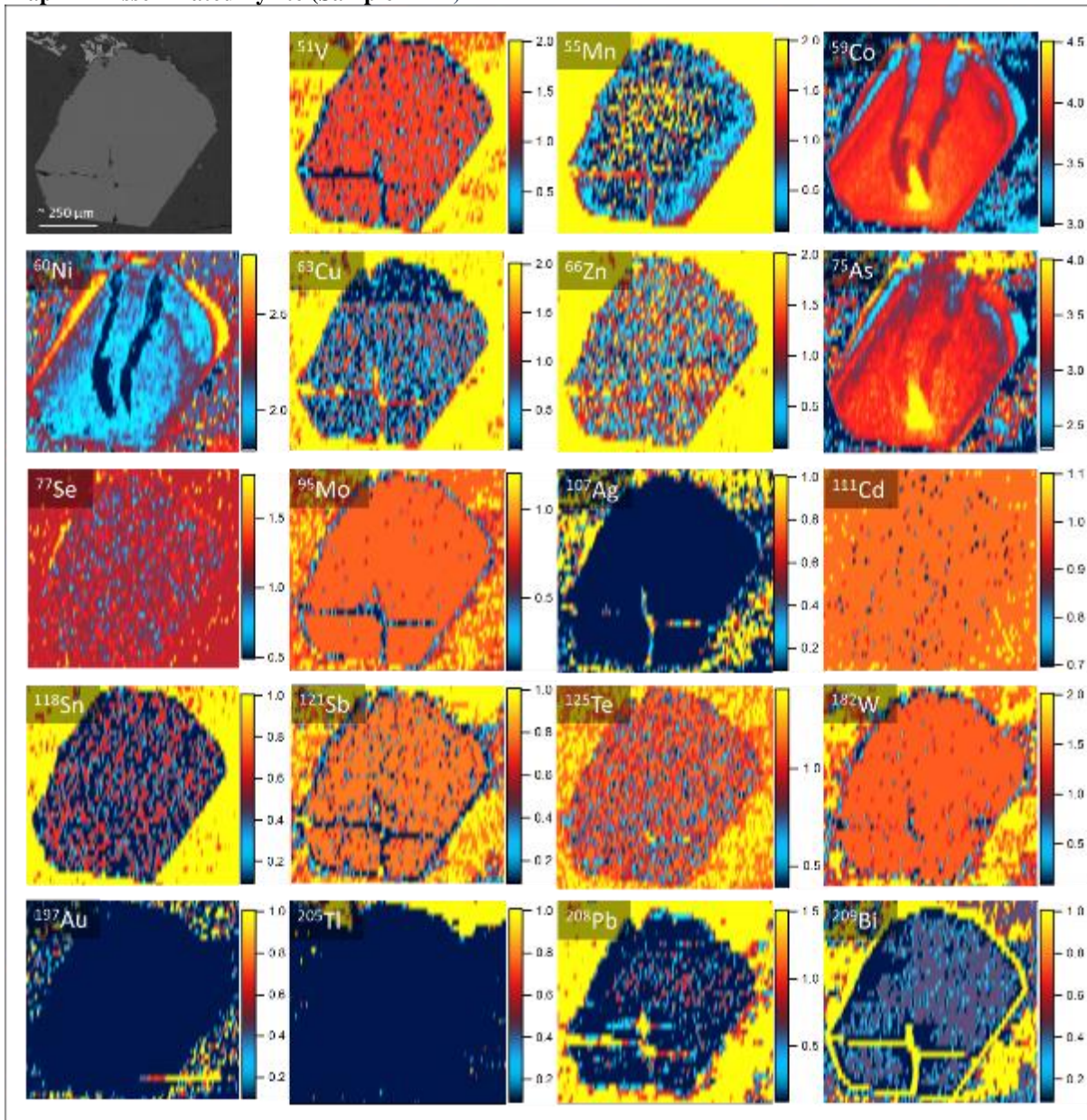
Map D – Vein-infill Pyrite (Sample B194)



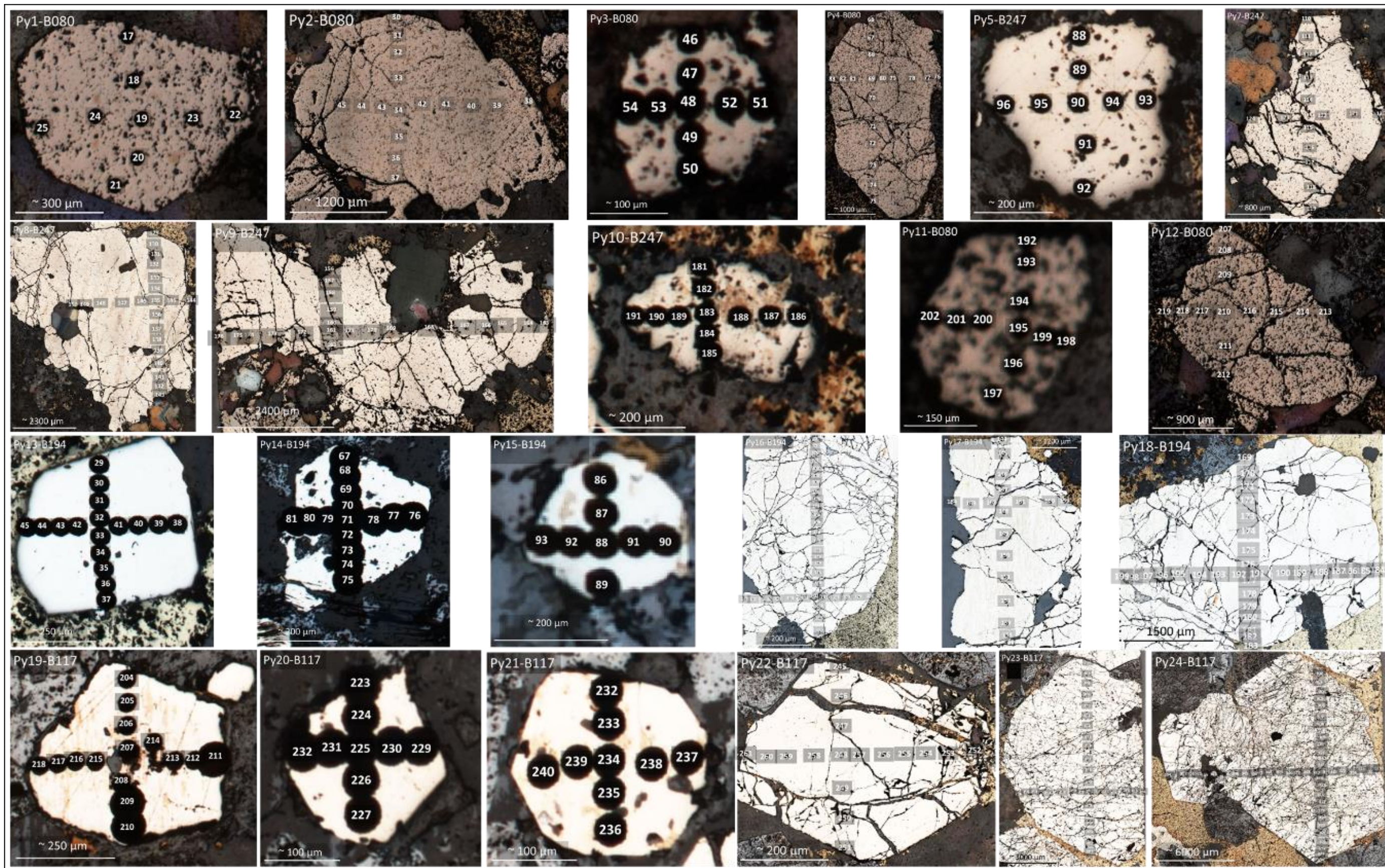
Map E – Disseminated Pyrite (Sample B194)



Map F – Disseminated Pyrite (Sample B117)



APPENDIX 3.B: PYRITE GEOCHEMICAL SPOT LOCATIONS – REFER TO EXCEL SPREADSHEET FOR SPOT DATA



APPENDIX 4: GOLD MASS BALANCE

Mass Au Present	=	167 Mt x (0.55 x 10 ⁻⁶)
	=	90.18 t
Mass Cu Present	=	167 Mt x 0.0112
	=	1.87 Mt
Moles Cu	=	1.87 Mt / (63.54 x 10 ⁻¹²) Mt/mol
	=	2.94 x 10 ¹⁰ mol
Mass Au in Chalcopyrite	=	5.40 Mt x (0.07 x 10 ⁻⁶)
	=	0.378 t
Total Invisible Au in Chalcopyrite (%)	=	(0.378 t / 90.18 t) x 100
	=	0.42%
Mass Pyrite in Reserve	=	167 Mt x 0.05
	=	8.35 Mt
Mass Au in Pyrite	=	8.35 Mt x (0.18 x 10 ⁻⁶)
	=	1.503 t
Total Invisible Au in Pyrite (%)	=	(1.503 t / 90.18 t) x 100
	=	1.67%

Therefore it is estimated that 97.91% of gold is present as free gold and other (rare) gold-bearing minerals such as sylvanite, and the remaining gold as invisible gold in chalcopyrite (0.42%) and pyrite (1.67%).